รายงานวิจัยฉบับสมบูรณ์

การบำบัดรักษาโรคติดเชื้อวิบริโอด้วยเฟจ: การคัดแยกและระบุตัวตนเฟจขนาดใหญ่ชนิดใหม่ที่มีความจำเพาะต่อกลุ่มแบคทีเรียวิบริโอ

Phage therapy for *Vibrio* infections: Isolation and identification of novel giant bacteriophages with broad host spectrum against vibrios

อาจารย์ ดร. วรพนธ์ ชัยกีรติศักดิ์

พฤษภาคม 2563

สัญญาเลขที่ MRG6180027

รายงานวิจัยฉบับสมบูรณ์

การบำบัดรักษาโรคติดเชื้อวิบริโอด้วยเฟจ: การคัดแยกและระบุตัวตนเฟจขนาดใหญ่ชนิดใหม่ที่มีความจำเพาะต่อกลุ่มแบคทีเรียวิบริโอ

Phage therapy for *Vibrio* infections: Isolation and identification of novel giant bacteriophages with broad host spectrum against vibrios

อาจารย์ ดร. วรพนธ์ ชัยกีรติศักดิ์
ภาควิชาชีวเคมี คณะวิทยาศาสตร์
จุฬาลงกรณ์มหาวิทยาลัย

สนับสนุนโดยสำนักงานคณะกรรมการการอุดมศึกษา และสำนักงานกองทุนสนับสนุนการวิจัย

Abstract

Since the emergence of deadly pathogens and multidrug-resistant bacteria at an alarmingly increased rate, bacteriophages have been developed as a controlling bioagent to prevent the spread of pathogenic bacteria. One of these pathogens, disease-causing *Vibrio parahaemolyticus* (VP_{AHPND}) which induces acute hepatopancreatic necrosis, is considered one of the deadliest shrimp pathogens, and has recently become resistant to various classes of antibiotics. Here, we discovered a novel vibriophage that specifically targets the vibrio host, VP_{AHPND}. The vibriophage, designated Seahorse, was classified in the family *Siphoviridae* because of its icosahedral capsid surrounded by head fibers and a non-contractile long tail. Phage Seahorse was able to infect the host in a broad range of pH and temperatures, and it had a relatively short latent period (nearly 30 minutes) in which it produced progeny at 72 particles per cell at the end of its lytic cycle. Upon phage infection, the host nucleoid condensed and became toroidal, similar to the bacterial DNA morphology seen during tetracycline treatment, suggesting that phage Seahorse hijacked host biosynthesis pathways through protein translation. As phage Seahorse genome encodes 48 open reading frames with many hypothetical proteins, this genome could be a potential untapped resource for the discovery of phage-derived therapeutic proteins.

บทคัดย่อ

เนื่องด้วยการเพิ่มขึ้นอย่างรวดเร็วของแบคทีเรียก่อโรคที่ดื้อยาปฏิชีวนะ แบคเทอริโอเฟจจึงเป็นหนึ่งทางเลือกที่ได้รับความสนใจในการใช้ควบคุมการกระจายของเชื้อดังกล่าว หนึ่งในเชื้อดื้อยาปฏิชีวนะและก่อโรครุนแรงในกุ้ง คือ Vibrio parahaemolyticus AHPND (VP_{AHPND}) เป็นต้นเหตุของกลุ่มอาการตับและตับอ่อนตายเฉียบพลัน งานวิจัยนี้จึงได้ทำการคัดแยกเฟจที่มีความจำเพาะต่อ VP_{AHPND} โดยเฟจชนิดนี้ถูกจัดอยู่ในวงศ์ Siphoviridae และมีชื่อว่า “ม้าน้ำ” เนื่องจากลักษณะโครงสร้างที่ปรากฏเส้นขนรอบๆหัว และมีหางที่ค่อนข้างยาว เฟจชนิดนี้มีความคงทนต่อช่วง pH และอุณหภูมิที่กว้าง นอกจากนี้เฟจจะใช้เวลาในการเพิ่มจำนวนภายในแบคทีเรียที่ค่อนข้างสั้น (30 นาที) และสร้างเฟจได้ 72 ตัวต่อเซลล์ ในการศึกษาระดับเซลล์พบว่าภายหลังการ infect ของเฟจ สารพันธุกรรมของแบคทีเรียจะค่อยๆ ปรากฏเป็นลักษณะกลมอยู่กลางเซลล์ และค่อยเปลี่ยนเป็นลักษณะ toroid ซึ่งลักษณะดังกล่าวเหมือนกับการที่แบคทีเรียได้รับยาปฏิชีวนะชนิด tetracycline จึงมีความเป็นไปได้ว่าเฟจม้าน้ำมีกลไกเช่นเดียวกับยา tetracycline ที่สามารถรบกวนการถอดรหัสโปรตีนของแบคทีเรียระหว่างการเพิ่มจำนวนได้ จีโนมของเฟจมีสามารถถอดรหัส 48 ORF และมีโปรตีนที่ไม่ทราบหน้าที่อีกมาก จึงแสดงให้เห็นถึงความเป็นไปได้ในการใช้สารที่ได้จากการสร้างของเฟจในการยับยั้งการสร้างโปรตีนของแบคทีเรียเพื่อยับยั้งเชื้อก่อโรค

Keywords: bacteriophages, *Vibrio* phage, phage genome, phage infection, *Vibrio parahaemolyticus*

Project Code: MRG6180027

Project Title: Phage therapy for *Vibrio* infections: Isolation and identification of novel giant bacteriophages with broad host spectrum against vibrios

Investigator: Vorrapon Chaikeeratisak / Department of Biochemistry, Chulalongkorn University

E-mail Address: Vorrapon.C@chula.ac.th

Project Period: 2 years

Objectives

To isolate and characterize phage targeting pathogenic *Vibrios*

Material and Methods

Phage isolation, purification, and preparation. Overnight cultures of VP_{AHPND} were prepared by inoculating the bacteria, previously grown on Tryptic Soy Agar supplemented with 1.5% Sodium chloride (TSA-1.5%NaCl), into 5 ml of Tryptic Soy Broth supplemented with 1.5% Sodium chloride (TSB-1.5%NaCl) and allowed to incubate at 30 °C, 200 rpm for at least 16 hours. One milliliter of seawater was added to 25 ml of TSB- 1.5%NaCl, 250 µl of 100 mM $CaCl_2$, and 2.5 ml of VP_{AHPND} overnight culture. Phage was enriched by growing at 30 °C, 200 rpm for 48 hours. Phage was next harvested by centrifugation at 9,000 rpm for 10 minutes followed by collecting and filtering the supernatant using a 0.45 µm filter. Next, phage purification was performed using double-layer agar method. Briefly, 10-fold serial dilutions of phage were prepared using SM buffer. Ten microliters of each diluent were added to 100µl of overnight culture of VP_{AHPND}, mixed and allowed to stand for 10 minutes. To this, 5 ml of melted 0.35% top agar of TSA-1.5%NaCl was added, mixed and poured onto a TSA-1.5%NaCl plate. The plates were incubated overnight at 30 °C. Putative translucent plaques were identified and picked and resuspended in 100 µl of SM buffer. This purification step was repeated 3 times. A high-titer phage lysate was prepared described by Chaikeeratisak *et al.*[1]. Briefly, 5 ml SM buffer was added to a near-confluent plate and incubated at 30 °C for at least 5 hours. The solution was aspirated into a tube and centrifuge at 9,000 rpm for 5 minutes. Finally, the supernatant was filtered using a 0.45 µm filter and stored at 4 °C.

This work has been reviewed and approved by Chulalongkorn University-Institutional Biosafety Committee (CU-IBC) in accordance with the levels of risk in pathogens and animal toxins listed in the Risk Group of Pathogen and Animal Toxin (2017) published by Department of Medical Sciences (Ministry of Public Health), the Pathogen and Animal Toxin Act (2015) and Biosafety Guidelines for Modern Biotechnology BIOTEC (2016) with approval number: SC CU-IBC-006/2018.

Transmission electron microscopy and cryo-electron tomography. 3 µl of phage titer was deposited on QUANTIFOIL 200 mesh holey carbon R 2/1 gold grids, glow-discharged using PELCO easiGlow (Ted Pella). The grids were blotted using Whatman No. one filter paper and plunge-frozen into a liquid ethane/propane mixture cooled by liquid nitrogen using a custom-built device (Max Planck Institute for Biochemistry, Munich). Tilt series were collected on grids clipped onto autogrids (Thermo Scientific) in a 300 keV Titan Krios (Thermo Scientific) fitted with a K2 Summit 4k x 4k pixel direct electron detector and a GIF Quantum post-column energy filter (Gatan) using a nominal magnification of 42 kx or a pixel size of 3.4 Å and −5 µm defocus. Tilt series were acquired using SerialEM in low dose mode, typically from −40o to +40o every 2–3 degrees with a total dose of 50–70 e/Å2. The tilt series were aligned and dose-

weighted according to the cumulative dose using MotionCor2 and reconstructed in IMOD software using weighted back-projection.

Conventional phage study. To evaluate phage adsorption, VP_{AHPND} culture (OD_{600} ~ 0.4) was infected with phage particles at MOI 0.01 (The OD_{600} of 1 = 1 × 10^9 CFU/ml[2]) and incubated at 30 °C. At each time point of 0, 1, 2, 5, 7.5, 10, 15, 20, 25, and 30 minutes, 100 µl of the samples were collected and diluted 10-fold in SM buffer. After centrifugation at 15,000 × g for 2 minutes at 4 °C, the supernatant was harvested and the number of free phages was determined by double-layer agar method. For the one-step growth curve analysis, VP_{AHPND} was infected at MOI 0.01 at 30 °C for 15 minutes, then the cell suspension was centrifuged at 12,000 × g for 5 minutes. The pellet was resuspended in 10 ml of TSB-1.5% NaCl. The mixture was then incubated with vigorous shaking at 200 rpm, 30 °C for 2 hours. Throughout the period of shaking, the samples of the untreated group and the chloroform-treated group were taken every 10 minutes to evaluate total virions by double-layer agar method.

For pH stability, 100 µl of phage lysate was mixed with 900 µl of SM buffer in a pH range 2 to 10 and incubated at 30 °C for 1 hour. For temperature stability, 50 µl of phage lysate was incubated for 1 hour at different temperatures; 4, 20, 25, 30, 37, 40, 50, 60, and 70 °C. For both tests, phage infectivity was determined by performing a spot test. These experiments were performed in triplicate.

To determine host spectrum of the phage, a spot test was performed to test the infectivity of the isolated phage against different 26 bacterial strains that we obtained and were kindly offered from different sources as indicated in Table 1. Briefly, overnight cultures were prepared as described above. 500 µl of each culture was mixed with 5 ml of 0.35% molten top agar (TSA-1.5% NaCl) and immediately poured on an agar plate (TSA-1.5% NaCl). After the cell lawn was solidified, 5 µl of each diluent of 10-fold serially diluted phage was spotted on the surface of the top agar. The plates were allowed to dry and next incubated overnight at 30 °C. The clearing zones were then evaluated for the infection ability of the phage toward the bacterial host.

Phylogenetic tree construction. DNA sequences of the terminase large subunit of various phages were obtained through GenBank. These sequences included accession number and phage names as follows: Vibriophage KVP40: NC_005083, Vibriophage CP-T1: NC_019457.1, Vibriophage pVp-1: NC_019529.1, Vibriophage vB_VpaS_MAR10: NC_019713.1, Vibriophage VH7D: NC_023568.1, *Enterobacteria* phage 9 g: NC_024146.1, *Salmonella* phage Stitch: NC_027297.1, Vibriophage phi 3: NC_028895.1, *Enterobacteria* phage JenK1: NC_029021.1, *Vibrio vulnificus* phage SSP002: NC_041910, *Enterobacteria* phage EPS7: NC_010583.1 and phage Seahorse. The sequences were aligned using ClustalW and the phylogenetic tree was constructed using Molecular Evolutionary Genetics Analysis (MEGA) version 10.0 as described by Kumar *et al*.[3]. Using the Maximum Likelihood method, a bootstrap consensus phylogenetic tree from 100 bootstrap replications for tree construction was selected. The selected numbers of bootstrap were shown on the selected branches.

Lysogeny experiment. To isolate phage-resistant strains, bacterial colonies that appeared in a double layer-agar plate at high titer of phage were picked and further isolated. The isolated strains and original VP_{AHPND} were tested for phage resistance by cross streaking each isolate with a drop of high titer phage lysate atop the bacterial stripes. The plate was incubated overnight at 30 °C and the result was recorded. To test whether the phage-resistant isolates were lysogen, a bacterial cell lawn of VP_{AHPND} strain was prepared as described above. Single colony of each phage-resistant isolate was picked by a sterile toothpick and stabbed into the top agar. The plate was then incubated at 30 °C overnight and the presence of a clear zone surrounding the stab isolate was recorded the day after.

Bacterial cell lysis profile assay. VP_{AHPND} culture at mid-log phase (OD_{600} ~ 0.4) was inoculated with phage lysate at MOI 0 as a control and MOI 0.01 and MOI 5 as experimental groups. The cultures were then incubated shaking at 200 RPM at 30 °C. OD_{600} of all cultures were monitored every 30 minutes until 10 hours of incubation. The experiment was carried out in triplicate.

Phage genome DNA extraction. The phage lysate was first dialyzed in sterile distilled water. Next, phage was precipitated by adding 2.5 ml of phage precipitant solution (30% w/v PEG-8,000, 3.3 M NaCl and sterile distilled water) to 10 ml of phage lysate (~10^9 pfu/ml) and stored overnight at 4°C. The solution was then centrifuged at 10,000 rpm for 30 minutes followed by resuspending the pellet in 500 µl of 1xDNase I buffer. To degrade bacterial genomic DNA and RNA, 5U DNaseI and 25 µg RNaseA were added and incubated at 37 °C for 2 hours. Next, 25 mM EDTA was added to inhibit nuclease activity, followed by 0.5% SDS and 25 µg proteinase K, and incubated at 60 °C for 2 hours. Phenol-chloroform extraction was then performed to extract phage genomic DNA.

Phage genome sequencing and analysis. Phage genomic DNA was sequenced by Illumina MiSeq plat- form. All raw reads were qualified and the low qualities were eliminated. The adaptors in the filtered reads were then trimmed and assembled into contigs. To remove potential host DNA contamination, reads were mapped to the host strain sequence of *V. parahaemolyticus* strain ATCC17802 (GenBank accessions CP014046, CP014047) using the Geneious mapper in Geneious Prime 2019 (https://www.geneious.com). The unmapped reads were used for assembly in Geneious Prime 2019 with the Geneious assembler using high sensitivity and default parameters. A list of ORFs was generated from this contig using the ORF finder in Geneious; filtering out any ORFs less than 200 base pairs. The protein sequences of each ORFs were predicted by EMBOSS Transeq and they were annotated manually by BLASTp and PSI-BLAST (cut-off e-value < 10^{-4}) against various databases: NCBI's non-redundant (nr) protein sequences, InterPro 75.0, NCBI conserved domain and ACLAME. In addition, to confirm the pre- dicted function, RAST sever, Prodigal and PHASTER were used as well. To determined antimicrobial resistance coding genes and putative toxins, RESFINDER and VirulenceFinder were used, respectively. Aragon and tRNAS- canSE were used to identify tRNAs. The map of genome was drawn by Artemis and DNA plotter.

Single cell-infection assay. VP_{AHPND} culture (OD_{600} ~ 0.4) was infected with phage at MOI 5 and the infected cells were incubated at 30 °C. At each time point; 0, 10, 20 and 30 minutes, the samples were harvested by centrifugation at 9,000 rpm for 2 minutes and the supernatant discarded. As described by Chaikeeratisak *et al.*[1], phage-infected cells were fixed at a final concentration of 4% paraformaldehyde and incubated at room tempera- ture for 15 minutes. The fixed cells were centrifuged and the pellets were washed with 500 µl of 1x PBS three times. The cells were resuspended in 1x PBS before loading 3 µl onto an agarose pad (1.2% agarose in 20% TSB-1.5% NaCl) that contained fluorescent dyes (2 µg/ml FM 4–64 and 2 µg/ml DAPI). The samples were visualized under DeltaVision Ultra High-Resolution Microscope. For live cells, the cells were harvested at desired time points, and inoculated on an agarose pad as described above. The nucleoid was stained with either 0.5 µM SYTOX-green or 0.5 µM SYTO 16, prior to fluorescence microscopy.

Minimal inhibitory concentration. Minimal inhibitory concentrations (MIC) were determined for the following antibiotics: Ciprofloxacin, Rifampicin, and Tetracycline, which were all used in the fluorescence microscopy experiment shown in Table S1. The antibiotics were respectively serially diluted in a 96 well plate using a microdilution method[4]. Overnight cultures of VP_{AHPND} were diluted 100-fold in TSB-1.5% NaCl and allowed to grow on a roller at 30 °C until exponential growth (OD_{600} of 0.2) was observed. The culture was further diluted 100-fold in TSB-1.5% NaCl into wells of the same 96-well plate that contained different concentrations of the respective antibiotic. The culture was further incubated at 30

°C for 24 hours. MICs for each antibiotic were determined as the lowest concentration dilution of that antibiotic capable of inhibiting growth of the bacteria.

Fluorescence microscopy. Overnight cultures of VP_{AHPND} were diluted 100-fold in TSB-1.5% NaCl and incubated at 30 °C on a roller until exponential phase of growth was obtained. Antibiotics were added to the culture at concentrations of 5 times the MIC. For live cell imaging, cultures were incubated at 30 °C on a roller for 60 minutes followed by staining with fluorescent dyes; FM 4–64 (2 μg/ml), DAPI (2 μg/ml) and SYTOX-green (0.5 μM). Cultures were then harvested by centrifugation at 6,000 g for 30 seconds and resuspended in 30 μl of supernatant. 3 μl of sample was loaded onto agarose pad (1.2% agarose containing 20% TSB-1.5% NaCl) on concave glass slides and fluorescence microscopy was performed, following consistent imaging parameters throughout all of the experiments. For fixed cell imaging, cultures were incubated on a roller at 30 °C for 30 and 60 minutes for treatment with ciprofloxacin and rifampicin, while 10, 20, 30 and 60 minutes for treatment with tetracycline. After the completion of each treatment, cultures were fixed as described above. Cultures were then harvested by centrifugation at 9,000 rpm for 2 minutes followed by washing the pellet with 1x PBS for 3 times. After centrifugation, the pellet was resuspended in 30 μl of 1x PBS and added to an agarose pad as described above. Fluorescence microscopy was performed using consistent imaging parameters for all experiments.

Results

Morphological and biological properties of phage Seahorse

Bacteriophages that target VP_{AHPND} were enriched and isolated from seawater collected from a local shrimp farming area in Thailand. A phage selected for this study actively lysed VP_{AHPND} and produced a 2–3 mm plaque with a 0.5 mm clear spot at the center surrounding by the halo-turbid area (Fig. 1a). As observed in negative staining by transmission electron microscopy (TEM), the phage belongs to the order *Caudovirales* and the family *Siphoviridae* as it has an icosahedral capsid with a long non-contractile tail with short tail fibers (Fig. 1b). In order to visualize the phage at a higher resolution and at a near-native state, we imaged the phage using cryo-electron tomography (cryo-ET). Our cryo-ET images indicated that the phage had a capsid of ~65 nm in diameter and a tail of ~125 nm in length (Fig. 1c–e; n = 3). The phage capsid seemed to be decorated with other proteins which may likely constitute the head fiber similar to those found in *Bacillus subtilis* phage Phi29 and adenoviruses[5–7]. Our cryo-ET images of the phage also revealed the presence of capsid fibers (the shaft with a knob) of ~10 nm in length at the vertices of the capsid (Purple arrows; Fig. 1c). We also see densities on the capsid facets (~3 nm) which may correspond to minor capsid proteins similar to those found in adenoviruses (Orange arrows; Fig. 1c)[5,8]. These are believed to enhance capsid stability by forming strong protein-protein interactions. Further biochemical and structural studies are needed to characterize and resolve these protein densities unambiguously. Based on the 3-dimensional phage structure under Cryo-ET, we designated this vibriophage as “Seahorse”.

To gain more information on the biological properties of phage Seahorse, we tested its host range and conducted a one-step growth curve, a phage tolerance test and measured phage adsorption rate. Out of 26 different bacterial strains tested, phage Seahorse exhibited a narrow host spectrum and specifically infected *V. parahaemolyticus* strain TM that causes AHPND or VP_{AHPND} (Table 1). A phage adsorption assay revealed that more than 95% of the phage were rapidly adsorbed onto the host cell within 15minutes (Fig. 1f). The one-step growth curve showed that the phage propagated in the cell during the latent period for at least 30 minutes and resulted in a burst size of 72 virions per cell (Figs. 1g, S1, and Table S2). Additionally, the phage was highly tolerant to a wide range of pH and temperatures (Fig. 1h,i). Figure 1h revealed that the phage was able to infect the host with the highest infectivity at pH 6–7 and the infectivity was found to be completely lost at pH 1–3 (Fig. 1h). A thermal stability study showed that the phage was still active at

temperatures between 4 °C–50 °C while the phage pre-treated with high temperatures above 60 °C significantly lost their infectivity (Fig. 1i).

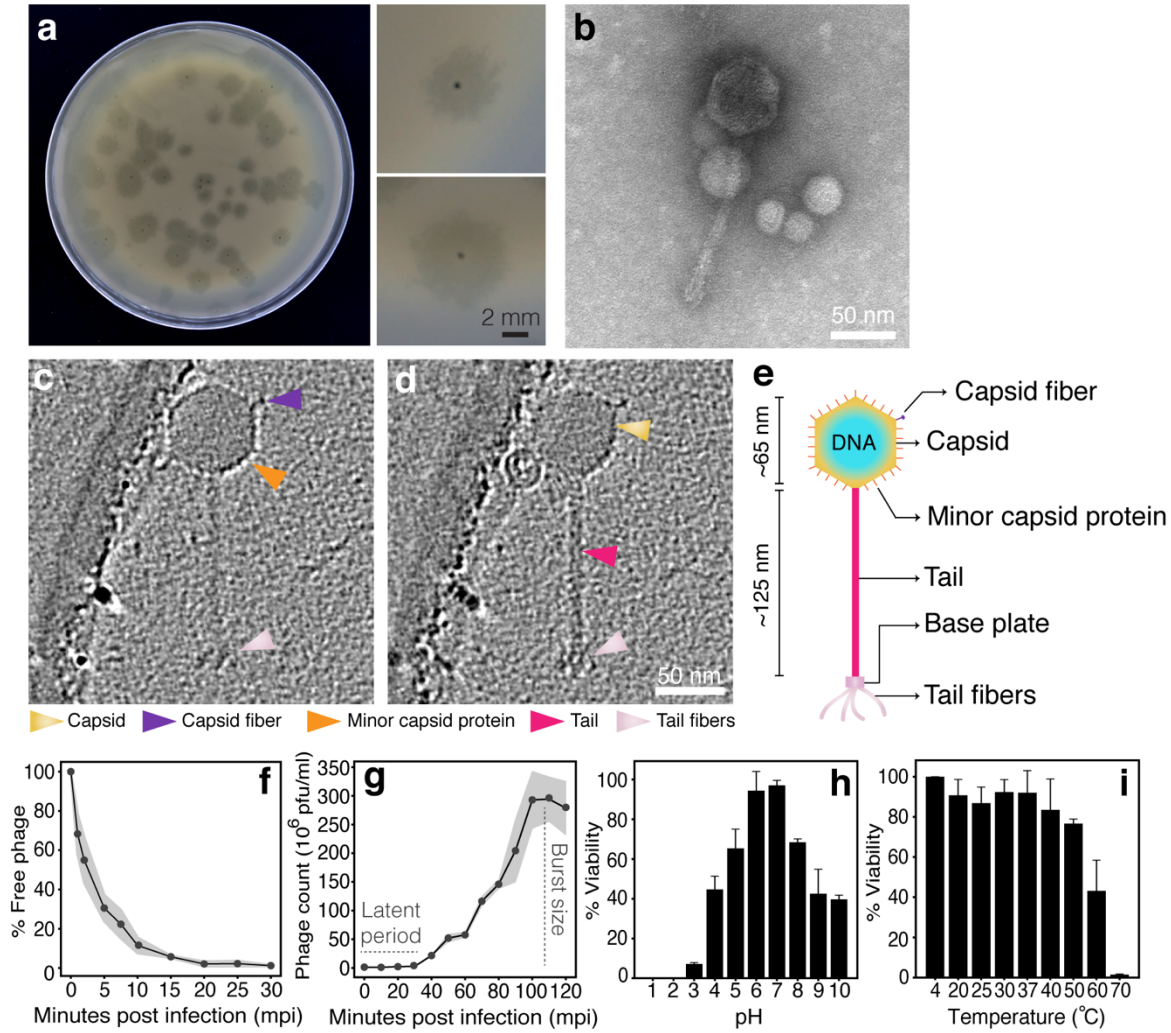

Figure 1. Morphological and biological properties of phage Seahorse. (**a**) Plaque morphology of phage Seahorse. An individual plaque is shown in the right panels. Scale bar equals to 2 mm. Morphology of phage Seahorse as determined by Negative staining and TEM (**b**) and Cryo-ET (**c**,**d**). Different slices (**c**,**d**) through the same Cryo-ET showing the structure of phage Seahorse. Arrows indicate capsid, capsid fiber, minor capsid protein, tail and tail fibers. Scale bar equals to 50 nm. (**e**) Schematic of phage Seahorse as visualized by Cryo-ET with the capsid size and the tail length indicated. (**f**–**i**) Biological studies of phage Seahorse; Adsorption assay (**f**), One-step growth curve (**g**), phage viability in different pH (**h**) and different temperature (**i**). The experiments (**f**–**i**) were conducted in at least 3 independent biological replicates and the data are represented as the mean ± standard deviation.

Bacterial species	Strain	Source	Plaque formation
Vibrio parahaemolyticus	AHPND (TM)	Junprung *et al.*	+
	Non-AHPND		-
	ATCC 17802	American type culture collection	-
	DMST 5665	DMST laboratory collection	-
Vibrio harveyi	Isolate 639		-
	Isolate 102		-
	Isolate 2207	Department of Microbiology, Faculty of	-
	Isolate 1526	Science, Chulalongkorn University	-
	Isolate gn		-
	Isolate 35		-
Vibrio alginolyticus	DMST 14800		-
Vibrio cholerae	DMST 2873		-
Vibrio fluvialis	DMST 21248	DMST laboratory collection	-
Vibrio vulnificus	DMST 21245		-
Vibrio mimicus	DMST 21244		-
Vibrio natrigens	ATCC 14048	American type culture collection	-
*Vibrio spp.**	VC1060		-
	VC1061	Isolated from healthy shrimp	-
	VC1062	(This study)	-
	VC1063		-
Pseudomonas aeruginosa	PA01	Klockgether *et al.*	-
Pseudomonas chlororaphis	200-B	Serwer *et al.*	-
Escherichia coli	ATCC 25922		-
Burkholderia thailandensis	ATCC 700388	American type culture collection	-
Acinetobacter baumannii	ATCC 17978		-
	ATCC 196096		-

*Identified by 16s sequencing

DMST: Department of Medical Sciences, Ministry of Public Health, Thailand

Table 1. Host range determination of phage Seahorse. Different bacterial species and strains were used as the host to determine the host spectrum of the phage using a spot test. *Identified by 16 s sequencing. DMST: Department of Medical Sciences, Ministry of Public Health, Thailand.

Genome features and annotation of phage Seahorse

The complete genome of Seahorse was 45,171 bp long with a GC content of 42.59% encoding 48 putative open reading frames (ORFs) and 3 tRNA genes (Fig. 2 and Table 2). These predicted ORFs were scattered throughout the phage Seahorse genome with different gene arrangements; 35 ORFs in the forward direction and 13 ORFs in the reverse direction (Fig. 2). Out of the total predicted ORFs, 22 ORFs were assigned a putative function according to the significant hits in the indicated databases with E-values less than 10^{-4} while the rest were identified as hypothetical proteins (Table 2). Among them, more than 80% of start codons in the ORFs were ATG followed by TTG (14.58%) and CTG (2.08%). We classified the 22 ORFs into 7 main groups according to function; (1) replication, transcription and translation, (2) DNA metabolism and modification, (3) virion structure and assembly, (4) phage regulation, (5) Nin regions, (6) lysis protein, and (7) other phage-related proteins (Fig. 2). In addition, we did not observe any antimicrobial resistance-coding genes or putative toxins from the phage genome.

As shown in Table 2, we found that the majority of predicted ORFs were virion structural proteins including head morphogenesis protein, tail tape measurement protein, and tail tubular protein as well as ATPase and both small and large subunits of the terminase enzyme, which is involved in DNA encapsidation. A phylogenetic tree of large subunits of terminase of phage Seahorse revealed the close relationship to the temperate vibriophage MAR10 (Fig. S2). Phage Seahorse encoded a set of crucial enzymes that are involved in DNA replication and transcription (e.g. DNA helicase, ribonuclease, and transcriptional regulator), and DNA metabolism and modification (e.g. nucleoside triphosphate pyrophosphohydrolase and adenine methylase). Some ORFs were predicted as a transposase which is involved in phage DNA integration into the host genome while others were categorized as High frequency lysogenization C and

Rha family proteins, which also serve a role in the regulation of lysogenic life cycle of phages, all of which suggest that phage Seahorse is indeed a temperate phage[9–11]. This annotation was further validated by a lysogeny experiment and a host cell lysis profile, both confirming that phage Seahorse has an ability to lysogenize the host (Fig. S3). Moreover, we also identify N-acetylmuramoyl-L-alanine amidase, an enzyme that degrades the peptidoglycan layer in bacterial cell walls[12].

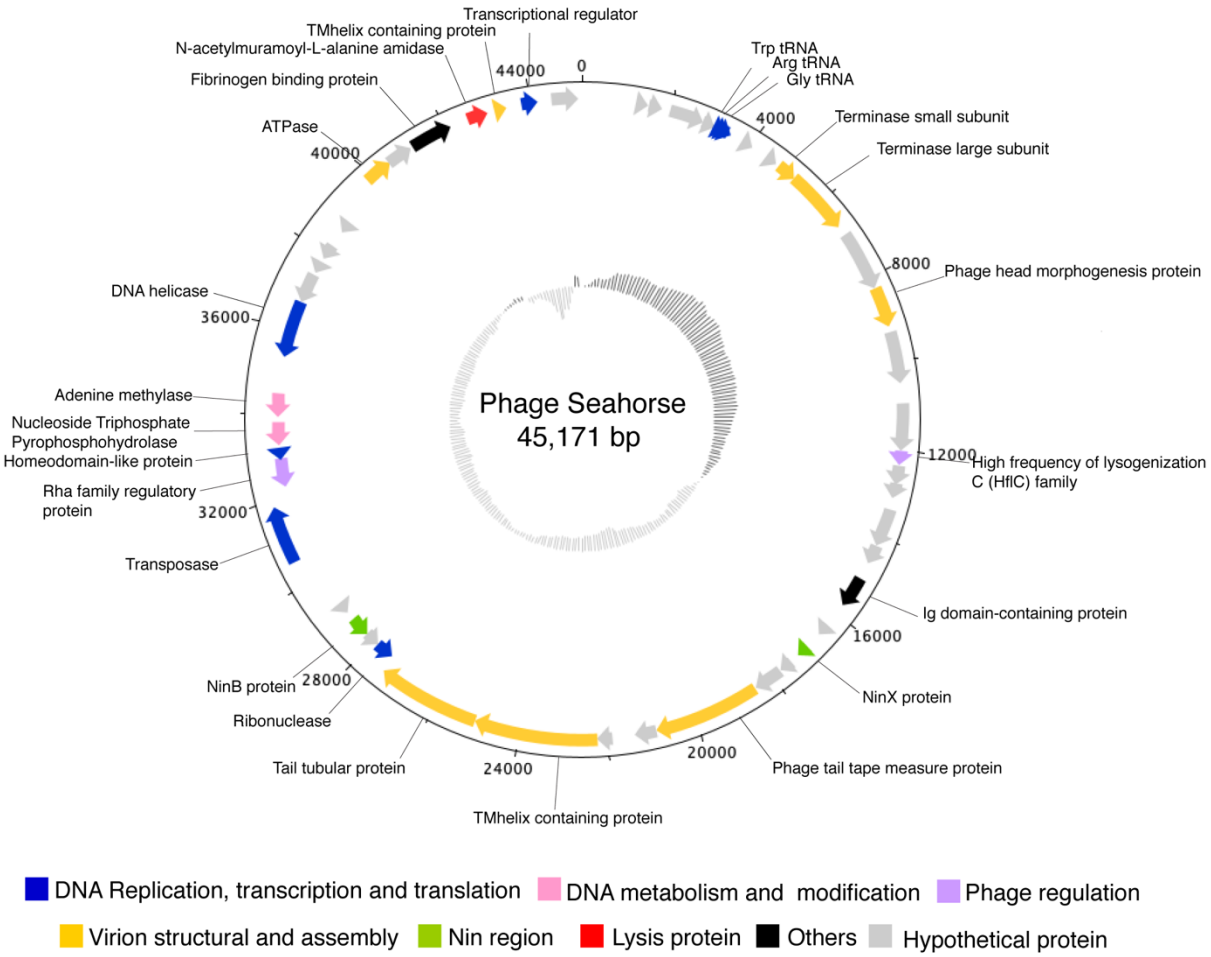

Figure 2. Genome map of phage Seahorse. The genome size is 45,171 base pairs long and the positions in term of base pairs are indicated by the number on the outermost circle. The grey scale on the innermost circle indicates GC content. The open reading frames (ORFs) are annotated and color-coded by their putative function; blue: DNA replication and transcription, and translation, pink: DNA metabolism and modification, purple: phage regulation, yellow: virion structural and assembly, green: Nin region, red: lysis protein, black: others, and grey: hypothetical proteins. The direction of arrows indicates gene arrangement in the genome.

ORF	Predicted function	Direction	Start	Stop	Size (n)	Sequence similarity	Accession no.	Source	E-value
ORF1	Hypothetical protein	+	1293	1496	204	Hypothetical protein NVP1103O_85 [Vibrio phage 1.103.O._10N.261.52.F2]	AUR87742.1	NCBI	6.00E-27
ORF2	Hypothetical protein	+	1514	1819	306	Hypothetical protein NVP1291O_36 [Vibrio phage 1.291.O._10N.286.55.F6]	AUS01750.1	NCBI	2.00E-46
ORF3	Hypothetical protein	+	2007	2786	780	Hypothetical protein NVP1263A_15 [Vibrio phage 1.263.A._10N.286.51.B1]	AUR99175.1	NCBI	3.00E-12
ORF4	Hypothetical protein	+	2787	3071	285	Hypothetical protein	168987	ACLAME	2.00E-07
ORF5	Hypothetical protein	+	3799	4032	234	Hypothetical protein [Vibrio phage LP.1]	AZU97916.1	NCBI	3.00E-14
ORF6	Hypothetical protein	+	4400	4681	282	Hypothetical protein ValSw33_31 [Vibrio phage ValSw3-3]	AVR75855.1	NCBI	3.00E-42
ORF7	Terminase small subunit	+	4761	5204	443	Phage(gi712916139); PHAGE_Shewan_3/49_NC_025466: terminase small subunit	PP_00071	PHASTER	7.35E-37
ORF8	Terminase large subunit	+	5194	6678	1484	phage(gi712915541); PHAGE_Shewan_1/41_NC_025458: terminase large subunit	PP_00070	PHASTER	0
ORF9	Hypothetical protein	+	6898	8274	1377	Hypothetical protein	184967	ACLAME	1.00E-71
ORF10	Phage head morphogenesis protein	+	8261	9190	929	MULTISPECIES: phage head morphogenesis protein [Vibrio]	WP_086959696.1	NCBI	1.00E-149
ORF11	Hypothetical protein	+	9312	10490	1179	Hypothetical protein	184946	ACLAME	2.00E-35
ORF12	Hypothetical protein	+	10936	12006	1071	Hypothetical protein	184931	ACLAME	3.00E-19
ORF13	High frequency of lysogenization C (HflC) family	+	12006	12332	327	High frequency of lysogenization C (HflC) family	YP_009275512.1	NCBI	1.33e-06
ORF14	Hypothetical protein	+	12339	12776	438	Hypothetical protein	184935	ACLAME	4.00E-13
ORF15	Hypothetical protein	+	12736	13089	354	Hypothetical protein	184932	ACLAME	2.00E-05
ORF16	Hypothetical protein	+	13355	14212	858	Hypothetical protein VPKG_00027 [Vibrio phage pYD21-A]	YP_007673989.1	NCBI	3.00E-71
ORF17	Hypothetical protein	+	14209	14652	444	Hypothetical protein ValSw33_31 [Vibrio phage ValSw3-3]	AVR75855.1	NCBI	3.00E-42
ORF18	Ig domain-containing protein	+	15028	15750	722	Uncharacterized conserved protein YjdB, contains Ig-like domain	COG5437	NCBI Conserved Domain Search	2.02E-05
ORF19	Hypothetical protein	+	16335	16598	264	Hypothetical protein NVP1116O_41 [Vibrio phage 1.116.O._10N.222.52.C10]	AUR88658.1	NCBI	2.00E-05
ORF20	NinX protein	+	16974	17261	287	NinX [Salmonella phage S102]	AXC39656.1	NCBI	7.00E-15
ORF21	Hypothetical protein	+	17466	17777	312	Hypothetical protein NVP1239O_45 [Vibrio phage 1.239.O._10N.261.52.F6]	AUR97481.1	NCBI	3.00E-08
ORF22	Hypothetical protein	+	17805	18461	657	Hypothetical protein	184973	ACLAME	3.00E-20
ORF23	Phage tail tape measure protein	+	18471	20900	2430	Lambda family phage tail tape measure protein	181776	ACLAME	5.00E-06
ORF24	Hypothetical protein	+	20900	21397	498	Hypothetical protein [Vibrio phage LP.2]	AZU97857.1	NCBI	3.00E-17
ORF25	Hypothetical protein	+	21903	22250	348	Hypothetical protein NVP1189B_19 [Vibrio phage 1.189.B._10N.286.51.B5]	AUR93845.1	NCBI	8.00E-23
ORF26	TMhelix containing protein	+	22238	25039	2801	TMhelix containing protein [Vibrio phage 1.110.O._10N.261.52.C1]	AUR88148.1	NCBI	3.00E-147
ORF27	Tail tubular protein	+	25039	27384	2345	tail tubular protein [Vibrio phage Athena1]	AUG84865.1	NCBI	2.00E-19
ORF28	Ribonuclease	-	27438	27878	441	Ribonuclease [Vibrio phage VaK]	ARH11752.1	NCBI	6.00E-46

ORF	Predicted function	Direction	Start	Stop	Size (n)	Sequence similarity	Accession no.	Source	E-value
ORF29	Hypothetical protein	-	27875	28228	354	Hypothetical protein NVP1254O_20 [Vibrio phage 1.254.O._10N.286.45.C8]	AUR98603. 1	NCBI	2.00E-20
ORF30	NinB protein	-	28225	28713	488	[Superfamily] cl21658 (PSSMID 328842) NinB protein	PRK09741	NCBI Conserved Domain Search	1.61E-37
ORF31	Hypothetical protein	-	28915	29139	225	Hypothetical protein ValSw33_20 [Vibrio phage ValSw3-3]	AVR75844.1	NCBI	5.00E-38
ORF32	Transposase	+	30555	31868	1313	PHAGE_Burkho_Bcep22_NC_005262: ISL3 family transposase; PP_00032; phage(gi38640338)	PP_00032	PHASTER	8.62E-64
ORF33	Rha family regulatory protein	-	32262	32933	671	Rha family regulatory protein [Vibrio phage 1.119.O._10N.261.51.A9]	AUR89012.1	NCBI	1.00E-94
ORF34	Homeodomain-like protein	-	32903	33175	272	Homeodomain-like protein	AUR86879.1	NCBI	2.00E-28
ORF35	Nucleoside Triphosphate Pyrophosphohydrolase	-	33254	33796	543	[Superfamily] cl16941 (PSSMID 354290) Nucleoside Triphosphate Pyrophosphohydrolase (EC 3.6.1.8) MazG-like domain superfamily	cd11542	NCBI Conserved Domain Search	8.02E-27
ORF36	Adenine methylase	-	33923	34483	560	Adenine methylase [Aeromonas phage 4_D05]	QDJ96121.1	NCBI	3.00E-90
ORF37	DNA helicase	-	35354	36724	1370	Replicative DNA helicase [Vibrio phage jenny 12G5]	AGN51428.1	NCBI	0
ORF38	Hypothetical protein	-	36721	37425	705	Hypothetical protein ValSw33_44 [Vibrio phage ValSw3-3]	AVR75868.1	NCBI	1.00E-68
ORF39	Hypothetical protein	-	37488	37733	246	Hypothetical protein S349_62 [Shewanella sp. phage 3/49]	YP_009103948.1	NCBI	1.00E-10
ORF40	Hypothetical protein	-	37871	38242	372	Hypothetical protein VPR_009 [Vibrio phage Vp_R1]	AUG88373.1	NCBI	5.00E-54
ORF41	Hypothetical protein	-	38629	38919	291	Hypothetical protein NVP1113A_38 [Vibrio phage 1.113.A._10N.286.51.E7]	AUR88439.1	NCBI	5.00E-31
ORF42	ATPase	+	39897	40544	647	ATPase [Aeromonas phage 2_D05]	QDB73849.1	NCBI	2.00E-99
ORF43	Hypothetical protein	+	40525	41121	597	Hypothetical protein	166167	ACLAME	2.00E-26
ORF44	Fibrinogen binding protein	+	41169	42131	962	Fibrinogen binding protein [Vibrio phage 1.013.O._10N.286.54.F9]	AUR81803.1	NCBI	3.00E-137
ORF45	N-acetylmuramoyl-L-alanine amidase	+	42558	43019	461	N-acetylmuramoyl-L-alanine amidase [Vibrio phage 1.232.O._10N.261.51.E11]	AUR96787.1	NCBI	3.00E-51
ORF46	TMhelix containing protein	+	43209	43460	251	TMhelix containing protein [Vibrio phage 1.134.O._10N.222.52.B8]	AUR89889.1	NCBI	3.00E-23
ORF47	Transcriptional regulator	+	43798	44172	375	Transcriptional regulator	184491	ACLAME	5.00E-06
ORF48	Hypothetical protein	+	44476	45090	615	Hypothetical protein ValSw33_24 [Vibrio phage ValSw3-3]	AVR75848.1	NCBI	2.00E-28

Table 2. List of annotated proteins from ORFs in the genome of phage Seahorse. ORFs with the predicted functions were determined by their significant hit (E-value < 10^{-4}) against genome databases.

Phage Seahorse infection triggers the condensation of host nucleoid

To investigate how phage Seahorse hijacks and kills the host VP_{APHND}, a single cell-leveled assay was used to visualize the bacterial cells upon the phage infection. We first focused on a 30-minute post infection (mpi) window because the one-step growth curve suggests that the phage replicates inside the host for only approximately 30 minutes before cell lysis (Fig. 1g). Fluorescence microscopy of Seahorse infected VP_{APHND} revealed a nonuniformly distributed nucleoid at time zero (0 mpi, lower panel; Fig. 3a), identical to the uninfected VP_{APHND} control (0 mpi, upper panel; Fig. 3a). Over intervals of 10 mpi, this distributed nucleoid became more condensed as infection progressed until 30 mpi in which it appeared as a single sphere (30 mpi, lower panel; Fig. 3a). During late infection (after 30 mpi), some

unlysed infected cells contained multiple nucleoids exhibiting an archetypal toroid shape (upper panel; Fig. 3b). Similar to a previous study in *Pseudomonas chlororaphis* phage 201Phi2-1, the bacterial host cells lysed at a late time point resulting in the release of phage particles appearing as puncta (blue) surrounding cell debris (red) suggesting the complete lytic cycle of the phage (lower panel; Fig. 3b)[13]. We observed no evidence of condensed DNA ("blob") or toroid formation in the control cells (Figs. 3a and S4; n = 1,782).

To rule out the possibility that the observed nucleoid condensation is caused by host cell membrane leakage, previously seen in pore-forming molecules such as nisin and calcimycin[4], we investigated the membrane integrity of infected cells by testing cell permeability to the DNA staining dye, SYTOX-green. Our result showed that the DNA blob in the infected cells was not stained by SYTOX-green, indicating that the cell membrane remained intact throughout infection, further supporting that phage Seahorse is the cause of the blob DNA formation, not the cell membrane leakage (Fig. 3c).

To confirm that the condensed nucleoid seen in the phage-infected cell is host bacterial DNA, we performed time-lapse fluorescence microscopy over a 30-minute infection period using live cell permeant SYTO 16 DNA dye. At the beginning of infection, the host nucleoid (green) appeared diffuse, similar to the uninfected cell control (Fig. 3d). Over the first 10 minutes, the nucleoid decondensed, seen by the diffusion and reduction of signal within the cell. Beginning at 15 mpi, the DNA nucleoid condensed and eventually appeared in a sphere at the midcell by 30 mpi, identical to the structure seen the infected cell shown in Fig. 3a. This time-lapse observation mirrors the morphological change in the DNA of fixed infected cells conducted over the same time course as shown in Fig. 3a. Altogether, these results suggest that phage Seahorse possibly interferes with the host cellular machineries in which it triggers the morphology change of host DNA.

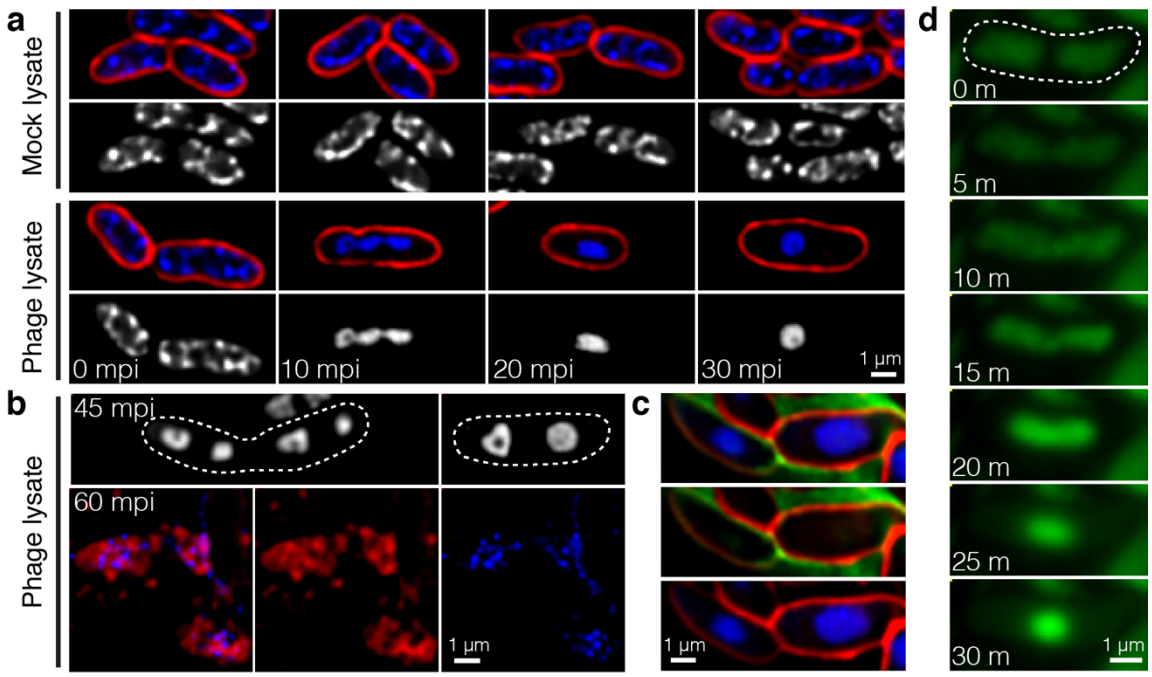

Figure 3. Single cell-leveled assay revealing the formation of blob and toroid of host DNA inside the phage- infected cells. Bacterial cells were grown in liquid culture to log phase and infected by phage Seahorse at MOI 5. At desired time points, the bacterial cells were harvested and fixed. For live cell imaging, the cells were inoculated on an agar pad after the phage infection. Prior to fluorescence microscopy, cell membrane (red) and nucleoid (blue/grey) were stained by FM4–64 and DAPI, respectively. (**a**) Fluorescence images of fixed bacterial cells in the presence of mock lysate (upper panel) and phage lysate (lower panel) at various time points. (**b**) Still images of phage-infected cells during late

infection; 45 mpi (upper panel) and 60 mpi (lower panel). (**c**) Live cell images of phage-infected cells. SYTOX-green as impermeable DNA staining dye was used as an indicator of live cells. (**d**) Time-lapse imaging of phage-infected cells over the course of 30 minutes. Nucleoid (green) as stained by SYTO 16 condensed and became blob shaped as early as 25 minutes. Dashed lines indicate cell borders. Scale bars equal to 1 micron.

Inhibition of protein translation resulted in blob and toroid structure formation of the bacterial chromosome

As previously reported by Nonejuie *et al*.[4], fluorescence microscopy-based method, bacterial cytological profiling (BCP), can be used to identify biosynthetic pathways of bacteria that are inhibited based on characteristic cell morphological changes. We therefore applied the principle of BCP to investigate which metabolic pathway of VP_{AHPND} is targeted during the phage Seahorse infection by fluorescence microscopy. Since phages are believed to hijack host DNA replication, RNA transcription, and protein translation pathways during the lytic cycle[14], we focused on antibiotics that also inhibit these major pathways. Ciprofloxacin, rifampicin, and tetracycline were used as inhibitors to replication, transcription, and translation respectively. Fluorescence microscopy results of VP_{AHPND} treated with antibiotics showed that each antibiotic treatment led to a unique morphological change in VP_{AHPND}, similar to what previously observed in gram-negative *Escherichia coli* and *Acinetobactor baumannii* treatments[4,15]. Upon ciprofloxacin treatment, inhibition of DNA replication resulted in cell elongation and DNA pooling at the midcell while treatment with rifampicin resulted in DNA decondensation (Fig. 4a). Tetracycline-treated cells exhibited the signature condensed and toroidal-shaped DNA at 30 minutes but more prominently at 60 minutes post treatment with an intact cell membrane (Figs. 4a and S5). This morphology upon tetracycline treatment is notably similar to the condensed DNA morphology of the bacterial cells infected by phage Seahorse (lower panel; Fig. 3a).

The production of “condensed” DNA upon infection instead of perfect “toroidal” shaped DNA urged us to ask if the condensed DNA morphology is truly the result of protein translation inhibition (lower panel, 10–30 mpi; Fig. 3a). The archetypal DNA shape of protein translation inhibition in many studies is a “toroid”[4,15,16] but DNA shape alteration during very early translation inhibition by an antibiotic (less than one hour) has never been reported. Thus, time-course analysis of toroidal DNA formation in VP_{AHPND} during tetracycline treatment was performed. This resulted in a more “condensed” DNA morphology that changed over time with the eventual appearance of the signature “toroid” DNA at 30 minutes post treatment and it became increasingly prominent at 60 minutes (Fig. 4b). Due to the fact that the phage Seahorse had a short latent period and completed its lytic cycle by 30 mpi, it is then reasonable to assume that the toroid DNA morphology was merely undetectable in infected cells because the host cell lysed before toroids were formed. Simply put, if it was able to progress beyond 30 mpi, the nucleoid would have resembled a toroid shape seen in Fig. 4b (45 mpi; Fig. 3b). Altogether, these results suggest that DNA condensation morphology observed in phage Seahorse-infected VP_{AHPND} is likely due to the protein translation inhibition caused by the phage hijacking mechanism.

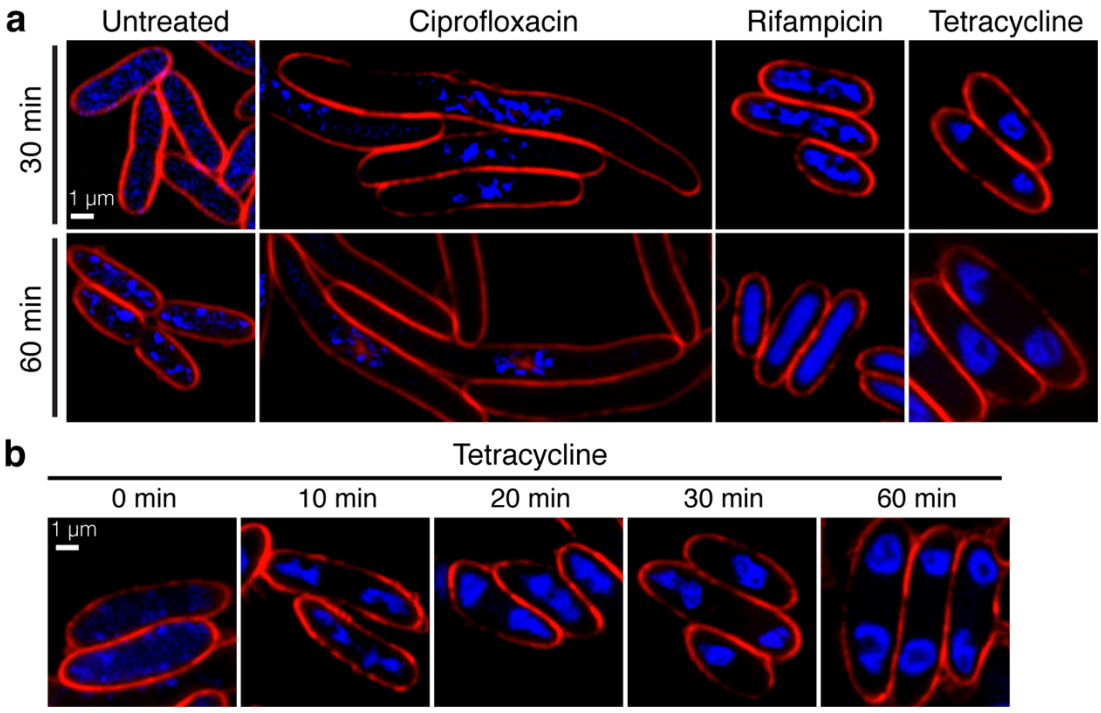

Figure 4. Fluorescence microscopy showed unique morphology of bacterial cells during the antibiotic treatment targeting different cellular pathways. Bacterial cells during the log phase were treated with antibiotics (ciprofloxacin, rifampicin, and tetracycline) at 5X MIC for indicated period of time. At desired time points, the cells were fixed and stained with FM4–64 (red) and DAPI (blue) prior to fluorescence microscopy. (**a**) Fluorescence images of fixed bacterial cells after the treatment with different antibiotics at 30 minutes (upper panel) and 60 minutes (lower panel). (**b**) Time-course still images of tetracycline-treated bacterial cells. Scale bars equal to 1 micron.

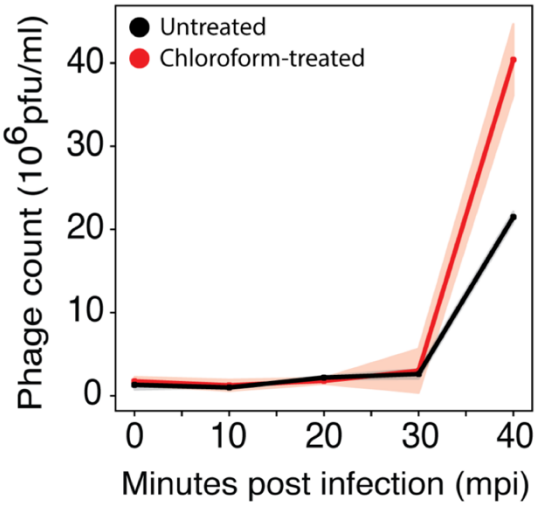

Supplemental Figure 1: One-step growth curve of phage Seahorse in comparison between untreated (black line) and chloroform-treated samples (red line). The experiment was performed in at least 3 independent biological replicates and the data are represented as the mean ± standard deviation.

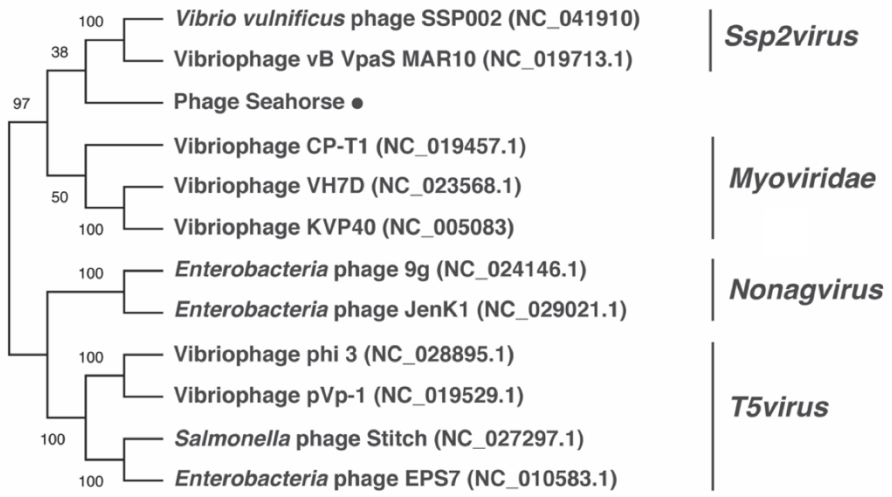

Supplemental Figure 2: Phylogenetic tree showing the relationship between terminase large subunits of different phages as indicated in the tree. Selected bootstrap values are shown at major branches. The viral classification: Ssp2virus, Myoviridae, Nonagvirus, and T5virus, is shown at each clustered group. A closed circle indicates the branch of terminase large subunit of phage Seahorse.

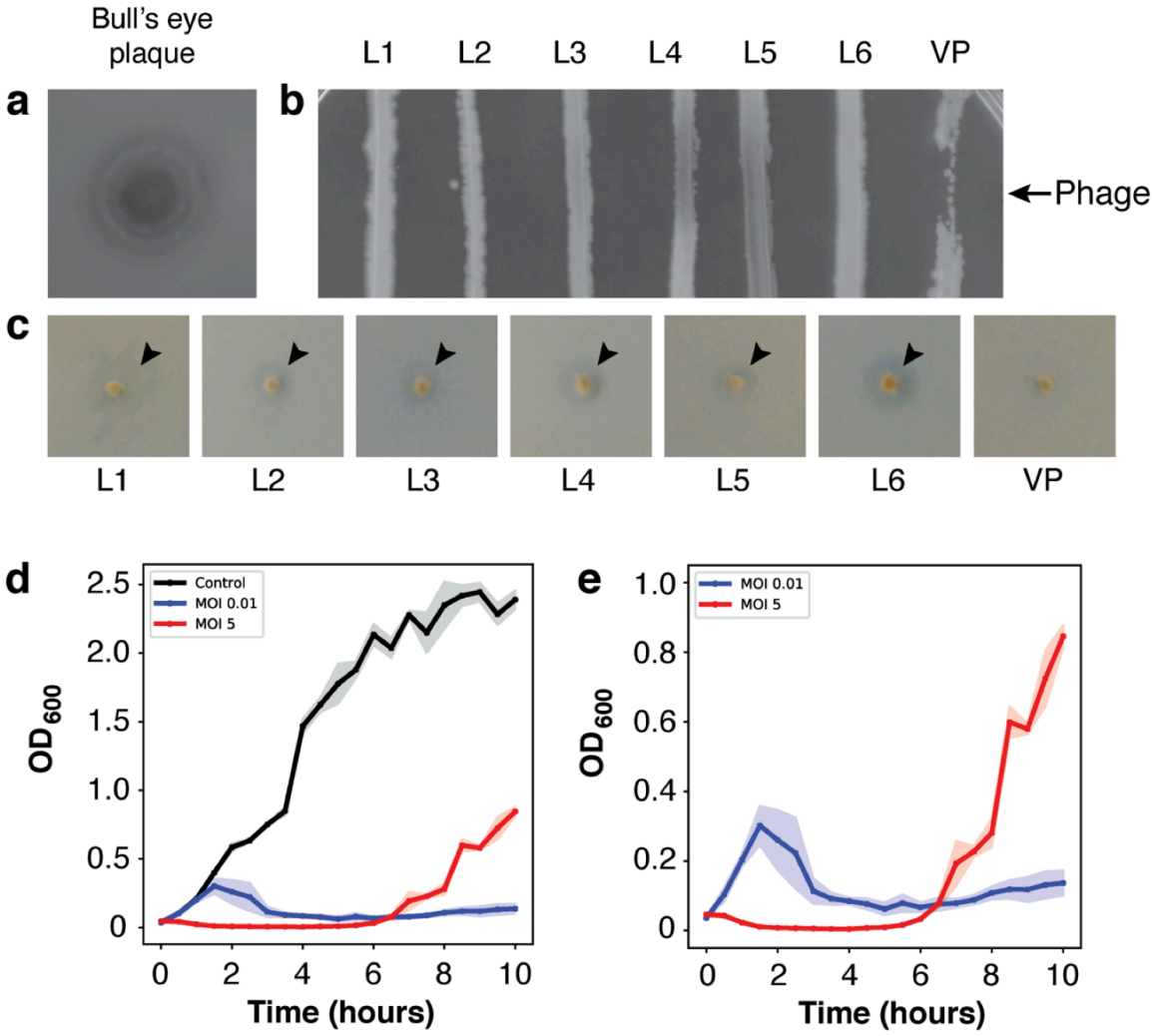

Supplemental Figure 3: Lysogeny experiment of phage Seahorse. (a) A spot test exhibiting a signature clear zone of temperate phages - "Bull's eye". (b) A cross-streak experiment of phage resistant isolates (L1 – L6) and the bacterial control (VP). Arrow indicates where high titer phage lysate was spotted atop the streaks. (c) Production of phage progeny from isolated lysogens. Arrowheads indicate clear zones as a result of host cell lysis. (d,e) The bacterial cell lysis profile of VP_{AHPND} in the presence of phage at MOI 0 (Control, black line), MOI 0.01 (blue line), and MOI 5 (red line).

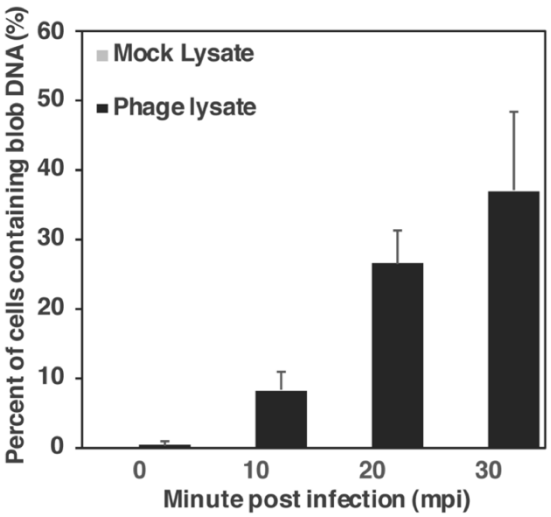

Supplemental Figure 4: A graph showing the increase of number of VP_{AHPND} cell containing blob-shaped DNA during the phage Seahorse infection.

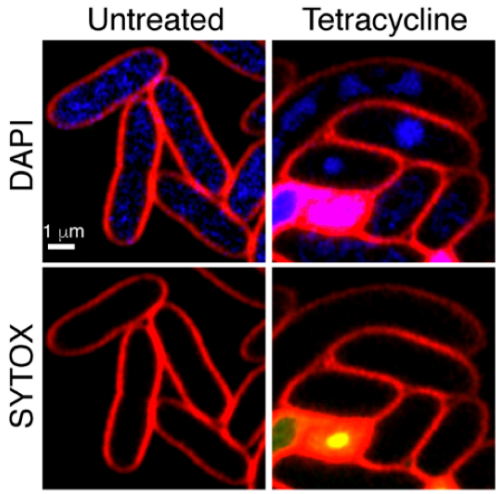

Supplemental Figure 5: Fluorescence images of live cells of VP_{AHPND} treated with tetracycline. Bacteria cells were treated with tetracycline for 60 minutes. SYTOX-green was used to stain DNA as an indicator for the cells with permeabilized membrane. Upper panels show FM4-64 (red) and DAPI (blue) staining while lower panels show FM4-64 (red) and SYTOX-green (green) stains. Scale bar equals to 1 micron.

Table S1: Antibiotics used in this study showing antibiotic class, MIC and drug target.

Antibiotic Class	Antibiotic Name	MIC (µg/ml)	Target
DNA Synthesis Inhibitor			
Fluoroquinolone	Ciprofloxacin	0.375	DNA gyrase A
RNA Transcription Inhibitor			
Rifamycin	Rifampicin	0.375	DNA-dependent RNA polymerase
Protein Synthesis Inhibitors			
Tetracycline	Tetracycline	0.5	30S ribosome (inhibit aminoacyl tRNA binding)

Table S2: A summary table of latent period, burst size, and tolerance of selected vibriophages

Phage name	Host	Stains	Latent Period (Minutes)	Burst Size (Particle/Cell)	Infectivity at pH	Infectivity at Temp (°C)
VP-1	*V. parahaemolyticus*	Non-specified strain	120	9	-	-
VP-2	*V. parahaemolyticus*	Non-specified strain	90	15	-	-
VP-3	*V. parahaemolyticus*	Non-specified strain	40	42	-	-
VpKK5	*V. parahaemolyticus*	ATCC17802 and 15 isolates	36	180	4 to 9	40
VhKM4	*V. parahaemolyticus*	ATCC 17802	60	52	-	-
VVP1	*V. parahaemolyticus*	N1A and N7A	20-30	-	6 to 12	4 to 55
pVp-1	*V. parahaemolyticus*	AHPND (22 strains)	15	47	5 to 11	20 to 50
ϕVP-1	*V. parahaemolyticus*	SV4	10	44	7 to 9	4 to 70
vB_ValP_IME271	*V. alginolyticus*	1651	90	40	8	40
Vp670	*V. alginolyticus*	E06333	30	84	-	-
Φa318	*V. alginolyticus*	ATCC 17749	15	72	-	lower than 50
pVa-21	*V. alginolyticus*	rm-8402	70	58	5 to 9	4 to 50
vB_VspP_pVa5	*V. splendidus*	VaAn	30	24	-	-
H188	*V. kanaloae*	LMG 20539(T)	96	3	4 to 12	30 to 70
BONAISHI	*V. coralliilyticus*	LMG20984	120-180	8 and 19	3 to 10	4 to 50
Seahorse	***V. parahaemolyticus***	**AHPND (TM)**	**30**	**72**	**4 to 10**	**20 to 60**

Conclusion and Discussion

A new strain of *V. parahaemolyticus*, called VP_{APHND}, emerged in 2009 as a devastating pathogen to shrimp, causing acute hepatopancreatic necrosis disease (AHPND) or early mortality syndrome (EMS). The infection resulted in mass production losses in southern China and within several years, the incidence of VP_{APHND} infection had expanded to other neighboring countries such as Vietnam, Malaysia and Thailand[17]. The disease contributes to 100% mortality of shrimp within one week and the infected animals present an atrophied and discolored hepatopancreas due to the *Photorhabdus* insect-related (Pir) binary toxins ($PirA^{vp}$/$PirB^{vp}$), which are encoded on the virulent plasmid of the pathogen. The toxins degenerate the tubule epithelial cells of the hepatopancreas leaving the diseased animals susceptible to additional bacterial infections[18,19].

Due to the emergence of VP_{AHPND} and its multidrug resistant isolates, effective tools to control and combat these pathogens are urgently needed. Most recently, Angulo *et al*. revealed a number of studies and research reports on using phages as a biocontrol for the wide spread of VP_{AHPND}[20]. Until now, even though many phages have been reported to target *V. parahaemolyticus*, only phage pVp-1 has been found to effectively kill VP_{AHPND}. Phage pVp-1 is highly potent and lyses more than 90% out of the VP_{AHPND} strains that were isolated from Vietnam, Mexico, Costa Rica, Honduras, and Central America Countries[21]. However, the bacterial strain isolated from Thailand is not targeted by the pVp-1 phage. In this study, we successfully isolated a novel phage (named “Seahorse”) that specifically infects the

VP_{AHPND} strain isolated in Thailand. This study also elucidates that the phage is able to hijack protein translation machinery of the host bacteria. In comparison to other phages that infect vibrios (Table S2)[22–28], phage Seahorse has relatively big burst size with a shorter latency period than phages VP-1, VP-2, VP-3, VpKK5, and VhKM4 that replicate in *V. parahaemolyticus*[21,29–33]. It is also tolerant to the wide range of pHs and temperatures compared to other vibriophages suggesting unique survivability in harsh natural environments. These infectious characteristics not only add phage Seahorse to the library of phage targeting VP_{AHPND} but also make it a potential candidate for a biocontrol agent.

Bacteriophage requires a bacterial host cell to replicate, manipulating the native biosynthesis machinery of the host to assemble its own progeny. During its reproduction process, various phage-encoding proteins are produced to redirect or inhibit the host metabolism at the molecular level to benefit its fitness. These phage-derived proteins not only target the major metabolic pathways but are also capable of lysing the host cell membrane. Due to nature of these effects, these proteins can be considered antimicrobial agents similar to that of antibiotics with possible therapeutic applications[12]. Phage Seahorse was classified in the family *Siphoviridae* due to characteristics of the flexible, noncontractile tail with a non-enveloped icosahedral capsid. In addition, at high resolution near a native-state by Cryo-ET, unique spikes and fibers (a shaft with a sphere at the tip) on the phage capsid were observed. This is not the first time that this structure has been reported[5–8]. These are most likely structurally diverse glycoproteins encoded by the phage and thought to promote tethering of the viral capsid to receptors present on the host cell surface. For instance, in the case of human adenoviruses, the fibers have a long shaft with a knob at the distal end of the capsid whereas, in phage Phi29 and some bovine adenoviruses, they consist of only a protruding stem without a terminal sphere[5,6,8,34,35]. Moreover, phage Sf6 that infects *Shigella flexneri* has an identical shaft-knob structure at the tail terminus called the "tail needle knob"[36]. Due to the narrow host spectrum of phage Seahorse, the capsid spikes and fibers located on the surface of the phage capsid serve a potential role in host specificity and recognition.

Unfortunately, in a therapeutic context, phage Seahorse is not appropriate for application due to the ability to enter lysogenic cycle which renders the phage unsafe for treatment. Phage Seahorse appeared phylogenetically related to the temperate phage MAR10 that belongs to the genus *Ssp2virus* and targets *V. parahaemolyticus* (Fig. S2)[37,38]. This reassures our conclusion that phage Seahorse is temperate and also suggests the possible viral family it belongs to. Moreover, due to the lack of bioinformatics in phage related databases, the majority of the ORFs annotated in the phage Seahorse genome were predicted as unknown. As they might produce unwanted products or other unknown virulence factors, the therapeutic application is not warranted unless the fundamental knowledge in phage biology is better established or the phage is engineered to strictly enter only the lytic cycle[39].

However, despite the therapeutic shortcomings of phage Seahorse itself, phage genomes generally are considered an untapped resource for antimicrobials due to the metabolic hijacking ability and lytic capacity of the proteins they encode[40,41]. For example, from our genome analysis, albeit its relatively small genome, we were able to identify a lysis-related enzyme, N-acetylmuramoyl-L-alanine amidase, from ORF45. This lysis enzyme is involved in the cleavage of a very common bond present in most bacterial cell membranes, thus serving a crucial role in cell lysis[12]. In fact, it has been reported that the application of recombinant phage lysis enzymes from vibriophages can target a wider spectrum of bacterial hosts as compared to the parental phages[42,43]. Therefore, there is a strong possibility of finding other antibacterial protein candidate from this small phage in the future. Determining whether or not other hypothetical proteins found in the phage Seahorse genome and other newly discovered phage exhibit antibacterial activity needs further investigation.

With the lysis-related enzyme in mind, we set out to investigate whether the phage Seahorse genome encoded other proteins that targeted major host metabolic pathways during its lytic cycle. Bacterial morphological changes have been used as indicators for various physiological states of bacteria elicited by genetic alteration or stress response[4,44,45].

BCP exploits these cell morphological change patterns under different stresses to identify the specific mechanism being targeted by an antibiotic that causes bacterial growth inhibition. This study, for the first time, applied the principle of BCP technique to identify the underlying effected pathway and found that phage Seahorse likely inhibits protein translation of VP_{AHPND} at the early stage of infection. This finding is concomitant with other reported hijacking mechanisms that use phage-host protein-protein interactions to inhibit host machineries (i.e. replication, transcription and translation) with the effect of disarming host defenses and producing its own proteins for reproduction[46]. Thus, the hijacking model of host protein machinery in favor of phage protein production right after infection is plausible. For example, *Pseudomonas aeruginosa* phage PaP3 strongly suppresses host protein synthesis through the reduction of ribosome to preserve energy[47]. Our finding does not directly indicate that native host replication and transcription are not also inhibited during the infection. To date, BCP has never been applied to study replication, transcription and translation inhibition simultaneously or chronologically. Thus, it is possible that host replication and transcription machineries were inhibited but only the profound protein translation inhibition phenotype was detected. Whether or not a temporal hijacking mechanism is presented during different stages of infection requires further investigation.

Our study revealed the formation of host toroidal nucleoids that are likely the result of encoded phage proteins that hijack host translation machinery before cell lysis, as we called it: “Mechanism of pre-killing (MOK)”. This study suggests that the phage Seahorse genome contained at least one product that was involved in the inhibition towards a protein biosynthesis pathway. Further investigation into which of the phage-derived proteins target important pathways of the bacterial host will be needed in order to identify these antimicrobial proteins for development as therapeutics against pathogens. Localization profiling of phage proteins inside the host, as we previously reported[1,48], could also be utilized to study Seahorse-infected cells to gain a better understanding of how individual phage-encoded proteins temporally and spatially function within the host. These investigations could help overcome Seahorse’s therapeutic shortcomings while identifying novel antimicrobial agents at the molecular level.

Data availability

All data generated or analyzed in this study are included in this article and its supplementary information files. Nucleotide sequence of the phage Seahorse genome was deposited in GenBank database with the accession number MN512538.

Acknowledgements

This research was supported by the Thailand Research Fund and the Office of the Higher Education Commission MRG6180027 (V.C.), the Grant for Development of New Faculty Staff, Ratchadaphiseksomphot Endowment Fund (V.C.), and National Institutes of Health grant GM129245 (J.P.). This study was supported in part by the Japan Science and Technology Agency (JST)/Japan International Cooperation Agency (JICA), Science and Technology Research Partnership for Sustainable Development, SATREPS JPMJSA1806 (V.C.). P.N. was supported by the Thailand research fund and the office of the higher education commission (MRG6080081). We acknowledge Chulalongkorn University for its support of the Center of Excellence for Molecular Biology and Genomics of Shrimp. We used the UCSD Cryo-Electron Microscopy Facility (supported by NIH grant R01-GM33050 to Dr. Timothy S. Baker and the Agouron Institute) and the fluorescence microscopy facility at the Advanced Cell Imaging Center, Institute of Molecular Biosciences, Mahidol University. We would like to thank John P. Davis and Savannah Senecal for bench-work assistance and helping with intellectual discussion, and Prof. Dr. Sirirat Rengpipat at Department of Microbiology, and Assoc. Prof. Dr. Kunlaya Somboonwiwat at Department of Biochemistry, Faculty of Science, Chulalongkorn University for offering *Vibrio* strains for host range determination.

Current research and future direction

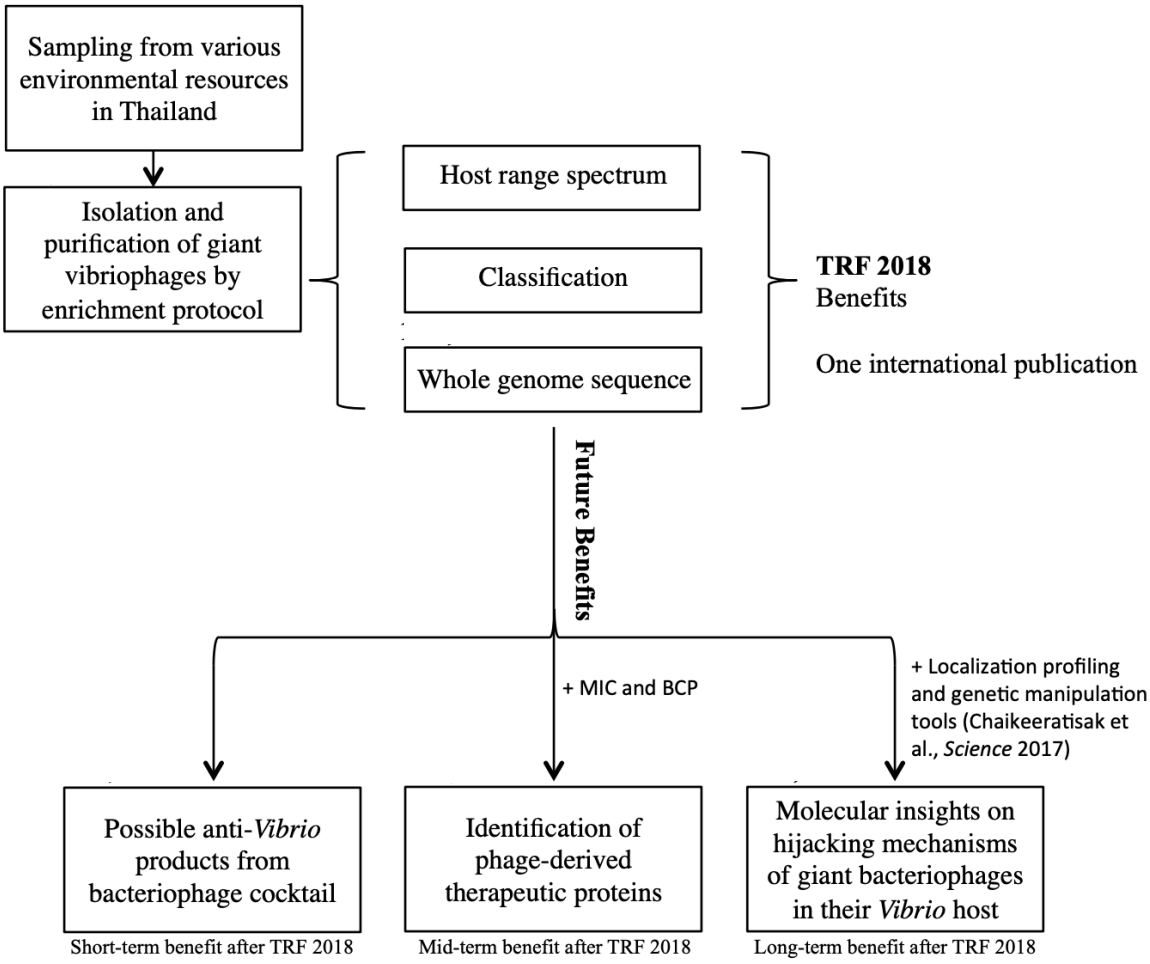

References

1. Chaikeeratisak, V. *et al.* The phage nucleus and tubulin spindle are conserved among large *Pseudomonas* phages. *Cell Rep.* **20**, 1563–1571 (2017).
2. Junprung, W., Supungul, P. & Tassanakajon, A. HSP70 and HSP90 are involved in shrimp *Penaeus vannamei* tolerance to AHPND-causing strain of Vibrio parahaemolyticus after non-lethal heat shock. *Fish Shellfish Immunol.* **60**, 237–246 (2017).
3. Kumar, S., Stecher, G., Li, M., Knyaz, C. & Tamura, K. MEGA X: molecular evolutionary genetics analysis across computing platforms. *Mol. Biol. Evol.* **35**, 1547–1549 (2018).
4. Nonejuie, P., Burkart, M., Pogliano, K. & Pogliano, J. Bacterial cytological profiling rapidly identifies the cellular pathways targeted by antibacterial molecules. *Proc. Natl. Acad. Sci.* **110**, 16169–16174 (2013).
5. Cheng, L. *et al.* Cryo-EM structures of two bovine adenovirus type 3 intermediates. *Virology* **450**, 174–181 (2014).
6. Xiang, Y. & Rossmann, M. G. Structure of bacteriophage φ29 head fibers has a supercoiled triple repeating helix-turn-helix motif. *Proc. Natl. Acad. Sci.* **108**, 4806–4810 (2011).
7. Van Raaij, M. J., Mitraki, A., Lavigne, G. & Cusack, S. A triple β-spiral in the adenovirus fibre shaft reveals a new structural motif for a fibrous protein. *Nature* **401**, 935–938 (1999).
8. Liu, H. *et al.* Atomic structure of human adenovirus by cryo-EM reveals interactions among protein networks. *Science* **329**, 1038–1043 (2010).

9. Kihara, A., Akiyama, Y. & Ito, K. Host regulation of lysogenic decision in bacteriophage λ: transmembrane modulation of FtsH (HflB), the cII degrading protease, by HflKC (HflA). *Proc. Natl. Acad. Sci.* **94**, 5544–5549 (1997).
10. Noble, J. *et al.* The *Escherichia coli* hflA locus encodes a putative GTP-binding protein and two membrane proteins, one of which contains a protease-like domain. *Proc. Natl. Acad. Sci.* **90**, 10866–10870 (1993).
11. Dyson, Z. A. *et al.* Locating and activating molecular 'time bombs': Induction of Mycolata prophages. *PloS One* **11**, (2016).
12. Borysowski, J., Weber-Dąbrowska, B. & Górski, A. Bacteriophage endolysins as a novel class of antibacterial agents. *Exp. Biol. Med.* **231**, 366–377 (2006).
13. Kraemer, J. A. *et al.* A phage tubulin assembles dynamic filaments by an atypical mechanism to center viral DNA within the host cell. *Cell* **149**, 1488–1499 (2012).
14. Parmar, K. M., Gaikwad, S. L., Dhakephalkar, P. K., Kothari, R. & Singh, R. P. Intriguing interaction of bacteriophage-host association: an understanding in the era of omics. *Front. Microbiol.* **8**, 559 (2017).
15. Htoo, H. H. *et al.* Bacterial cytological profiling as a tool to study mechanisms of action of antibiotics that are active against *Acinetobacter baumannii*. *Antimicrob. Agents Chemother.* **63**, e02310-18 (2019).
16. Nonejuie, P. *et al.* Application of bacterial cytological profiling to crude natural product extracts reveals the antibacterial arsenal of *Bacillus subtilis*. *J. Antibiot. (Tokyo)* **69**, 353 (2016).
17. Thitamadee, S. *et al.* Review of current disease threats for cultivated penaeid shrimp in Asia. *Aquaculture* **452**, 69–87 (2016).
18. Boonyawiwat, V. *et al.* Impact of farm management on expression of early mortality syndrome/acute hepatopancreatic necrosis disease (EMS/AHPND) on penaeid shrimp farms in Thailand. *J. Fish Dis.* **40**, 649–659 (2017).
19. De Schryver, P., Defoirdt, T. & Sorgeloos, P. Early mortality syndrome outbreaks: a microbial management issue in shrimp farming? *PLoS Pathog.* **10**, (2014).
20. Angulo, C., Loera-Muro, A., Trujillo, E. & Luna-González, A. Control of AHPND by phages: a promising biotechnological approach. *Rev. Aquac.* **11**, 989–1004 (2019).
21. Jun, J. W. *et al.* Potential application of bacteriophage pVp-1: agent combating *Vibrio parahaemolyticus* strains associated with acute hepatopancreatic necrosis disease (AHPND) in shrimp. *Aquaculture* **457**, 100–103 (2016).
22. Li, F. *et al.* Genomic and biological characterization of the Vibrio alginolyticus-infecting "Podoviridae" bacteriophage, vB_ValP_IME271. *Virus Genes* **55**, 218–226 (2019).
23. Luo, P. *et al.* Complete genomic sequence of the *Vibrio alginolyticus* bacteriophage Vp670 and characterization of the lysis-related genes, cwlQ and holA. *BMC Genomics* **19**, 1–11 (2018).
24. Lin, Y.-R., Chiu, C.-W., Chang, F.-Y. & Lin, C.-S. Characterization of a new phage, termed φA318, which is specific for *Vibrio alginolyticus*. *Arch. Virol.* **157**, 917–926 (2012).
25. Kim, S. G. *et al.* Isolation and characterisation of pVa-21, a giant bacteriophage with anti-biofilm potential against *Vibrio alginolyticus*. *Sci. Rep.* **9**, 1–10 (2019).
26. Katharios, P., Kalatzis, P. G., Kokkari, C., Sarropoulou, E. & Middelboe, M. Isolation and characterization of a N4-like lytic bacteriophage infecting *Vibrio splendidus*, a pathogen of fish and bivalves. *PloS One* **12**, (2017).
27. Li, Y. *et al.* Complete genomic sequence of bacteriophage H188: A novel *Vibrio kanaloae* phage isolated from Yellow Sea. *Curr. Microbiol.* **72**, 628–633 (2016).
28. Jacquemot, L. *et al.* Therapeutic potential of a new jumbo phage that infects *Vibrio coralliilyticus*, a widespread coral pathogen. *Front. Microbiol.* **9**, 2501 (2018).
29. Mateus, L. *et al.* Efficiency of phage cocktails in the inactivation of *Vibrio* in aquaculture. *Aquaculture* **424**, 167–173 (2014).
30. Lal, T. M., Sano, M. & Ransangan, J. Genome characterization of a novel vibriophage VpKK5 (*Siphoviridae*) specific to fish pathogenic strain of Vibrio parahaemolyticus. *J. Basic Microbiol.* **56**, 872–888 (2016).

31. Lal, T. M., Sano, M. & Ransangan, J. Isolation and characterization of large marine bacteriophage (*Myoviridae*), VhKM4 infecting Vibrio harveyi. *J. Aquat. Anim. Health* **29**, 26–30 (2017).
32. Stalin, N. & Srinivasan, P. Characterization of *Vibrio parahaemolyticus* and its specific phage from shrimp pond in Palk Strait, South East coast of India. *Biologicals* **44**, 526–533 (2016).
33. Matamp, N. & Bhat, S. G. Genome characterization of novel lytic *Myoviridae* bacteriophage φVP-1 enhances its applicability against MDR-biofilm-forming Vibrio parahaemolyticus. *Arch. Virol.* **165**, 387–396 (2020).
34. Xu, J., Wang, D., Gui, M. & Xiang, Y. Structural assembly of the tailed bacteriophage φ29. *Nat. Commun.* **10**, 1–16 (2019).
35. Yu, X. *et al.* Cryo-EM structure of human adenovirus D26 reveals the conservation of structural organization among human adenoviruses. *Sci. Adv.* **3**, e1602670 (2017).
36. Bhardwaj, A., Molineux, I. J., Casjens, S. R. & Cingolani, G. Atomic structure of bacteriophage Sf6 tail needle knob. *J. Biol. Chem.* **286**, 30867–30877 (2011).
37. Lee, H. S., Choi, S., Shin, H., Lee, J.-H. & Choi, S. H. Vibrio vulnificus bacteriophage SSP002 as a possible biocontrol agent. *Appl Env. Microbiol* **80**, 515–524 (2014).
38. Villa, A. A., Kropinski, A. M., Abbasifar, R., Abbasifar, A. & Griffiths, M. W. Genome sequence of temperate *Vibrio parahaemolyticus* bacteriophage vB_VpaS_MAR10. (2012).
39. Dedrick, R. M. *et al.* Engineered bacteriophages for treatment of a patient with a disseminated drug-resistant Mycobacterium abscessus. *Nat. Med.* **25**, 730–733 (2019).
40. Liu, J. *et al.* Antimicrobial drug discovery through bacteriophage genomics. *Nat. Biotechnol.* **22**, 185–191 (2004).
41. Drulis-Kawa, Z., Majkowska-Skrobek, G. & Maciejewska, B. Bacteriophages and phage-derived proteins–application approaches. *Curr. Med. Chem.* **22**, 1757–1773 (2015).
42. Wang, W., Li, M., Lin, H., Wang, J. & Mao, X. The *Vibrio parahaemolyticus*-infecting bacteriophage qdvp001: genome sequence and endolysin with a modular structure. *Arch. Virol.* **161**, 2645–2652 (2016).
43. Zermeño-Cervantes, L. A., Makarov, R., Lomelí-Ortega, C. O., Martínez-Díaz, S. F. & Cardona-Félix, C. S. Recombinant Lys VPMS 1 as an endolysin with broad lytic activity against *Vibrio parahaemolyticus* strains associated to acute hepatopancreatic necrosis disease. *Aquac. Res.* **49**, 1723–1726 (2018).
44. Ultee, E., Ramijan, K., Dame, R. T., Briegel, A. & Claessen, D. Stress-induced adaptive morphogenesis in bacteria. *Adv Microb Physiol* **74**, 97–141 (2019).
45. Peters, J. M. *et al.* A comprehensive, CRISPR-based functional analysis of essential genes in bacteria. *Cell* **165**, 1493–1506 (2016).
46. Roucourt, B. & Lavigne, R. The role of interactions between phage and bacterial proteins within the infected cell: a diverse and puzzling interactome. *Environ. Microbiol.* **11**, 2789–2805 (2009).
47. Zhao, X. *et al.* Global transcriptomic analysis of interactions between *Pseudomonas aeruginosa* and bacteriophage PaP3. *Sci. Rep.* **6**, 1–12 (2016).
48. Chaikeeratisak, V. *et al.* Assembly of a nucleus-like structure during viral replication in bacteria. *Science* **355**, 194–197 (2017)

Output จากโครงการวิจัยที่ได้รับทุนจาก สกว.

1. ผลงานตีพิมพ์ในวารสารวิชาการนานาชาติ (ระบุชื่อผู้แต่ง ชื่อเรื่อง ชื่อวารสาร ปี เล่มที่ เลขที่ และหน้า) หรือผลงานตามที่คาดไว้ในสัญญาโครงการ

   ตีพิมพ์เผยแพร่ผลงานวิจัยระดับนานาชาติจำนวน 3 เรื่อง

   1. (งานวิจัยหลัก) ในวารสาร Scientific Reports ซึ่งเป็นวารสารที่อยู่ใน Quartile in Category Q1 และมี Impact Factor 4.122

      Thammatinna, K., Egan, M.K.E., Htoo, H.H., Khanna, K., Sugie, J., Nideffer, J.F., Villa, E., Tassanakajon, A., Pogliano, J., Nonejuie, P., Chaikeeratisak, V. (2020) A novel vibriophage exhibits inhibitory activity against host protein synthesis machinery. Scientific Reports 10 (1), 2347.

   2. (งานวิจัยเสริม) ในวารสาร Cell ซึ่งเป็นวารสารที่อยู่ใน Quartile in Category Q1 และมี Impact Factor 36.216

      Chaikeeratisak, V., Khanna, K., Nguyen, K.T., Sugie, J., Egan, M.E., Erb, M.L., Vavilina, A., Nonejuie, P., Nieweglowska, E., Pogliano, K., et al. (2019). Viral Capsid Trafficking along Treadmilling Tubulin Filaments in Bacteria. Cell 177, 1771-1780.e12.

   3. (งานวิจัยเสริม) ในวารสาร Antimicrobial Agents and Chemotherapy (AAC) ซึ่งเป็นวารสารที่อยู่ใน Quartile in Category Q1 และมี Impact Factor 4.256

      Htoo, H.H., Brumage, L., Chaikeeratisak, V., Tsunemoto, H., Sugie, J., Tribuddharat, C., Pogliano, J., and Nonejuie, P. (2019). Bacterial Cytological Profiling as a Tool To Study Mechanisms of Action of Antibiotics That Are Active against Acinetobacter baumannii. Antimicrobial agents and chemotherapy 63 (4), e02310-18

2. การนำผลงานวิจัยไปใช้ประโยชน์

   - เชิงพาณิชย์ (มีการนำไปผลิต/ขาย/ก่อให้เกิดรายได้ หรือมีการนำไปประยุกต์ใช้โดยภาคธุรกิจ/บุคคลทั่วไป)

     ไม่มี

   - เชิงนโยบาย (มีการกำหนดนโยบายอิงงานวิจัย/เกิดมาตรการใหม่/เปลี่ยนแปลงระเบียบข้อบังคับหรือวิธีทำงาน)

     ไม่มี

   - เชิงสาธารณะ (มีเครือข่ายความร่วมมือ/สร้างกระแสความสนใจในวงกว้าง)

     <u>ความร่วมมือระหว่างการทำวิจัย</u>

     - ได้ร่วมมือกับ Professor Joe Pogliano จาก University of California, San Diego ในการศึกษาการเพิ่มจำนวนของเฟจในเซลล์แบคทีเรียในรูปแบบเซลล์เดียว
     - ได้ร่วมมือกับ Professor Elizabeth Villa จาก University of California, San Diego ในการศึกษาโครงสร้างของแบคเทริโอเฟจด้วยกล้องจุลทรรศน์ความละเอียดสูง

- ได้ร่วมมือกับ อ.ดร.ภูชิต โนนจุ้ย จากสถาบันชีววิทยาศาสตร์โมเลกุล มหาวิทยาลัยมหิดล ศาลายา ในการศึกษารูปร่างของเซลล์แบคทีเรียในสภาวะที่มียาปฏิชีวนะ

<u>เครือข่ายความร่วมมือที่สร้างขึ้นใหม่</u> ภายหลังจากการตีพิมพ์งานวิจัยในวารสาร Scientific Reports ได้มีการสร้างความร่วมมือใหม่ เพื่อศึกษาแบคเทอริโอเฟจในเชิงลึก ดังนี้

- ได้สร้างความร่วมมือกับ Professor Gino Cingolani ณ ศูนย์ Sidney Kimmel Cancer Center มหาวิทยาลัย Thomas Jefferson University เพื่อศึกษาโครงสร้างเฉพาะส่วนของแบคเทริโอเฟจด้วยกล้องจุลทรรศน์ความละเอียดสูง
- ได้สร้างความร่วมมือกับภาคเอกชน บริษัท SCG Chemicals จำกัด

- เชิงวิชาการ (มีการพัฒนาการเรียนการสอน/สร้างนักวิจัยใหม่)
  - นำงานวิจัยมาใช้ในการเรียนการสอนระดับปริญญาบัณฑิต วิชา แบคเทอริโอเฟจ คณะวิทยาศาสตร์ สถาบันเทคโนโลยีพระจอมเกล้าเจ้าคุณทหารลาดกระบัง
  - นำงานวิจัยมาใช้ในการเรียนการสอนระดับบัณฑิตศึกษา วิชา ชีวเคมีของเซลล์ คณะวิทยาศาสตร์ จุฬาลงกรณ์มหาวิทยาลัย
  - พัฒนาและถ่ายทอดความรู้ให้แก่นักศึกษาระดับปริญญาโท นางสาวครองขวัญ ธรรมทินนะ ณ ภาควิชาชีวเคมี คณะวิทยาศาสตร์ จุฬาลงกรณ์มหาวิทยาลัย
  - สร้างผู้ช่วยนักวิจัย Mr. MacKennon E. Egan ใหม่

3. อื่นๆ (เช่น ผลงานตีพิมพ์ในวารสารวิชาการในประเทศ การเสนอผลงานในที่ประชุมวิชาการ หนังสือ การจดสิทธิบัตร)
   - นางสาวครองขวัญ ธรรมทินนะ ได้เสนอผลงานในรูปแบบ Oral presentation ในงานประชุมวิชาการนานาชาติ The 24th Biological Science Graduate Congress 2019 (BSGC2019) ที่จัดขึ้นระหว่างวันที่ 19 – 21 ธันวาคม พ.ศ. 2562

ภาคผนวก
Accepted manuscript ฉบับที่ 1 (งานวิจัยหลัก)

วารสาร Scientific Reports ซึ่งเป็นวารสารที่อยู่ใน Quartile in Category Q1 และมี Impact Factor 4.122

Thammatinna, K., Egan, M.K.E., Htoo, H.H., Khanna, K., Sugie, J., Nideffer, J.F., Villa, E., Tassanakajon, A., Pogliano, J., Nonejuie, P., Chaikeeratisak, V. (2020) A novel vibriophage exhibits inhibitory activity against host protein synthesis machinery. Scientific Reports 10 (1), 2347.

SCIENTIFIC REPORTS
nature research

OPEN

A novel vibriophage exhibits inhibitory activity against host protein synthesis machinery

Khrongkhwan Thammatinna[1,4], MacKennon E. Egan[2,4], Htut Htut Htoo[3], Kanika Khanna[2], Joseph Sugie[2], Jason F. Nideffer[2], Elizabeth Villa[2], Anchalee Tassanakajon[1], Joe Pogliano[2], Poochit Nonejuie[3] & Vorrapon Chaikeeratisak[1*]

Since the emergence of deadly pathogens and multidrug-resistant bacteria at an alarmingly increased rate, bacteriophages have been developed as a controlling bioagent to prevent the spread of pathogenic bacteria. One of these pathogens, disease-causing *Vibrio parahaemolyticus* (VP_{AHPND}) which induces acute hepatopancreatic necrosis, is considered one of the deadliest shrimp pathogens, and has recently become resistant to various classes of antibiotics. Here, we discovered a novel vibriophage that specifically targets the vibrio host, VP_{AHPND}. The vibriophage, designated Seahorse, was classified in the family *Siphoviridae* because of its icosahedral capsid surrounded by head fibers and a non-contractile long tail. Phage Seahorse was able to infect the host in a broad range of pH and temperatures, and it had a relatively short latent period (nearly 30 minutes) in which it produced progeny at 72 particles per cell at the end of its lytic cycle. Upon phage infection, the host nucleoid condensed and became toroidal, similar to the bacterial DNA morphology seen during tetracycline treatment, suggesting that phage Seahorse hijacked host biosynthesis pathways through protein translation. As phage Seahorse genome encodes 48 open reading frames with many hypothetical proteins, this genome could be a potential untapped resource for the discovery of phage-derived therapeutic proteins.

Vibrio is a genus of motile Gram-negative bacteria that possesses a curved-rod cell shape with a single flagellum. Vibrios are abundant and diverse bacteria that are typically found in marine habitats. The genus *Vibrio* consists of 14 recognized clades and at least 86 different species[1]. While some of them are not pathogenic, many can cause serious health effects in both human and aquatic life. Due to the continuously rising ocean temperature, the composition of vibrio in the ocean microbiome has been reported to be higher than usual[2–4]. This vibrio-rich environment might increase the incident of a vibrio outbreak in the near future posing risks to global health[2].

Vibrio parahaemolyticus, which is one of the disease-causing *Vibrio* species, is pathogenic to both humans and marine animals[5]. Consumption of raw seafoods contaminated with the bacteria can cause acute gastroenteritis[5,6]. This opportunistic bacterium is also able to infect through an open wound which can lead to sepsis and, in rare cases, subsequent death in immunocompromised patients[7,8]. Moreover, *V. parahaemolyticus* that has acquired a plasmid encoding the deadly binary toxins $PirA^{vp}/PirB^{vp}$ is even more virulent[9]. The *V. parahaemolyticus* strain harboring the plasmid has been found to cause a newly emerging disease in shrimp, known as acute hepatopancreatic necrosis disease (AHPND)[9]. Moreover, the AHPND-causing plasmid is also found to be transferable among other vibrios, increasing the chance of the disease spreading regionally and globally[10]. Unsurprisingly, the spread of AHPND has been reported in many countries, including China, Vietnam, Malaysia, Thailand, Mexico, the Philippines, and South America[11–13]. Because of its efficient transferability, the gross impact of the infection is also a concern. The infection from AHPND-causing *V. parahaemolyticus* (VP_{AHPND}) in cultured shrimp results in a near 100% mortality rate within a week after the first symptoms appear[14]. Altogether, VP_{AHPND} has easily become a leading cause in tremendous reduction of shrimp farming yield, which could lend itself to global financial detriments in key shrimp aquaculture industries.

[1]Center of Excellence for Molecular Biology and Genomics of Shrimp, Department of Biochemistry, Faculty of Science, Chulalongkorn University, Bangkok, 10330, Thailand. [2]Division of Biological Sciences, University of California, San Diego, La Jolla, California, USA. [3]Institute of Molecular Biosciences, Mahidol University, Salaya, Nakhon Pathom, Thailand. [4]These authors contributed equally: Khrongkhwan Thammatinna and MacKennon E. Egan. *email: vorrapon.c@chula.ac.th

To prevent these detriments, antibiotics are top candidate for control agents because of their ease of use and high accessibility in many countries. However, the heavy misuse of antibiotics undoubtedly contributes to the emergence of multidrug-resistant (MDR) bacteria. This also accelerates the spread of multidrug resistant genes to other bacteria via well documented genetic element transfers within the microbial community[15]. As a result, over the last decade, MDR-vibrios (MDR-V) have been rapidly emerging worldwide and have been found in the United States, China, India and South East Asian countries including Thailand[16,17], with the most recent emergence in Nigeria and Malaysia this past year[18–20]. In particular, MDR-V isolated from cultured animals are now strongly resistant to ampicillin and tetracycline, and moderately resistant to nalidixic acid[16,17]. Specifically, VP_{AHPND} strains have been reported to be resistant to ampicillin, tetracycline, and erythromycin[21,22]. Thus, alternative measures are desperately needed in order to control vibrio outbreaks and prevent further antibiotic resistance development.

Bacteriophage therapy has been under a recent spotlight as an alternative therapeutic method that helps minimize the extensive use of antibiotics, delay the emergence of antibiotic resistance, and combat the existing MDR bacteria[23]. In aquaculture, phage application using various potent lytic phages has been proven successful in preventing vibriosis by *V. harveyi*, *V. alginolyticus*, *V. coralliilyticus*, *V. anguillarum*, *V. cyclitrophicus*, *V. splendidus* as well as *V. parahaemolyticus*[24,25]. During the past few years, many phages, such as VP882, Vp1, Vpms1, A3S, VpKK5, and VVP1, have been isolated from natural resources exhibiting potent antibacterial activity against *V. parahaemolyticus*[26]. However, due to the high specificity of phage, this renders their use too narrow and thus impractical. There have been recent studies to address this, one of which utilized a phage cocktail comprising three lytic phages simultaneously (VP-1, VP-2, and VP-3) that inactivated *V. parahaemolyticus* more efficiently than the individual phages alone[27]. Additionally, a series of reports from Jun JW *et al.* revealed that pVp-1 showed a bactericidal activity toward MDR-*V. parahaemolyticus* and a broad-host range against VP_{AHPND} strains obtained from diverse regions. Moreover, its application on VP_{AHPND}-infected penaeid shrimp in a lab-scale tank revealed high effectiveness in both prophylactic and therapeutic aspects indicating the potential method of phage therapy, so there is evidence that phage therapy can overcome the specificity concern[28–30].

With the ultimate goal of extending the variety of phages targeting VP_{AHPND} and to provide more untapped resources for antimicrobial discovery from phage-encoded products, we report here a novel vibriophage isolated from seawater that was able to kill VP_{AHPND} strain TM. Exploiting fluorescence microscopy techniques based on bacterial cytological profiling (BCP) principle[31], we observed a mechanism of pre-killing (MOK) of this vibriophage in which the phage intercepts host protein translation machinery during the period of infection before host cell lysis. Our study suggests the discovery of a possible therapeutic agent derived from the phage that inhibits protein synthesis of this pathogenic bacterium.

Results

Morphological and biological properties of phage Seahorse. Bacteriophages that target VP_{AHPND} were enriched and isolated from seawater collected from a local shrimp farming area in Thailand. A phage selected for this study actively lysed VP_{AHPND} and produced a 2–3 mm plaque with a 0.5 mm-clear spot at the center surrounding by the halo-turbid area (Fig. 1a). As observed in negative staining by transmission electron microscopy (TEM), the phage belongs to the order *Caudovirales* and the family *Siphoviridae* as it has an icosahedral capsid with a long non-contractile tail with short tail fibers (Fig. 1b). In order to visualize the phage at a higher resolution and at a near-native state, we imaged the phage using cryo-electron tomography (cryo-ET). Our cryo-ET images indicated that the phage had a capsid of ~65 nm in diameter and a tail of ~125 nm in length (Fig. 1c–e; n = 3). The phage capsid seemed to be decorated with other proteins which may likely constitute the head fiber similar to those found in *Bacillus subtilis* phage Phi29 and adenoviruses[32–34]. Our cryo-ET images of the phage also revealed the presence of capsid fibers (the shaft with a knob) of ~10 nm in length at the vertices of the capsid (Purple arrows; Fig. 1c). We also see densities on the capsid facets (~3 nm) which may correspond to minor capsid proteins similar to those found in adenoviruses (Orange arrows; Fig. 1c)[34,35]. These are believed to enhance capsid stability by forming strong protein-protein interactions. Further biochemical and structural studies are needed to characterize and resolve these protein densities unambiguously. Based on the 3-dimensional phage structure under Cryo-ET (Movie S1), we designated this vibriophage as "Seahorse".

To gain more information on the biological properties of phage Seahorse, we tested its host range and conducted a one-step growth curve, a phage tolerance test and measured phage adsorption rate. Out of 26 different bacterial strains tested, phage Seahorse exhibited a narrow host spectrum and specifically infected *V. parahaemolyticus* strain TM that causes AHPND or VP_{AHPND} (Table 1). A phage adsorption assay revealed that more than 95% of the phage were rapidly adsorbed onto the host cell within 15 minutes (Fig. 1f). The one-step growth curve showed that the phage propagated in the cell during the latent period for at least 30 minutes and resulted in a burst size of 72 virions per cell (Figs. 1g, S1, and Table S2). Additionally, the phage was highly tolerant to a wide range of pH and temperatures (Fig. 1h,i). Figure 1h revealed that the phage was able to infect the host with the highest infectivity at pH 6–7 and the infectivity was found to be completely lost at pH 1–3 (Fig. 1h). A thermal stability study showed that the phage was still active at temperatures between 4 °C–50 °C while the phage pre-treated with high temperatures above 60 °C significantly lost their infectivity (Fig. 1i).

Genome features and annotation of phage Seahorse. The complete genome of Seahorse was 45,171 bp long with a GC content of 42.59% encoding 48 putative open reading frames (ORFs) and 3 tRNA genes (Fig. 2 and Table 2). These predicted ORFs were scattered throughout the phage Seahorse genome with different gene arrangements; 35 ORFs in the forward direction and 13 ORFs in the reverse direction (Fig. 2). Out of the total predicted ORFs, 22 ORFs were assigned a putative function according to the significant hits in the indicated databases with E-values less than 10^{-4} while the rest were identified as hypothetical proteins (Table 2). Among them, more than 80% of start codons in the ORFs were ATG followed by TTG (14.58%) and CTG (2.08%). We

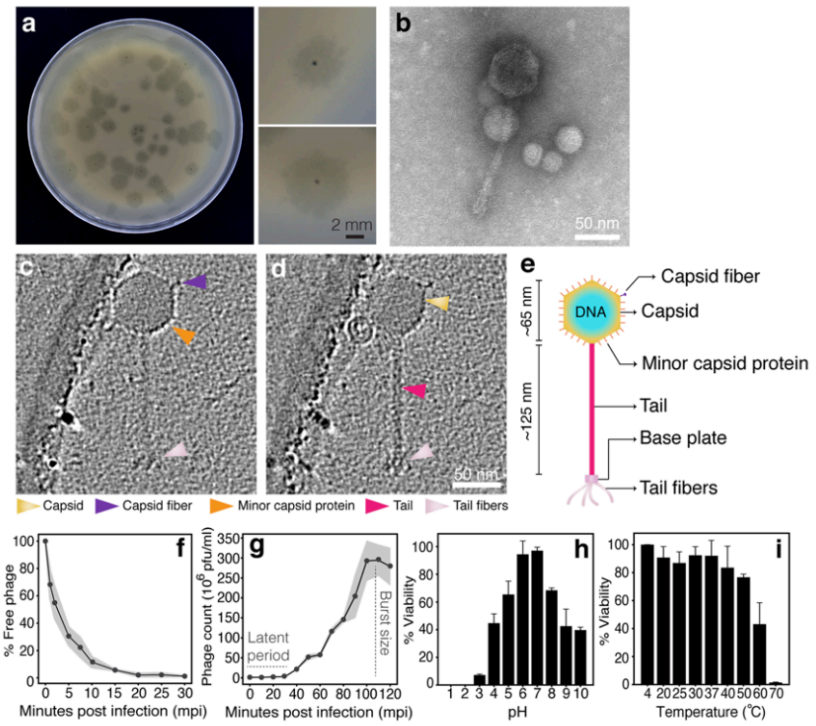

Figure 1. Morphological and biological properties of phage Seahorse. (**a**) Plaque morphology of phage Seahorse. An individual plaque is shown in the right panels. Scale bar equals to 2 mm. Morphology of phage Seahorse as determined by Negative staining and TEM (**b**) and Cryo-ET (**c**,**d**). Different slices (**c**,**d**) through the same Cryo-ET showing the structure of phage Seahorse. Arrows indicate capsid, capsid fiber, minor capsid protein, tail and tail fibers. Scale bar equals to 50 nm. (**e**) Schematic of phage Seahorse as visualized by Cryo-ET with the capsid size and the tail length indicated. (**f**–**i**) Biological studies of phage Seahorse; Adsorption assay (**f**), One-step growth curve (**g**), phage viability in different pH (**h**) and different temperature (**i**). The experiments (**f**–**i**) were conducted in at least 3 independent biological replicates and the data are represented as the mean ± standard deviation.

classified the 22 ORFs into 7 main groups according to function; (1) replication, transcription and translation, (2) DNA metabolism and modification, (3) virion structure and assembly, (4) phage regulation, (5) Nin regions, (6) lysis protein, and (7) other phage-related proteins (Fig. 2). In addition, we did not observe any antimicrobial resistance-coding genes or putative toxins from the phage genome.

As shown in Table 2, we found that the majority of predicted ORFs were virion structural proteins including head morphogenesis protein, tail tape measurement protein, and tail tubular protein as well as ATPase and both small and large subunits of the terminase enzyme, which is involved in DNA encapsidation. A phylogenetic tree of large subunits of terminase of phage Seahorse revealed the close relationship to the temperate vibriophage MAR10 (Fig. S2). Phage Seahorse encoded a set of crucial enzymes that are involved in DNA replication and transcription (e.g. DNA helicase, ribonuclease, and transcriptional regulator), and DNA metabolism and modification (e.g. nucleoside triphosphate pyrophosphohydrolase and adenine methylase). Some ORFs were predicted as a transposase which is involved in phage DNA integration into the host genome while others were categorized as High frequency lysogenization C and Rha family proteins, which also serve a role in the regulation of lysogenic life cycle of phages, all of which suggest that phage Seahorse is indeed a temperate phage[36–38]. This annotation was further validated by a lysogeny experiment and a host cell lysis profile, both confirming that phage Seahorse has an ability to lysogenize the host (Fig. S3). Moreover, we also identify N-acetylmuramoyl-L-alanine amidase, an enzyme that degrades the peptidoglycan layer in bacterial cell walls[39].

Phage Seahorse infection triggers the condensation of host nucleoid. To investigate how phage Seahorse hijacks and kills the host VP_{APHND}, a single cell-leveled assay was used to visualize the bacterial cells upon the phage infection. We first focused on a 30-minute post infection (mpi) window because the one-step

Bacterial species	Strain	Source	Plaque formation
Vibrio parahaemolyticus	AHPND (TM)	Junprung *et al.*[73]	+
	Non-AHPND		–
	ATCC 17802	American type culture collection	–
	DMST 5665	DMST laboratory collection	–
Vibrio harveyi	Isolate 639	Department of Microbiology, Faculty of Science, Chulalongkorn University	–
	Isolate 102		–
	Isolate 2207		–
	Isolate 1526		–
	Isolate gn		–
	Isolate 35		–
Vibrio alginolyticus	DMST 14800	DMST laboratory collection	–
Vibrio cholerae	DMST 2873		–
Vibrio fluvialis	DMST 21248		–
Vibrio vulnificus	DMST 21245		–
Vibrio mimicus	DMST 21244		–
Vibrio natrigens	ATCC 14048	American type culture collection	–
*Vibrio spp.**	VC1060	Isolated from healthy shrimp (This study)	–
	VC1061		–
	VC1062		–
	VC1063		–
Pseudomonas aeruginosa	PA01	Klockgether *et al.*[75]	–
Pseudomonas chlororaphis	200-B	Serwer *et al.*[76]	–
Escherichia coli	ATCC 25922	American type culture collection	–
Burkholderia thailandensis	ATCC 700388		–
Acinetobacter baumannii	ATCC 17978		–
	ATCC 196096		–

Table 1. Host range determination of phage Seahorse. Different bacterial species and strains were used as the host to determine the host spectrum of the phage using a spot test. *Identified by 16 s sequencing. DMST: Department of Medical Sciences, Ministry of Public Health, Thailand.

growth curve suggests that the phage replicates inside the host for only approximately 30 minutes before cell lysis (Fig. 1g). Fluorescence microscopy of Seahorse infected VP_{APHND} revealed a nonuniformly distributed nucleoid at time zero (0 mpi, lower panel; Fig. 3a), identical to the uninfected VP_{APHND} control (0 mpi, upper panel; Fig. 3a). Over intervals of 10 mpi, this distributed nucleoid became more condensed as infection progressed until 30 mpi in which it appeared as a single sphere (30 mpi, lower panel; Fig. 3a). During late infection (after 30 mpi), some unlysed infected cells contained multiple nucleoids exhibiting an archetypal toroid shape (upper panel; Fig. 3b). Similar to a previous study in *Pseudomonas chlororaphis* phage 201Phi2-1, the bacterial host cells lysed at a late time point resulting in the release of phage particles appearing as puncta (blue) surrounding cell debris (red) suggesting the complete lytic cycle of the phage (lower panel; Fig. 3b)[40]. We observed no evidence of condensed DNA ("blob") or toroid formation in the control cells (Figs. 3a and S4; n = 1,782).

To rule out the possibility that the observed nucleoid condensation is caused by host cell membrane leakage, previously seen in pore-forming molecules such as nisin and calcimycin[31], we investigated the membrane integrity of infected cells by testing cell permeability to the DNA staining dye, SYTOX-green. Our result showed that the DNA blob in the infected cells was not stained by SYTOX-green, indicating that the cell membrane remained intact throughout infection, further supporting that phage Seahorse is the cause of the blob DNA formation, not the cell membrane leakage (Fig. 3c).

To confirm that the condensed nucleoid seen in the phage-infected cell is host bacterial DNA, we performed time-lapse fluorescence microscopy over a 30-minute infection period using live cell permeant SYTO 16 DNA dye. At the beginning of infection, the host nucleoid (green) appeared diffuse, similar to the uninfected cell control (Fig. 3d, Movie S2). Over the first 10 minutes, the nucleoid decondensed, seen by the diffusion and reduction of signal within the cell. Beginning at 15 mpi, the DNA nucleoid condensed and eventually appeared in a sphere at the midcell by 30 mpi, identical to the structure seen the infected cell shown in Fig. 3a. This time-lapse observation mirrors the morphological change in the DNA of fixed infected cells conducted over the same time course as shown in Fig. 3a. Altogether, these results suggest that phage Seahorse possibly interferes with the host cellular machineries in which it triggers the morphology change of host DNA.

Inhibition of protein translation resulted in blob and toroid structure formation of the bacterial chromosome. As previously reported by Nonejuie *et al.*[31], fluorescence microscopy-based method, bacterial cytological profiling (BCP), can be used to identify biosynthetic pathways of bacteria that are inhibited based on characteristic cell morphological changes. We therefore applied the principle of BCP to investigate which

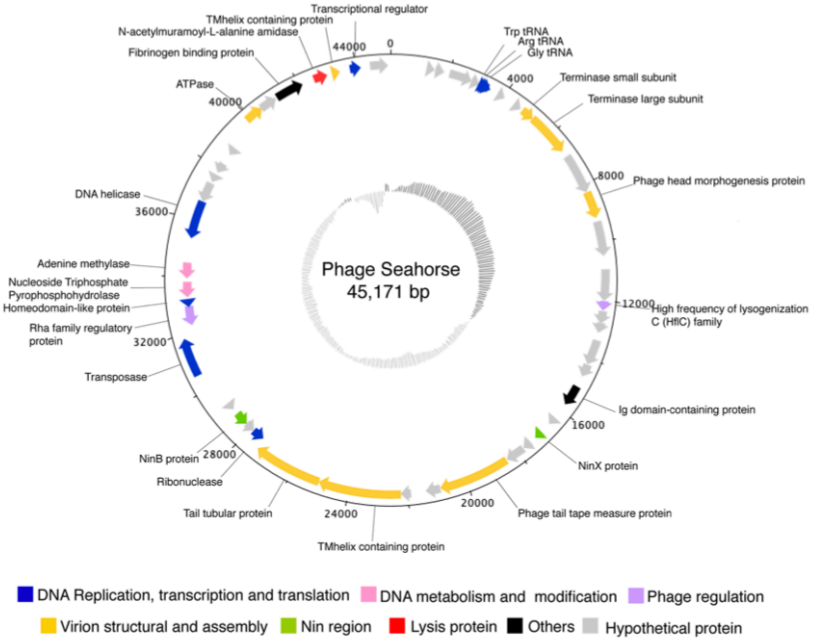

Figure 2. Genome map of phage Seahorse. The genome size is 45,171 base pairs long and the positions in term of base pairs are indicated by the number on the outermost circle. The grey scale on the innermost circle indicates GC content. The open reading frames (ORFs) are annotated and color-coded by their putative function; blue: DNA replication and transcription, and translation, pink: DNA metabolism and modification, purple: phage regulation, yellow: virion structural and assembly, green: Nin region, red: lysis protein, black: others, and grey: hypothetical proteins. The direction of arrows indicates gene arrangement in the genome.

metabolic pathway of VP_{AHPND} is targeted during the phage Seahorse infection by fluorescence microscopy. Since phages are believed to hijack host DNA replication, RNA transcription, and protein translation pathways during the lytic cycle[41], we focused on antibiotics that also inhibit these major pathways. Ciprofloxacin, rifampicin, and tetracycline were used as inhibitors to replication, transcription, and translation respectively. Fluorescence microscopy results of VP_{AHPND} treated with antibiotics showed that each antibiotic treatment led to a unique morphological change in VP_{AHPND}, similar to what previously observed in gram-negative *Escherichia coli* and *Acinetobactor baumannii* treatments[31,42]. Upon ciprofloxacin treatment, inhibition of DNA replication resulted in cell elongation and DNA pooling at the midcell while treatment with rifampicin resulted in DNA decondensation (Fig. 4a). Tetracycline-treated cells exhibited the signature condensed and toroidal-shaped DNA at 30 minutes but more prominently at 60 minutes post treatment with an intact cell membrane (Figs. 4a and S5). This morphology upon tetracycline treatment is notably similar to the condensed DNA morphology of the bacterial cells infected by phage Seahorse (lower panel; Fig. 3a).

The production of "condensed" DNA upon infection instead of perfect "toroidal" shaped DNA urged us to ask if the condensed DNA morphology is truly the result of protein translation inhibition (lower panel, 10–30 mpi; Fig. 3a). The archetypal DNA shape of protein translation inhibition in many studies is a "toroid"[31,42,43], but DNA shape alteration during very early translation inhibition by an antibiotic (less than one hour) has never been reported. Thus, time-course analysis of toroidal DNA formation in VP_{AHPND} during tetracycline treatment was performed. This resulted in a more "condensed" DNA morphology that changed over time with the eventual appearance of the signature "toroid" DNA at 30 minutes post treatment and it became increasingly prominent at 60 minutes (Fig. 4b). Due to the fact that the phage Seahorse had a short latent period and completed its lytic cycle by 30 mpi, it is then reasonable to assume that the toroid DNA morphology was merely undetectable in infected cells because the host cell lysed before toroids were formed. Simply put, if it was able to progress beyond 30 mpi, the nucleoid would have resembled a toroid shape seen in Fig. 4b (45 mpi; Fig. 3b). Altogether, these results suggest that DNA condensation morphology observed in phage Seahorse-infected VP_{AHPND} is likely due to the protein translation inhibition caused by the phage hijacking mechanism.

ORF	Predicted function	Direction	Start	Stop	Size (n)	Sequence similarity	Accession no.	Database	E-value
ORF1	Hypothetical protein	+	1293	1496	204	Hypothetical protein NVP1103O_85 [Vibrio phage 1.103.O._10N.261.52.F2]	AUR87742.1	NCBI	6.00E-27
ORF2	Hypothetical protein	+	1514	1819	306	Hypothetical protein NVP1291O_36 [Vibrio phage 1.291.O._10N.286.55.F6]	AUS01750.1	NCBI	2.00E-46
ORF3	Hypothetical protein	+	2007	2786	780	Hypothetical protein NVP1263A_15 [Vibrio phage 1.263.A._10N.286.51.B1]	AUR99175.1	NCBI	3.00E-12
ORF4	Hypothetical protein	+	2787	3071	285	Hypothetical protein	168987	ACLAME	2.00E-07
ORF5	Hypothetical protein	+	3799	4032	234	Hypothetical protein [Vibrio phage LP.1]	AZU97916.1	NCBI	3.00E-14
ORF6	Hypothetical protein	+	4400	4681	282	Hypothetical protein ValSw33_31 [Vibrio phage ValSw3-3]	AVR75855.1	NCBI	3.00E-42
ORF7	Terminase small subunit	+	4761	5204	443	Phage(gi712916139); PHAGE_ Shewan_3/49_NC_025466: terminase small subunit	PP_00071	PHASTER	7.35E-37
ORF8	Terminase large subunit	+	5194	6678	1484	phage(gi712915541); PHAGE_ Shewan_1/41_NC_025458: terminase large subunit	PP_00070	PHASTER	0
ORF9	Hypothetical protein	+	6898	8274	1377	Hypothetical protein	184967	ACLAME	1.00E-71
ORF10	Phage head morphogenesis protein	+	8261	9190	929	MULTISPECIES: phage head morphogenesis protein [Vibrio]	WP_086959696.1	NCBI	1.00E-149
ORF11	Hypothetical protein	+	9312	10490	1179	Hypothetical protein	184946	ACLAME	2.00E-35
ORF12	Hypothetical protein	+	10936	12006	1071	Hypothetical protein	184931	ACLAME	3.00E-19
ORF13	High frequency of lysogenization C (HflC) family	+	12006	12332	327	High frequency of lysogenization C (HflC) family	YP_009275512.1	NCBI	1.33e-06
ORF14	Hypothetical protein	+	12339	12776	438	Hypothetical protein	184935	ACLAME	4.00E-13
ORF15	Hypothetical protein	+	12736	13089	354	Hypothetical protein	184932	ACLAME	2.00E-05
ORF16	Hypothetical protein	+	13355	14212	858	Hypothetical protein VPKG_00027 [Vibrio phage pYD21-A]	YP_007673989.1	NCBI	3.00E-71
ORF17	Hypothetical protein	+	14209	14652	444	Hypothetical protein ValSw33_31 [Vibrio phage ValSw3-3]	AVR75855.1	NCBI	3.00E-42
ORF18	Ig domain-containing protein	+	15028	15750	722	Uncharacterized conserved protein YjdB, contains Ig-like domain	COG5437	NCBI Conserved Domain Search	2.02E-05
ORF19	Hypothetical protein	+	16335	16598	264	Hypothetical protein NVP1116O_41 [Vibrio phage 1.116.O._10N.222.52.C10]	AUR88658.1	NCBI	2.00E-05
ORF20	NinX protein	+	16974	17261	287	NinX [Salmonella phage S102]	AXC39656.1	NCBI	7.00E-15
ORF21	Hypothetical protein	+	17466	17777	312	Hypothetical protein NVP1239O_45 [Vibrio phage 1.239.O._10N.261.52.F6]	AUR97481.1	NCBI	3.00E-08
ORF22	Hypothetical protein	+	17805	18461	657	Hypothetical protein	184973	ACLAME	3.00E-20
ORF23	Phage tail tape measure protein	+	18471	20900	2430	Lambda family phage tail tape measure protein	181776	ACLAME	5.00E-06
ORF24	Hypothetical protein	+	20900	21397	498	Hypothetical protein [Vibrio phage LP.2]	AZU97857.1	NCBI	3.00E-17
ORF25	Hypothetical protein	+	21903	22250	348	Hypothetical protein NVP1189B_19 [Vibrio phage 1.189.B._10N.286.51.B5]	AUR93845.1	NCBI	8.00E-23
ORF26	TMhelix containing protein	+	22238	25039	2801	TMhelix containing protein [Vibrio phage 1.110.O._10N.261.52.C1]	AUR88148.1	NCBI	3.00E-147
ORF27	Tail tubular protein	+	25039	27384	2345	tail tubular protein [Vibrio phage Athena1]	AUG84865.1	NCBI	2.00E-19
ORF28	Ribonuclease	−	27438	27878	441	Ribonuclease [Vibrio phage VaK]	ARH11752.1	NCBI	6.00E-46
ORF29	Hypothetical protein	−	27875	28228	354	Hypothetical protein NVP1254O_20 [Vibrio phage 1.254.O._10N.286.45.C8]	AUR98603. 1	NCBI	2.00E-20
ORF30	NinB protein	−	28225	28713	488	[Superfamily] cl21658 (PSSMID 328842) NinB protein	PRK09741	NCBI Conserved Domain Search	1.61E-37
ORF31	Hypothetical protein	−	28915	29139	225	Hypothetical protein ValSw33_20 [Vibrio phage ValSw3-3]	AVR75844.1	NCBI	5.00E-38
ORF32	Transposase	+	30555	31868	1313	PHAGE_Burkho_Bcep22_NC_005262: ISL3 family transposase; PP_00032; phage(gi38640338)	PP_00032	PHASTER	8.62E-64
ORF33	Rha family regulatory protein	−	32262	32933	671	Rha family regulatory protein [Vibrio phage 1.119.O._10N.261.51.A9]	AUR89012.1	NCBI	1.00E-94
ORF34	Homeodomain-like protein	−	32903	33175	272	Homeodomain-like protein	AUR86879.1	NCBI	2.00E-28
ORF35	Nucleoside Triphosphate Pyrophosphohydrolase	−	33254	33796	543	[Superfamily] cl16941 (PSSMID 354290) Nucleoside Triphosphate Pyrophosphohydrolase (EC 3.6.1.8) MazG-like domain superfamily	cd11542	NCBI Conserved Domain Search	8.02E-27
ORF36	Adenine methylase	−	33923	34483	560	Adenine methylase [Aeromonas phage 4_D05]	QDJ96121.1	NCBI	3.00E-90

Continued

ORF	Predicted function	Direction	Start	Stop	Size (n)	Sequence similarity	Accession no.	Database	E-value
ORF37	DNA helicase	–	35354	36724	1370	Replicative DNA helicase [Vibrio phage jenny 12G5]	AGN51428.1	NCBI	0
ORF38	Hypothetical protein	–	36721	37425	705	Hypothetical protein ValSw33_44 [Vibrio phage ValSw3-3]	AVR75868.1	NCBI	1.00E-68
ORF39	Hypothetical protein	–	37488	37733	246	Hypothetical protein S349_62 [Shewanella sp. phage 3/49]	YP_009103948.1	NCBI	1.00E-10
ORF40	Hypothetical protein	–	37871	38242	372	Hypothetical protein VPR_009 [Vibrio phage Vp_R1]	AUG88373.1	NCBI	5.00E-54
ORF41	Hypothetical protein	–	38629	38919	291	Hypothetical protein NVP1113A_38 [Vibrio phage 1.113.A._10N.286.51.E7]	AUR88439.1	NCBI	5.00E-31
ORF42	ATPase	+	39897	40544	647	ATPase [Aeromonas phage 2_D05]	QDB73849.1	NCBI	2.00E-99
ORF43	Hypothetical protein	+	40525	41121	597	Hypothetical protein	166167	ACLAME	2.00E-26
ORF44	Fibrinogen binding protein	+	41169	42131	962	Fibrinogen binding protein [Vibrio phage 1.013.O._10N.286.54.F9]	AUR81803.1	NCBI	3.00E-137
ORF45	N-acetylmuramoyl-L-alanine amidase	+	42558	43019	461	N-acetylmuramoyl-L-alanine amidase [Vibrio phage 1.232.O._10N.261.51.E11]	AUR96787.1	NCBI	3.00E-51
ORF46	TMhelix containing protein	+	43209	43460	251	TMhelix containing protein [Vibrio phage 1.134.O._10N.222.52.B8]	AUR89889.1	NCBI	3.00E-23
ORF47	Transcriptional regulator	+	43798	44172	375	Transcriptional regulator	184491	ACLAME	5.00E-06
ORF48	Hypothetical protein	+	44476	45090	615	Hypothetical protein ValSw33_24 [Vibrio phage ValSw3-3]	AVR75848.1	NCBI	2.00E-28

Table 2. List of annotated proteins from ORFs in the genome of phage Seahorse. ORFs with the predicted functions were determined by their significant hit (E-value $< 10^{-4}$) against genome databases.

Discussion

A new strain of *V. parahaemolyticus*, called VP_{APHND}, emerged in 2009 as a devastating pathogen to shrimp, causing acute hepatopancreatic necrosis disease (AHPND) or early mortality syndrome (EMS). The infection resulted in mass production losses in southern China and within several years, the incidence of VP_{APHND} infection had expanded to other neighboring countries such as Vietnam, Malaysia and Thailand[11]. The disease contributes to 100% mortality of shrimp within one week and the infected animals present an atrophied and discolored hepatopancreas due to the *Photorhabdus* insect-related (Pir) binary toxins ($PirA^{vp}$/$PirB^{vp}$), which are encoded on the virulent plasmid of the pathogen. The toxins degenerate the tubule epithelial cells of the hepatopancreas leaving the diseased animals susceptible to additional bacterial infections[44,45].

Due to the emergence of VP_{AHPND} and its multidrug resistant isolates, effective tools to control and combat these pathogens are urgently needed. Most recently, Angulo *et al.* revealed a number of studies and research reports on using phages as a biocontrol for the wide spread of AHPND[26]. Until now, even though many phages have been reported to target *V. parahaemolyticus*, only phage pVp-1 has been found to effectively kill VP_{AHPND}. Phage pVp-1 is highly potent and lyses more than 90% out of the VP_{AHPND} strains that were isolated from Vietnam, Mexico, Costa Rica, Honduras, and Central America Countries[29]. However, the bacterial strain isolated from Thailand is not targeted by the pVp-1 phage. In this study, we successfully isolated a novel phage (named "Seahorse") that specifically infects the VP_{AHPND} strain isolated in Thailand. This study also elucidates that the phage is able to hijack protein translation machinery of the host bacteria. In comparison to other phages that infect vibrios (Table S2)[46–52], phage Seahorse has relatively big burst size with a shorter latency period than phages VP-1, VP-2, VP-3, VpKK5, and VhKM4 that replicate in *V. parahaemolyticus*[27,29,53–56]. It is also tolerant to the wide range of pHs and temperatures compared to other vibriophages suggesting unique survivability in harsh natural environments. These infectious characteristics not only add phage Seahorse to the library of phage targeting VP_{AHPND} but also make it a potential candidate for a biocontrol agent.

Bacteriophage requires a bacterial host cell to replicate, manipulating the native biosynthesis machinery of the host to assemble its own progeny. During its reproduction process, various phage-encoding proteins are produced to redirect or inhibit the host metabolism at the molecular level to benefit its fitness. These phage-derived proteins not only target the major metabolic pathways but are also capable of lysing the host cell membrane. Due to nature of these effects, these proteins can be considered antimicrobial agents similar to that of antibiotics with possible therapeutic applications[39]. Phage Seahorse was classified in the family *Siphoviridae* due to characteristics of the flexible, noncontractile tail with a non-enveloped icosahedral capsid. In addition, at high resolution near a native-state by Cryo-ET, unique spikes and fibers (a shaft with a sphere at the tip) on the phage capsid were observed. This is not the first time that this structure has been reported[32–35]. These are most likely structurally diverse glycoproteins encoded by the phage and thought to promote tethering of the viral capsid to receptors present on the host cell surface. For instance, in the case of human adenoviruses, the fibers have a long shaft with a knob at the distal end of the capsid whereas, in phage Phi29 and some bovine adenoviruses, they consist of only a protruding stem without a terminal sphere[32,34,35,57,58]. Moreover, phage Sf6 that infects *Shigella flexneri* has an identical shaft-knob structure at the tail terminus called the "tail needle knob"[59]. Due to the narrow host spectrum of phage Seahorse, the capsid spikes and fibers located on the surface of the phage capsid serve a potential role in host specificity and recognition.

Unfortunately, in a therapeutic context, phage Seahorse is not appropriate for application due to the ability to enter lysogenic cycle which renders the phage unsafe for treatment. Phage Seahorse appeared phylogenetically

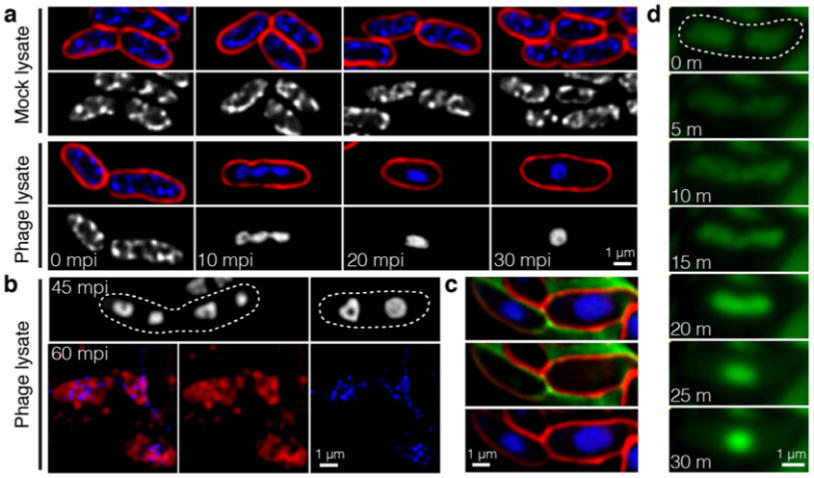

Figure 3. Single cell-leveled assay revealing the formation of blob and toroid of host DNA inside the phage-infected cells. Bacterial cells were grown in liquid culture to log phase and infected by phage Seahorse at MOI 5. At desired time points, the bacterial cells were harvested and fixed. For live cell imaging, the cells were inoculated on an agar pad after the phage infection. Prior to fluorescence microscopy, cell membrane (red) and nucleoid (blue/grey) were stained by FM4–64 and DAPI, respectively. (**a**) Fluorescence images of fixed bacterial cells in the presence of mock lysate (upper panel) and phage lysate (lower panel) at various time points. (**b**) Still images of phage-infected cells during late infection; 45 mpi (upper panel) and 60 mpi (lower panel). (**c**) Live cell images of phage-infected cells. SYTOX-green as impermeable DNA staining dye was used as an indicator of live cells. (**d**) Time-lapse imaging of phage-infected cells over the course of 30 minutes. Nucleoid (green) as stained by SYTO 16 condensed and became blob shaped as early as 25 minutes. Dashed lines indicate cell borders. Scale bars equal to 1 micron.

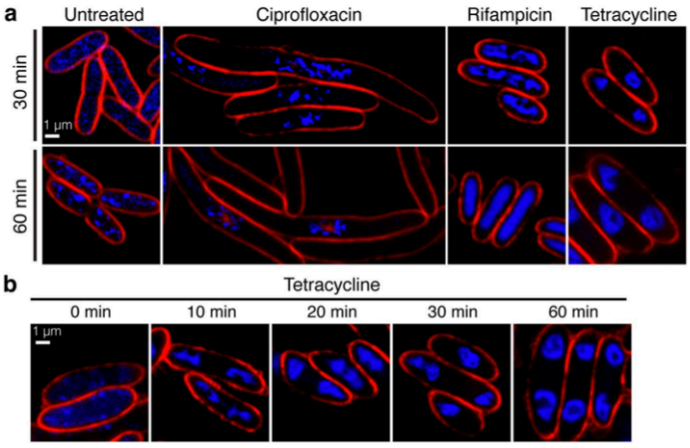

Figure 4. Fluorescence microscopy showed unique morphology of bacterial cells during the antibiotic treatment targeting different cellular pathways. Bacterial cells during the log phase were treated with antibiotics (ciprofloxacin, rifampicin, and tetracycline) at 5X MIC for indicated period of time. At desired time points, the cells were fixed and stained with FM4–64 (red) and DAPI (blue) prior to fluorescence microscopy. (**a**) Fluorescence images of fixed bacterial cells after the treatment with different antibiotics at 30 minutes (upper panel) and 60 minutes (lower panel). (**b**) Time-course still images of tetracycline-treated bacterial cells. Scale bars equal to 1 micron.

related to the temperate phage MAR10 that belongs to the genus *Ssp2virus* and targets *V. parahaemolyticus* (Fig. S2)[60,61]. This reassures our conclusion that phage Seahorse is temperate and also suggests the possible viral family it belongs to. Moreover, due to the lack of bioinformatics in phage related databases, the majority of the ORFs annotated in the phage Seahorse genome were predicted as unknown. As they might produce unwanted products or other unknown virulence factors, the therapeutic application is not warranted unless the fundamental knowledge in phage biology is better established or the phage is engineered to strictly enter only the lytic cycle[62].

However, despite the therapeutic shortcomings of phage Seahorse itself, phage genomes generally are considered an untapped resource for antimicrobials due to the metabolic hijacking ability and lytic capacity of the proteins they encode[63,64]. For example, from our genome analysis, albeit its relatively small genome, we were able to identify a lysis-related enzyme, N-acetylmuramoyl-L-alanine amidase, from ORF45. This lysis enzyme is involved in the cleavage of a very common bond present in most bacterial cell membranes, thus serving a crucial role in cell lysis[39]. In fact, it has been reported that the application of recombinant phage lysis enzymes from vibriophages can target a wider spectrum of bacterial hosts as compared to the parental phages[65,66]. Therefore, there is a strong possibility of finding other antibacterial protein candidate from this small phage in the future. Determining whether or not other hypothetical proteins found in the phage Seahorse genome and other newly discovered phage exhibit antibacterial activity needs further investigation.

With the lysis-related enzyme in mind, we set out to investigate whether the phage Seahorse genome encoded other proteins that targeted major host metabolic pathways during its lytic cycle. Bacterial morphological changes have been used as indicators for various physiological states of bacteria elicited by genetic alteration or stress response[31,67,68]. BCP exploits these cell morphological change patterns under different stresses to identify the specific mechanism being targeted by an antibiotic that causes bacterial growth inhibition. This study, for the first time, applied the principle of BCP technique to identify the underlying effected pathway and found that phage Seahorse likely inhibits protein translation of VP_{AHPND} at the early stage of infection. This finding is concomitant with other reported hijacking mechanisms that use phage-host protein-protein interactions to inhibit host machineries (i.e. replication, transcription and translation) with the effect of disarming host defenses and producing its own proteins for reproduction[69]. Thus, the hijacking model of host protein machinery in favor of phage protein production right after infection is plausible. For example, *Pseudomonas aeruginosa* phage PaP3 strongly suppresses host protein synthesis through the reduction of ribosome to preserve energy[70]. Our finding does not directly indicate that native host replication and transcription are not also inhibited during the infection. To date, BCP has never been applied to study replication, transcription and translation inhibition simultaneously or chronologically. Thus, it is possible that host replication and transcription machineries were inhibited but only the profound protein translation inhibition phenotype was detected. Whether or not a temporal hijacking mechanism is presented during different stages of infection requires further investigation.

Our study revealed the formation of host toroidal nucleoids that are likely the result of encoded phage proteins that hijack host translation machinery before cell lysis, as we called it: "Mechanism of pre-killing (MOK)". This study suggests that the phage Seahorse genome contained at least one product that was involved in the inhibition towards a protein biosynthesis pathway. Further investigation into which of the phage-derived proteins target important pathways of the bacterial host will be needed in order to identify these antimicrobial proteins for development as therapeutics against pathogens. Localization profiling of phage proteins inside the host, as we previously reported[71,72], could also be utilized to study Seahorse-infected cells to gain a better understanding of how individual phage-encoded proteins temporally and spatially function within the host. These investigations could help overcome Seahorse's therapeutic shortcomings while identifying novel antimicrobial agents at the molecular level.

Material and Methods

Phage isolation, purification, and preparation. Overnight cultures of VP_{AHPND} were prepared by inoculating the bacteria, previously grown on Tryptic Soy Agar supplemented with 1.5% Sodium chloride (TSA-1.5%NaCl), into 5 ml of Tryptic Soy Broth supplemented with 1.5% Sodium chloride (TSB-1.5%NaCl) and allowed to incubate at 30 °C, 200 rpm for at least 16 hours. One milliliter of seawater was added to 25 ml of TSB-1.5%NaCl, 250 µl of 100 mM $CaCl_2$, and 2.5 ml of VP_{AHPND} overnight culture. Phage was enriched by growing at 30 °C, 200 rpm for 48 hours. Phage was next harvested by centrifugation at 9,000 rpm for 10 minutes followed by collecting and filtering the supernatant using a 0.45 µm filter. Next, phage purification was performed using double-layer agar method. Briefly, 10-fold serial dilutions of phage were prepared using SM buffer. Ten microliters of each diluent were added to 100µl of overnight culture of VP_{AHPND}, mixed and allowed to stand for 10 minutes. To this, 5 ml of melted 0.35% top agar of TSA-1.5%NaCl was added, mixed and poured onto a TSA-1.5%NaCl plate. The plates were incubated overnight at 30 °C. Putative translucent plaques were identified and picked and resuspended in 100 µl of SM buffer. This purification step was repeated 3 times. A high-titer phage lysate was prepared described by Chaikeeratisak *et al.*[72]. Briefly, 5 ml SM buffer was added to a near-confluent plate and incubated at 30 °C for at least 5 hours. The solution was aspirated into a tube and centrifuge at 9,000 rpm for 5 minutes. Finally, the supernatant was filtered using a 0.45 µm filter and stored at 4 °C.

This work has been reviewed and approved by Chulalongkorn University-Institutional Biosafety Committee (CU-IBC) in accordance with the levels of risk in pathogens and animal toxins listed in the Risk Group of Pathogen and Animal Toxin (2017) published by Department of Medical Sciences (Ministry of Public Health), the Pathogen and Animal Toxin Act (2015) and Biosafety Guidelines for Modern Biotechnology BIOTEC (2016) with approval number: SC CU-IBC-006/2018.

Transmission electron microscopy and cryo-electron tomography. 3 µl of phage titer was deposited on QUANTIFOIL 200 mesh holey carbon R 2/1 gold grids, glow-discharged using PELCO easiGlow (Ted Pella).

The grids were blotted using Whatman No. one filter paper and plunge-frozen into a liquid ethane/propane mixture cooled by liquid nitrogen using a custom-built device (Max Planck Institute for Biochemistry, Munich). Tilt series were collected on grids clipped onto autogrids (Thermo Scientific) in a 300 keV Titan Krios (Thermo Scientific) fitted with a K2 Summit 4k x 4k pixel direct electron detector and a GIF Quantum post-column energy filter (Gatan) using a nominal magnification of 42 kx or a pixel size of 3.4 Å and −5 μm defocus. Tilt series were acquired using SerialEM in low dose mode, typically from −40o to +40o every 2–3 degrees with a total dose of 50–70 e/Å2. The tilt series were aligned and dose-weighted according to the cumulative dose using MotionCor2 and reconstructed in IMOD software using weighted back-projection.

Conventional phage study. To evaluate phage adsorption, VP_{AHPND} culture (OD_{600} ~ 0.4) was infected with phage particles at MOI 0.01 (The OD_{600} of 1 = 1×10^9 CFU/ml[73]) and incubated at 30 °C. At each time point of 0, 1, 2, 5, 7.5, 10, 15, 20, 25, and 30 minutes, 100 μl of the samples were collected and diluted 10-fold in SM buffer. After centrifugation at 15,000 × g for 2 minutes at 4 °C, the supernatant was harvested and the number of free phages was determined by double-layer agar method. For the one-step growth curve analysis, VP_{AHPND} was infected at MOI 0.01 at 30 °C for 15 minutes, then the cell suspension was centrifuged at 12,000 × g for 5 minutes. The pellet was resuspended in 10 ml of TSB-1.5% NaCl. The mixture was then incubated with vigorous shaking at 200 rpm, 30 °C for 2 hours. Throughout the period of shaking, the samples of the untreated group and the chloroform-treated group were taken every 10 minutes to evaluate total virions by double-layer agar method.

For pH stability, 100 μl of phage lysate was mixed with 900 μl of SM buffer in a pH range 2 to 10 and incubated at 30 °C for 1 hour. For temperature stability, 50 μl of phage lysate was incubated for 1 hour at different temperatures; 4, 20, 25, 30, 37, 40, 50, 60, and 70 °C. For both tests, phage infectivity was determined by performing a spot test. These experiments were performed in triplicate.

To determine host spectrum of the phage, a spot test was performed to test the infectivity of the isolated phage against different 26 bacterial strains that we obtained and were kindly offered from different sources as indicated in Table 1. Briefly, overnight cultures were prepared as described above. 500 μl of each culture was mixed with 5 ml of 0.35% molten top agar (TSA-1.5% NaCl) and immediately poured on an agar plate (TSA-1.5% NaCl). After the cell lawn was solidified, 5 μl of each diluent of 10-fold serially diluted phage was spotted on the surface of the top agar. The plates were allowed to dry and next incubated overnight at 30 °C. The clearing zones were then evaluated for the infection ability of the phage toward the bacterial host.

Phylogenetic tree construction. DNA sequences of the terminase large subunit of various phages were obtained through GenBank. These sequences included accession number and phage names as follows: Vibriophage KVP40: NC_005083, Vibriophage CP-T1: NC_019457.1, Vibriophage pVp-1: NC_019529.1, Vibriophage vB_VpaS_MAR10: NC_019713.1, Vibriophage VH7D: NC_023568.1, *Enterobacteria* phage 9 g: NC_024146.1, *Salmonella* phage Stitch: NC_027297.1, Vibriophage phi 3: NC_028895.1, *Enterobacteria* phage JenK1: NC_029021.1, *Vibrio vulnificus* phage SSP002: NC_041910, *Enterobacteria* phage EPS7: NC_010583.1 and phage Seahorse. The sequences were aligned using ClustalW and the phylogenetic tree was constructed using Molecular Evolutionary Genetics Analysis (MEGA) version 10.0 as described by Kumar *et al.*[74]. Using the Maximum Likelihood method, a bootstrap consensus phylogenetic tree from 100 bootstrap replications for tree construction was selected. The selected numbers of bootstrap were shown on the selected branches.

Lysogeny experiment. To isolate phage-resistant strains, bacterial colonies that appeared in a double layer-agar plate at high titer of phage were picked and further isolated. The isolated strains and original VP_{AHPND} were tested for phage resistance by cross streaking each isolate with a drop of high titer phage lysate atop the bacterial stripes. The plate was incubated overnight at 30 °C and the result was recorded. To test whether the phage-resistant isolates were lysogen, a bacterial cell lawn of VP_{AHPND} strain was prepared as described above. Single colony of each phage-resistant isolate was picked by a sterile toothpick and stabbed into the top agar. The plate was then incubated at 30 °C overnight and the presence of a clear zone surrounding the stab isolate was recorded the day after.

Bacterial cell lysis profile assay. VP_{AHPND} culture at mid-log phase (OD_{600} ~ 0.4) was inoculated with phage lysate at MOI 0 as a control and MOI 0.01 and MOI 5 as experimental groups. The cultures were then incubated shaking at 200 RPM at 30 °C. OD_{600} of all cultures were monitored every 30 minutes until 10 hours of incubation. The experiment was carried out in triplicate.

Phage genome DNA extraction. The phage lysate was first dialyzed in sterile distilled water. Next, phage was precipitated by adding 2.5 ml of phage precipitant solution (30% w/v PEG-8,000, 3.3 M NaCl and sterile distilled water) to 10 ml of phage lysate (~10^9 pfu/ml) and stored overnight at 4 °C. The solution was then centrifuged at 10,000 rpm for 30 minutes followed by resuspending the pellet in 500 μl of 1xDNase I buffer. To degrade bacterial genomic DNA and RNA, 5U DNaseI and 25 μg RNaseA were added and incubated at 37 °C for 2 hours. Next, 25 mM EDTA was added to inhibit nuclease activity, followed by 0.5% SDS and 25 μg proteinase K, and incubated at 60 °C for 2 hours. Phenol-chloroform extraction was then performed to extract phage genomic DNA.

Phage genome sequencing and analysis. Phage genomic DNA was sequenced by Illumina MiSeq platform. All raw reads were qualified and the low qualities were eliminated. The adaptors in the filtered reads were then trimmed and assembled into contigs. To remove potential host DNA contamination, reads were mapped to the host strain sequence of *V. parahaemolyticus* strain ATCC17802 (GenBank accessions CP014046, CP014047) using the Geneious mapper in Geneious Prime 2019 (https://www.geneious.com). The unmapped reads were used

for assembly in Geneious Prime 2019 with the Geneious assembler using high sensitivity and default parameters. A list of ORFs was generated from this contig using the ORF finder in Geneious; filtering out any ORFs less than 200 base pairs. The protein sequences of each ORFs were predicted by EMBOSS Transeq and they were annotated manually by BLASTp and PSI-BLAST (cut-off e-value $< 10^{-4}$) against various databases: NCBI's non-redundant (nr) protein sequences, InterPro 75.0, NCBI conserved domain and ACLAME. In addition, to confirm the predicted function, RAST sever, Prodigal and PHASTER were used as well. To determined antimicrobial resistance coding genes and putative toxins, RESFINDER and VirulenceFinder were used, respectively. Aragon and tRNAScanSE were used to identify tRNAs. The map of genome was drawn by Artemis and DNA plotter.

Single cell-infection assay. VP_{AHPND} culture (OD_{600} ~ 0.4) was infected with phage at MOI 5 and the infected cells were incubated at 30 °C. At each time point; 0, 10, 20 and 30 minutes, the samples were harvested by centrifugation at 9,000 rpm for 2 minutes and the supernatant discarded. As described by Chaikeeratisak *et al.*[72], phage-infected cells were fixed at a final concentration of 4% paraformaldehyde and incubated at room temperature for 15 minutes. The fixed cells were centrifuged and the pellets were washed with 500 µl of 1x PBS three times. The cells were resuspended in 1x PBS before loading 3 µl onto an agarose pad (1.2% agarose in 20% TSB-1.5% NaCl) that contained fluorescent dyes (2 µg/ml FM 4–64 and 2 µg/ml DAPI). The samples were visualized under DeltaVision Ultra High-Resolution Microscope. For live cells, the cells were harvested at desired time points, and inoculated on an agarose pad as described above. The nucleoid was stained with either 0.5 µM SYTOX-green or 0.5 µM SYTO 16, prior to fluorescence microscopy.

Minimal inhibitory concentration. Minimal inhibitory concentrations (MIC) were determined for the following antibiotics: Ciprofloxacin, Rifampicin, and Tetracycline, which were all used in the fluorescence microscopy experiment shown in Table S1. The antibiotics were respectively serially diluted in a 96 well plate using a microdilution method[42]. Overnight cultures of VP_{AHPND} were diluted 100-fold in TSB-1.5% NaCl and allowed to grow on a roller at 30 °C until exponential growth (OD_{600} of 0.2) was observed. The culture was further diluted 100-fold in TSB-1.5% NaCl into wells of the same 96-well plate that contained different concentrations of the respective antibiotic. The culture was further incubated at 30 °C for 24 hours. MICs for each antibiotic were determined as the lowest concentration dilution of that antibiotic capable of inhibiting growth of the bacteria.

Fluorescence microscopy. Overnight cultures of VP_{AHPND} were diluted 100-fold in TSB-1.5% NaCl and incubated at 30 °C on a roller until exponential phase of growth was obtained. Antibiotics were added to the culture at concentrations of 5 times the MIC. For live cell imaging, cultures were incubated at 30 °C on a roller for 60 minutes followed by staining with fluorescent dyes; FM 4–64 (2 µg/ml), DAPI (2 µg/ml) and SYTOX-green (0.5 µM). Cultures were then harvested by centrifugation at 6,000 g for 30 seconds and resuspended in 30 µl of supernatant. 3 µl of sample was loaded onto agarose pad (1.2% agarose containing 20% TSB-1.5% NaCl) on concave glass slides and fluorescence microscopy was performed, following consistent imaging parameters throughout all of the experiments. For fixed cell imaging, cultures were incubated on a roller at 30 °C for 30 and 60 minutes for treatment with ciprofloxacin and rifampicin, while 10, 20, 30 and 60 minutes for treatment with tetracycline. After the completion of each treatment, cultures were fixed as described above. Cultures were then harvested by centrifugation at 9,000 rpm for 2 minutes followed by washing the pellet with 1x PBS for 3 times. After centrifugation, the pellet was resuspended in 30 µl of 1x PBS and added to an agarose pad as described above. Fluorescence microscopy was performed using consistent imaging parameters for all experiments.

Data availability

All data generated or analyzed in this study are included in this article and its supplementary information files. Nucleotide sequence of the phage Seahorse genome was deposited in GenBank database with the accession number MN512538.

Received: 2 October 2019; Accepted: 27 January 2020;
Published online: 11 February 2020

References

1. Sawabe, T. *et al.* Updating the Vibrio clades defined by multilocus sequence phylogeny: proposal of eight new clades, and the description of *Vibrio tritonius* sp. nov. *Front. Microbiol.* **4**, 414 (2013).
2. Vezzulli, L. *et al.* Climate influence on *Vibrio* and associated human diseases during the past half-century in the coastal North Atlantic. *Proc. Natl. Acad. Sci.* **113**, E5062 (2016).
3. Froelich, B., Gonzalez, R., Blackwood, D., Lauer, K. & Noble, R. Decadal monitoring reveals an increase in *Vibrio* spp. concentrations in the Neuse River Estuary, North Carolina, USA. *Plos One* **14**, e0215254 (2019).
4. Siboni, N., Balaraju, V., Carney, R., Labbate, M. & Seymour, J. R. Spatiotemporal Dynamics of *Vibrio* spp. within the Sydney Harbour Estuary. *Front. Microbiol.* **7**, 460 (2016).
5. Su, Y. C. & Liu, C. *Vibrio parahaemolyticus*: A concern of seafood safety. *Food Microbiol.* **24**, 549–558 (2007).
6. Iwamoto, M., Ayers, T., Mahon, B. E. & Swerdlow, D. L. Epidemiology of seafood-associated infections in the United States. *Clin. Microbiol. Rev.* **23**, 399–411 (2010).
7. Velazquez-Roman, J., León-Sicairos, N., Hernandez-Diaz, L. & Canizalez-Roman, A. Pandemic *Vibrio parahaemolyticus* O3:K6 on the American continent. *Front. Cell. Infect. Microbiol.* **3**, 110 (2014).
8. Ghenem, L., Elhadi, N., Alzahrani, F. & Nishibuchi, M. *Vibrio Parahaemolyticus*: A Review on Distribution, Pathogenesis, Virulence Determinants and Epidemiology. *Saudi J. Med. Med. Sci.* **5**, 93–103 (2017).
9. Lee, C. T. *et al.* The opportunistic marine pathogen *Vibrio parahaemolyticus* becomes virulent by acquiring a plasmid that expresses a deadly toxin. *Proc. Natl. Acad. Sci.* **112**, 10798 (2015).
10. Restrepo, L. *et al.* PirVP genes causing AHPND identified in a new *Vibrio* species (*Vibrio punensis*) within the commensal Orientalis clade. *Sci. Rep.* **8**, 13080 (2018).
11. Thitamadee, S. *et al.* Review of current disease threats for cultivated penaeid shrimp in Asia. *Aquaculture* **452**, 69–87 (2016).

12. Soto-Rodriguez, S. A., Gomez-Gil, B., Lozano-Olvera, R., Betancourt-Lozano, M. & Morales-Covarrubias, M. S. Field and Experimental Evidence of *Vibrio parahaemolyticus* as the Causative Agent of Acute Hepatopancreatic Necrosis Disease of Cultured Shrimp *Litopenaeus vannamei* in Northwestern Mexico. *Appl. Environ. Microbiol.* **81**, 1689 (2015).
13. Restrepo, L., Bayot, B., Betancourt, I. & Pinzón, A. Draft genome sequence of pathogenic bacteria *Vibrio parahaemolyticus* strain Ba94C2, associated with acute hepatopancreatic necrosis disease isolate from South America. *Genomics. Data* **9**, 143–144 (2016).
14. Lai, H. C. *et al.* Pathogenesis of acute hepatopancreatic necrosis disease (AHPND) in shrimp. *Fish Shellfish Immunol.* **47**, 1006–1014 (2015).
15. Davies, J. & Davies, D. Origins and evolution of antibiotic resistance. *Microbiol. Mol. Biol. Rev.* **74**, 417–433 (2010).
16. Elmahdi, S., DaSilva, L. V. & Parveen, S. Antibiotic resistance of *Vibrio parahaemolyticus* and *Vibrio vulnificus* in various countries: A review. *Food Microbiol.* **57**, 128–134 (2016).
17. Yano, Y. *et al.* Prevalence and antimicrobial susceptibility of *Vibrio* species related to food safety isolated from shrimp cultured at inland ponds in Thailand. *Food Control* **38**, 30–36 (2014).
18. Emmanuel, E. O. & Etinosa, O. I. Multi-drug resistant *Vibrio* species isolated from abattoir effluents in Nigeria. *J. Infect. Dev. Ctries.* **11**, (2017).
19. Tan, C. W. *et al.* Prevalence and Antimicrobial Susceptibility of *Vibrio parahaemolyticus* Isolated from Short Mackerels (*Rastrelliger brachysoma*) in Malaysia. *Front. Microbiol.* **8**, 1087–1087 (2017).
20. Odeyemi, O. A. & Ahmad, A. Population dynamics, antibiotics resistance and biofilm formation of *Aeromonas* and *Vibrio* species isolated from aquatic sources in Northern Malaysia. *Microb. Pathog.* **103**, 178–185 (2017).
21. Kongrueng, J. *et al.* Characterization of *Vibrio parahaemolyticus* causing acute hepatopancreatic necrosis disease in southern Thailand. *J. Fish Dis.* **38**, 957–966 (2015).
22. Han, J. E., Mohney, L. L., Tang, K. F. J., Pantoja, C. R. & Lightner, D. V. Plasmid mediated tetracycline resistance of *Vibrio parahaemolyticus* associated with acute hepatopancreatic necrosis disease (AHPND) in shrimps. *Aquac. Rep.* **2**, 17–21 (2015).
23. Sulakvelidze, A., Alavidze, Z. & Morris, J. G. Bacteriophage Therapy. *Antimicrob. Agents Chemother.* **45**, 649 (2001).
24. Doss, J., Culbertson, K., Hahn, D., Camacho, J. & Barekzi, N. A Review of Phage Therapy against Bacterial Pathogens of Aquatic and Terrestrial Organisms. *Viruses* **9**, 50 (2017).
25. Kalatzis, G. P., Castillo, D., Katharios, P. & Middelboe, M. Bacteriophage Interactions with Marine Pathogenic *Vibrios*: Implications for Phage Therapy. *Antibiotics* **7**, (2018).
26. Angulo, C., Loera-Muro, A., Trujillo, E. & Luna-González, A. Control of AHPND by phages: a promising biotechnological approach. *Rev. Aquac.* 1–16 (2018).
27. Mateus, L. *et al.* Efficiency of phage cocktails in the inactivation of *Vibrio* in aquaculture. *Aquaculture* **424–425**, 167–173 (2014).
28. Jun, J. W. *et al.* Bacteriophage Therapy of a *Vibrio parahaemolyticus* Infection Caused by a Multiple-Antibiotic–Resistant O3:K6 Pandemic Clinical Strain. *J. Infect. Dis.* **210**, 72–78 (2014).
29. Jun, J. W. *et al.* Potential application of bacteriophage pVp-1: Agent combating *Vibrio parahaemolyticus* strains associated with acute hepatopancreatic necrosis disease (AHPND) in shrimp. *Aquaculture* **457**, 100–103 (2016).
30. Jun, J. W. *et al.* Phage Application for the Protection from Acute Hepatopancreatic Necrosis Disease (AHPND) in *Penaeus vannamei*. *Indian J. Microbiol.* **58**, 114–117 (2018).
31. Nonejuie, P., Burkart, M., Pogliano, K. & Pogliano, J. Bacterial cytological profiling rapidly identifies the cellular pathways targeted by antibacterial molecules. *Proc. Natl. Acad. Sci.* **110**, 16169 (2013).
32. Xiang, Y. & Rossmann, M. G. Structure of bacteriophage ϕ29 head fibers has a supercoiled triple repeating helix-turn-helix motif. *Proc. Natl. Acad. Sci.* **108**, 4806 (2011).
33. van Raaij, M. J., Mitraki, A., Lavigne, G. & Cusack, S. A triple β-spiral in the adenovirus fibre shaft reveals a new structural motif for a fibrous protein. *Nature* **401**, 935–938 (1999).
34. Cheng, L. *et al.* Cryo-EM structures of two bovine adenovirus type 3 intermediates. *Virology* **450–451**, 174–181 (2014).
35. Liu, H. *et al.* Atomic Structure of Human Adenovirus by Cryo-EM Reveals Interactions Among Protein Networks. *Science* **329**, 1038 (2010).
36. Kihara, A., Akiyama, Y. & Ito, K. Host regulation of lysogenic decision in bacteriophage lambda: transmembrane modulation of FtsH (HflB), the cII degrading protease, by HflKC (HflA). *Proc. Natl. Acad. Sci. USA* **94**, 5544–5549 (1997).
37. Noble, J. A. *et al.* The *Escherichia coli* hflA locus encodes a putative GTP-binding protein and two membrane proteins, one of which contains a protease-like domain. *Proc. Natl. Acad. Sci. USA* **90**, 10866–10870 (1993).
38. Dyson, Z. A. *et al.* Locating and Activating Molecular 'Time Bombs': Induction of Mycolata Prophages. *Plos One* **11**, e0159957 (2016).
39. Borysowski, J., Weber-Dąbrowska, B. & Górski, A. Bacteriophage Endolysins as a Novel Class of Antibacterial Agents. *Exp. Biol. Med.* **231**, 366–377 (2006).
40. Kraemer, J. A. *et al.* A Phage Tubulin Assembles Dynamic Filaments by an Atypical Mechanism to Center Viral DNA within the Host Cell. *Cell* **149**, 1488–1499 (2012).
41. Parmar, K. M., Gaikwad, S. L., Dhakephalkar, P. K., Kothari, R. & Singh, R. P. Intriguing Interaction of Bacteriophage-Host Association: An Understanding in the Era of Omics. *Front. Microbiol.* **8**, 559–559 (2017).
42. Htoo, H. H. *et al.* Bacterial Cytological Profiling as a Tool To Study Mechanisms of Action of Antibiotics That Are Active against *Acinetobacter baumannii*. *Antimicrob. Agents Chemother.* **63**, e02310–18 (2019).
43. Nonejuie, P. *et al.* Application of bacterial cytological profiling to crude natural product extracts reveals the antibacterial arsenal of *Bacillus subtilis*. *J. Antibiot.* **69**, 353–361 (2016).
44. Boonyawiwat, V. *et al.* Impact of farm management on expression of early mortality syndrome/acute hepatopancreatic necrosis disease (EMS/AHPND) on penaeid shrimp farms in Thailand. *J. Fish Dis.* **40**, 649–659 (2017).
45. De Schryver, P., Defoirdt, T. & Sorgeloos, P. Early mortality syndrome outbreaks: a microbial management issue in shrimp farming? *Plos Pathog.* **10**, e1003919–e1003919 (2014).
46. Li, F. *et al.* Genomic and biological characterization of the *Vibrio alginolyticus*-infecting "*Podoviridae*" bacteriophage, vB_ValP_IME271. *Virus Genes* **55**, 218–226 (2019).
47. Luo, P. *et al.* Complete genomic sequence of the *Vibrio alginolyticus* bacteriophage Vp670 and characterization of the lysis-related genes, cwlQ and holA. *BMC Genomics* **19**, 741 (2018).
48. Lin, Y. R., Chiu, C. W., Chang, F. Y. & Lin, C. S. Characterization of a new phage, termed ϕA318, which is specific for *Vibrio alginolyticus*. *Arch. Virol.* **157**, 917–926 (2012).
49. Kim, S. G. *et al.* Isolation and characterisation of pVa-21, a giant bacteriophage with anti-biofilm potential against *Vibrio alginolyticus*. *Sci. Rep.* **9**, 6284 (2019).
50. Katharios, P., Kalatzis, P. G., Kokkari, C., Sarropoulou, E. & Middelboe, M. Isolation and characterization of a N4-like lytic bacteriophage infecting *Vibrio splendidus*, a pathogen of fish and bivalves. *Plos One* **12**, e0190083 (2017).
51. Li, Y. *et al.* Complete Genomic Sequence of Bacteriophage H188: A Novel *Vibrio kanaloae* Phage Isolated from Yellow Sea. *Curr. Microbiol.* **72**, 628–633 (2016).
52. Jacquemot, L. *et al.* Therapeutic Potential of a New Jumbo Phage That Infects *Vibrio coralliilyticus*, a Widespread Coral Pathogen. *Front. Microbiol.* **9**, 2501 (2018).
53. Lal, T. M., Sano, M. & Ransangan, J. Genome characterization of a novel vibriophage VpKK5 (Siphoviridae) specific to fish pathogenic strain of *Vibrio parahaemolyticus*. *J. Basic Microbiol.* **56**, 872–888 (2016).

54. Lal, T. M., Sano, M. & Ransangan, J. Isolation and Characterization of Large Marine Bacteriophage (Myoviridae), VhKM4 Infecting *Vibrio harveyi*. *J. Aquat. Anim. Health* **29**, 26–30 (2017).
55. Stalin, N. & Srinivasan, P. Characterization of *Vibrio parahaemolyticus* and its specific phage from shrimp pond in Palk Strait, South East coast of India. *Biologicals* **44**, 526–533 (2016).
56. Matamp, N. & Bhat, S. G. Genome characterization of novel lytic *Myoviridae* bacteriophage ϕVP-1 enhances its applicability against MDR-biofilm-forming *Vibrio parahaemolyticus*. *Arch. Virol.* https://doi.org/10.1007/s00705-019-04493-6 (2019).
57. Xu, J., Wang, D., Gui, M. & Xiang, Y. Structural assembly of the tailed bacteriophage ϕ29. *Nat. Commun.* **10**, 2366 (2019).
58. Yu, X. *et al*. Cryo-EM structure of human adenovirus D26 reveals the conservation of structural organization among human adenoviruses. *Sci. Adv.* **3**, e1602670 (2017).
59. Bhardwaj, A., Molineux, I. J., Casjens, S. R. & Cingolani, G. Atomic structure of bacteriophage Sf6 tail needle knob. *J. Biol. Chem.* **286**, 30867–30877 (2011).
60. Lee, H. S., Choi, S., Shin, H., Lee, J. H. & Choi, S. H. *Vibrio vulnificus* Bacteriophage SSP002 as a Possible Biocontrol Agent. *Appl. Environ. Microbiol.* **80**, 515 (2014).
61. Alanis Villa, A., Kropinski, A. M., Abbasifar, R., Abbasifar, A. & Griffiths, M. W. Genome Sequence of Temperate *Vibrio parahaemolyticus* Bacteriophage vB_VpaS_MAR10. *J. Virol.* **86**, 13851 (2012).
62. Dedrick, R. M. *et al*. Engineered bacteriophages for treatment of a patient with a disseminated drug-resistant *Mycobacterium abscessus*. *Nat. Med.* **25**, 730–733 (2019).
63. Liu, J. *et al*. Antimicrobial drug discovery through bacteriophage genomics. *Nat. Biotechnol.* **22**, 185–191 (2004).
64. Drulis-Kawa, Z., Majkowska-Skrobek, G. & Maciejewska, B. Bacteriophages and phage-derived proteins - application approaches. *Curr. Med. Chem.* **22**, 1757–1773 (2015).
65. Wang, W., Li, M., Lin, H., Wang, J. & Mao, X. The *Vibrio parahaemolyticus*-infecting bacteriophage qdvp001: genome sequence and endolysin with a modular structure. *Arch. Virol.* **161**, 2645–2652 (2016).
66. Zermeño-Cervantes, L. A., Makarov, R., Lomelí-Ortega, C. O., Martínez-Díaz, S. F. & Cardona-Félix, C. S. Recombinant LysVPMS1 as an endolysin with broad lytic activity against *Vibrio parahaemolyticus* strains associated to acute hepatopancreatic necrosis disease. *Aquac. Res.* **49**, 1723–1726 (2018).
67. Ultee, E., Ramijan, K., Dame, R. T., Briegel, A. & Claessen, D. Chapter Two - Stress-induced adaptive morphogenesis in bacteria. In Advances in Microbial Physiology (ed. Poole, R. K.) **74**, 97–141 (Academic Press, 2019).
68. Peters, J. M. *et al*. A Comprehensive, CRISPR-based Functional Analysis of Essential Genes in Bacteria. *Cell* **165**, 1493–1506 (2016).
69. Roucourt, B. & Lavigne, R. The role of interactions between phage and bacterial proteins within the infected cell: a diverse and puzzling interactome. *Environ. Microbiol.* **11**, 2789–2805 (2009).
70. Zhao, X. *et al*. Global Transcriptomic Analysis of Interactions between *Pseudomonas aeruginosa* and Bacteriophage PaP3. *Sci. Rep.* **6**, 19237–19237 (2016).
71. Chaikeeratisak, V. *et al*. Assembly of a nucleus-like structure during viral replication in bacteria. *Science* **355**, 194 (2017).
72. Chaikeeratisak, V. *et al*. The Phage Nucleus and Tubulin Spindle Are Conserved among Large *Pseudomonas* Phages. *Cell Rep.* **20**, 1563–1571 (2017).
73. Junprung, W., Supungul, P. & Tassanakajon, A. HSP70 and HSP90 are involved in shrimp *Penaeus vannamei* tolerance to AHPND-causing strain of *Vibrio parahaemolyticus* after non-lethal heat shock. *Fish Shellfish Immunol.* **60**, 237–246 (2017).
74. Kumar, S., Stecher, G., Li, M., Knyaz, C. & Tamura, K. MEGA X: Molecular Evolutionary Genetics Analysis across Computing Platforms. *Mol. Biol. Evol.* **35**, 1547–1549 (2018).
75. Klockgether, J. *et al*. Genome Diversity of *Pseudomonas aeruginosa* PAO1 Laboratory Strains. *J. Bacteriol.* **192**, 1113 (2010).
76. Serwer, P. *et al*. Improved isolation of undersampled bacteriophages: finding of distant terminase genes. *Virology* **329**, 412–424 (2004).

Acknowledgements

This research was supported by the Thailand Research Fund and the Office of the Higher Education Commission MRG6180027 (V.C.), the Grant for Development of New Faculty Staff, Ratchadaphiseksomphot Endowment Fund (V.C.), and National Institutes of Health grant GM129245 (J.P.). This study was supported in part by the Japan Science and Technology Agency (JST)/Japan International Cooperation Agency (JICA), Science and Technology Research Partnership for Sustainable Development, SATREPS JPMJSA1806 (V.C.). P.N. was supported by the Thailand research fund and the office of the higher education commission (MRG6080081). We acknowledge Chulalongkorn University for its support of the Center of Excellence for Molecular Biology and Genomics of Shrimp. We used the UCSD Cryo-Electron Microscopy Facility (supported by NIH grant R01-GM33050 to Dr. Timothy S. Baker and the Agouron Institute) and the fluorescence microscopy facility at the Advanced Cell Imaging Center, Institute of Molecular Biosciences, Mahidol University. We would like to thank John P. Davis and Savannah Senecal for bench-work assistance and helping with intellectual discussion, and Prof. Dr. Sirirat Rengpipat at Department of Microbiology, and Assoc. Prof. Dr. Kunlaya Somboonwiwat at Department of Biochemistry, Faculty of Science, Chulalongkorn University for offering *Vibrio* strains for host-range determination.

Author contributions

K.T., M.E.E., H.H.H., K.K., and V.C. conducted experiments, analyzed and interpreted data, and prepared the figures. J.S. and J.F.N. conducted experiments and collected data. K.T., M.E.E., K.K., J.P., P.N., and V.C. contributed to writing the manuscript. V.C. conceived the project and supervised all experiments. K.T., M.E.E., H.H.H., E.V., A.T., J.P., P.N., V.C. edited and approved the manuscript.

Competing interests

The authors declare no competing interests.

Additional information

Supplementary information is available for this paper at https://doi.org/10.1038/s41598-020-59396-3.

Correspondence and requests for materials should be addressed to V.C.

Reprints and permissions information is available at www.nature.com/reprints.

Publisher's note Springer Nature remains neutral with regard to jurisdictional claims in published maps and institutional affiliations.

Accepted manuscript ฉบับที่ 2 (งานวิจัยเสริม)

วารสาร Cell ซึ่งเป็นวารสารที่อยู่ใน Quartile in Category Q1 และมี Impact Factor 36.216

Chaikeeratisak, V., Khanna, K., Nguyen, K.T., Sugie, J., Egan, M.E., Erb, M.L., Vavilina, A., Nonejuie, P., Nieweglowska, E., Pogliano, K., et al. (2019). Viral Capsid Trafficking along Treadmilling Tubulin Filaments in Bacteria. Cell 177, 1771-1780.e12.

Article

Cell

Viral Capsid Trafficking along Treadmilling Tubulin Filaments in Bacteria

Graphical Abstract

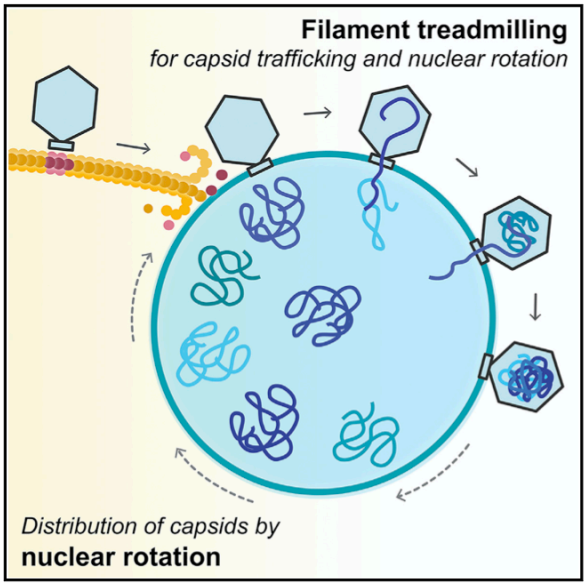

Authors

Vorrapon Chaikeeratisak, Kanika Khanna, Katrina T. Nguyen, ..., David A. Agard, Elizabeth Villa, Joe Pogliano

Correspondence

evilla@ucsd.edu (E.V.), jpogliano@ucsd.edu (J.P.)

In Brief

Bacteriophage-encoded tubulin-like proteins form treadmilling filaments in their bacterial host to transport viral capsids to the subcellular compartment where phage DNA is replicated and transcribed.

Highlights

- Capsids traffic along a viral encoded tubulin filament
- Treadmilling of the filament provides the mechanism of capsid movement through the cell
- Rotation of phage nucleus by the filament distributes capsids for efficient DNA packaging

Chaikeeratisak et al., 2019, Cell 177, 1771–1780
June 13, 2019
https://doi.org/10.1016/j.cell.2019.05.032

CellPress

Article

Cell

Viral Capsid Trafficking along Treadmilling Tubulin Filaments in Bacteria

Vorrapon Chaikeeratisak,[1,2] Kanika Khanna,[1] Katrina T. Nguyen,[1] Joseph Sugie,[1] MacKennon E. Egan,[1] Marcella L. Erb,[1] Anastasia Vavilina,[1] Poochit Nonejuie,[3] Eliza Nieweglowska,[4] Kit Pogliano,[1] David A. Agard,[4] Elizabeth Villa,[1,*] and Joe Pogliano[1,5,*]

[1]Division of Biological Sciences, University of California, San Diego, San Diego, CA 92093, USA
[2]Department of Biochemistry, Faculty of Science, Chulalongkorn University, Bangkok, 10330, Thailand
[3]Institute of Molecular Biosciences, Mahidol University, Nakhon Pathom 73170, Thailand
[4]Department of Biochemistry and Biophysics and the Howard Hughes Medical Institute, University of California, San Francisco, San Francisco, CA 94158, USA
[5]Lead Contact
*Correspondence: evilla@ucsd.edu (E.V.), jpogliano@ucsd.edu (J.P.)
https://doi.org/10.1016/j.cell.2019.05.032

SUMMARY

Cargo trafficking along microtubules is exploited by eukaryotic viruses, but no such examples have been reported in bacteria. Several large *Pseudomonas* phages assemble a dynamic, tubulin-based (PhuZ) spindle that centers replicating phage DNA sequestered within a nucleus-like structure. Here, we show that capsids assemble on the membrane and then move rapidly along PhuZ filaments toward the phage nucleus for DNA packaging. The spindle rotates the phage nucleus, distributing capsids around its surface. PhuZ filaments treadmill toward the nucleus at a constant rate similar to the rate of capsid movement and the linear velocity of nucleus rotation. Capsids become trapped along mutant static PhuZ filaments that are defective in GTP hydrolysis. Our results suggest a transport and distribution mechanism in which capsids attached to the sides of filaments are trafficked to the nucleus by PhuZ polymerization at the poles, demonstrating that the phage cytoskeleton evolved cargo-trafficking capabilities in bacteria.

INTRODUCTION

Microtubules play a key role in intracellular cargo trafficking in eukaryotes. Many viruses exploit microtubule trafficking to translocate from the surface of the plasma cell membrane to the cell interior, such as to the nucleus to initiate viral replication (Cohen et al., 2011; Greber and Way, 2006; Portilho et al., 2016; Sodeik et al., 1997). Newly assembled viral particles also traffic along microtubules to reach the surface of the cell for egress (Greber and Way, 2006; Ward, 2011). In addition to serving as a conduit for movement of mature particles in and out of cells, microtubules have been shown to be important for other steps of viral replication, including providing transportation for capsids (Dohner et al., 2002; Sodeik et al., 1997) or viral RNA-protein complexes (Nturibi et al., 2017) or by contributing to efficient capsid formation (Iwamoto et al., 2017). In contrast to eukaryotes, cargo trafficking along tubulin filaments has not been reported in bacteria.

We recently described a family of *Pseudomonas* phages that assemble a bipolar spindle composed of a tubulin-like protein (PhuZ) (Erb et al., 2014; Kraemer et al., 2012; Zehr et al., 2014). PhuZ is expressed by phage 201Φ2-1 early during infection of *P. chlororaphis*, where it forms three-stranded filaments (Erb et al., 2014; Kraemer et al., 2012; Zehr et al., 2014, 2018) that spatially organize viral replication. Like eukaryotic microtubules, PhuZ filaments are polarized, with kinetically distinct plus and minus ends. PhuZ polymers display dynamic instability *in vitro* and *in vivo*; that is, filaments can cease growing at their plus ends, catastrophically depolymerize, and then be rescued to start growing again (Erb et al., 2014; Kraemer et al., 2012). Notably, a different behavior, treadmilling, in which polymerization at the plus end of the filament is matched by depolymerization at the minus end, has been observed with *in vitro*-assembled PhuZ polymers (Erb et al., 2014), but it has remained unclear whether filaments of the spindle can also treadmill *in vivo*.

The PhuZ spindle plays a key role in phage reproduction by positioning replicating phage DNA in the center of the cell (Erb et al., 2014; Kraemer et al., 2012). Phage 201Φ2-1 DNA is encased by a proteinaceous shell composed of gp105, forming a nucleus-like structure, referred to as the phage nucleus, that compartmentalizes proteins according to function (Chaikeeratisak et al., 2017b). Early during infection, the dynamically unstable filaments of the PhuZ spindle push the nucleus from the cell pole to the midcell where it then oscillates in position (Erb et al., 2014; Chaikeeratisak et al., 2017b). Proteins involved in DNA replication and transcription localize inside the phage nucleus, while ribosomes and proteins involved in metabolic processes localize in the cytoplasm on the outside (Chaikeeratisak et al., 2017b). The nucleus likely provides protection for phage DNA by excluding proteins of the host defense systems (restriction systems, nucleases, and CRISPR-Cas) that target invading phage DNA (Chaikeeratisak et al., 2017a, 2017b; Mendoza et al., 2018). The phage spindle and nucleus are conserved among the related large phages ΦPA3 and ΦKZ that replicate in *P. aeruginosa* (Aylett et al., 2013; Chaikeeratisak et al., 2017a).

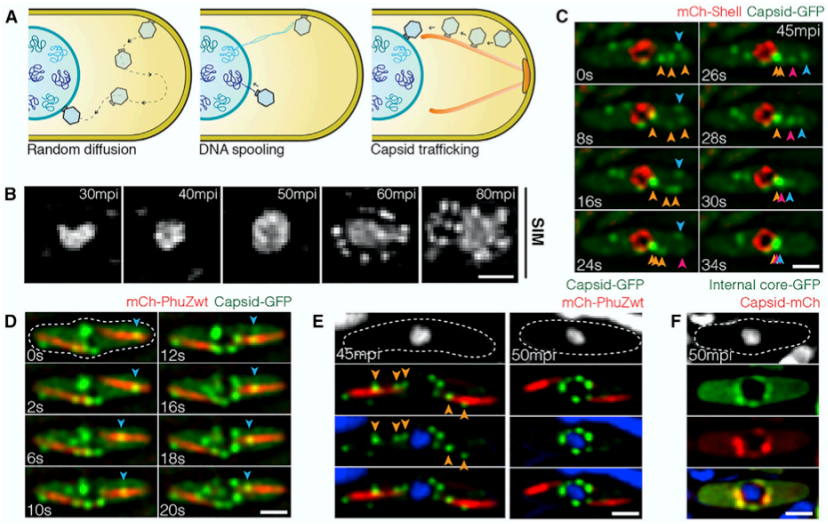

Figure 1. Phage Capsids Traffic along PhuZ Filaments to the Phage Nucleus for DNA Encapsidation by 60 mpi

(A) Three possible models of capsid trajectory toward the phage nucleus.

(B) 3D-SIM images showing appearance of the phage nucleus at various developmental stages of infected *P. chlororaphis* cells. The phage nucleus shows uniform staining in the first 50 min of infection. At 60 min post infection (mpi), bright puncta appear surrounding the phage nucleus. Scale bars, 0.5 micron.

(C) Rapid time-lapse imaging of GFP-tagged capsid (gp200; green) and mCherry-tagged shell (gp105; red) in *P. chlororaphis* infected with phage 201Φ2-1 over a 34 s interval. Capsids (green) assemble near the cell membrane, and immediately after detachment, they independently migrate along the same straight-line trajectory toward the phage shell (red). Arrows indicate individual capsids. See also Data S1 (see Movie 1).

(D) Rapid time-lapse imaging of GFP-tagged capsids (gp200; green) and mCherry-tagged wild-type PhuZ (gp059; red) during an interval of 20 s in phage 201Φ2-1-infected *P. chlororaphis* cells. Blue arrow indicates a capsid traveling along the PhuZ spindle from the cell pole to phage nucleus. See also Data S1 (see Movie 3).

(E) Still images of phage 201Φ2-1-infected *P. chlororaphis* cells expressing GFP-tagged capsid (gp200; green) and mCherry-tagged wild-type PhuZ (gp059; red) at 45 and 50 mpi.

(F) Still images of phage 201Φ2-1-infected *P. chlororaphis* cells expressing GFP-tagged internal core protein (gp246; green) and mCherry-tagged capsid (gp200; red) at 50 mpi.

Dashed lines indicate cell borders. Scale bars in (C)–(F), 1 micron. See also Figures S1 and S2.

Curiously, phage capsids assemble on the plasma membrane but must dock on the surface of the phage nucleus in order to package phage DNA (Chaikeeratisak et al., 2017a, 2017b). How capsids relocate from the membrane to the surface of the phage nucleus was unclear and potentially explained by three models (Figure 1A): (1) via "random diffusion" through the cell until capsids make contact with the nuclear shell; (2) via "DNA spooling," in which strands of phage DNA emanating from the phage nucleus are captured by the packaging ATPase at the base of the capsid and the process of spooling DNA into the capsid transports them to the shell surface; or (3) via "capsid trafficking," in which the PhuZ spindle plays a role in transporting capsids to the phage nucleus.

Here, we explore the mechanisms underlying capsid movement during phage infection. Using time-lapse microscopy and cryo-electron tomography (cryo-ET), we show that capsids move rapidly and directionally along PhuZ filaments but become trapped along mutant PhuZ filaments that are defective in guanosine triphosphate (GTP) hydrolysis. Photobleaching studies demonstrate that filaments of the spindle treadmill toward the nucleus, providing a simple mechanism by which capsids might be transported.

RESULTS

Capsids Move Directionally along PhuZ Filaments

To investigate models for capsid movement, we used rapid time-lapse imaging of GFP-tagged capsids and followed their movement from the cell membrane to the phage nuclear shell. We first identified the stage of infection during which capsids relocate by using DAPI staining and super-resolution fluorescence microscopy to determine approximately when DNA packaging occurs. DAPI staining of *P. chlororaphis* cells infected with phage 201Φ2-1 showed that nuclear staining intensity increased as DNA replicated until 50 min post infection (mpi) and that viral particles containing packaged DNA accumulated around the phage nucleus at 60 mpi (Figures 1B and S1A). We therefore used time-lapse imaging to study capsid trafficking between 40 and 60 mpi

by simultaneously imaging fluorescently labeled capsids (gp200) and shells (gp105). *P. chlororaphis* cells expressing gp200-GFP and mCherry-gp105 were infected with phage 201Φ2-1, and at approximately 45 mpi when capsid assembly occurs, cells were imaged every 2 s for 2 min. In Figure 1C, multiple capsids (green foci) were observed to assemble on the cell membrane, where they remained motionless for several seconds (Data S1, see Movie 1) (Chaikeeratisak et al., 2017b). Capsids then independently followed a linear trajectory, seemingly traveling on the same intracellular track directly to the phage nucleus where they docked (Figure 1C; Data S1, see Movie 1). Movement was directional and rapid, with capsids traveling over 1 micron in length in fewer than 30 s. These results suggest that capsids move via either model 2 (DNA spooling) or model 3 (capsid trafficking) (Figure 1A). We obtained similar results with phage ΦPA3 infecting *P. aeruginosa.* Rapid time-lapse imaging of GFP-tagged PA3-capsids (gp136) and mCherry-tagged PA3-shell (gp053) showed that the trajectory of the capsids was a straight line moving rapidly toward midcell (Figure S1B; Data S1, see Movie 2).

To determine whether the PhuZ spindle is involved in capsid movement, we imaged GFP-tagged capsids with either mCherry-tagged wild-type PhuZ or a PhuZD190A mutant that blocks GTP hydrolysis. We infected *P. chlororaphis* cells expressing gp200 (capsid)-GFP and either wild-type mCherry-PhuZ or mutant mCherry-PhuZD190A and visualized capsid assembly and movement in time-lapse microscopy beginning at 45 mpi. Our capsid-PhuZ co-localization experiments demonstrated that, as capsids traveled through the cell toward the phage nucleus, they co-localized with PhuZ polymers and appeared to travel on the same path along the PhuZ filaments in both time-lapse (Figure 1D; Data S1, see Movie 3) and still images (Figure 1E, left). By 50 mpi, most capsids were docked on the phage nucleus (Figure 1E, right). Capsids co-localized with another protein involved in capsid assembly (internal core protein gp246), suggesting that the capsids that dock on the surface of the phage nucleus are fully assembled (Figure 1F).

PhuZ Mutants Defective in GTP Hydrolysis Block Capsid Migration and Rotation of the Phage Nucleus

In *P. chlororaphis* cells expressing the mutant mCherry-PhuZD190A, phage 201Φ2-1 capsids lined the filaments at both 50 mpi and 70 mpi (Figure 2A, arrows). In time-lapse microscopy, the capsids appeared to be immobilized on the sides of the PhuZ filaments (Figures 2C and S2C; Data S1, see Movie 4). Similar results were found for closely related phage ΦPA3, which replicates in *P. aeruginosa* by a similar mechanism (Chaikeeratisak et al., 2017b). ΦPA3 capsids individually travelled along similar trajectories (Figure S1B; Data S1, see Movie 2) and co-localized with and migrated along wild-type PhuZ filaments (Figure S1C; Data S1, see Movie 5). In the presence of catalytically defective PhuZD190A, ΦPA3 capsids became statically attached to filaments (Figures 2B, 2D, S2A, S2B, and S2D; Data S1, see Movie 6).

DAPI staining was used as a way to assess, independently of GFP fusions, whether the expression of the PhuZD190A mutant interfered with capsid trafficking, which is required for DNA packaging at the phage nucleus. As previously reported (Chaikeeratisak et al., 2017a, 2017b), capsids containing DNA accumulated on the phage nucleus by 60 mpi (Figure 1B). However, in the presence of PhuZD190A, the number of encapsidated phage particles decreased approximately 5-fold (from an average of 10.5 to 2.1 particles), suggesting that capsid DNA packaging is delayed (Figures 2G and 2H). Taken together, our results suggest that capsids rely upon the PhuZ spindle to migrate rapidly to the phage nucleus and the GTP hydrolysis mutations in PhuZ trap capsids along static filaments and therefore delay DNA packaging.

To further confirm the difference in capsid positioning between cells expressing the wild-type or PhuZD190A mutant at 50 mpi, we quantitated gp200 (capsid)-GFP position from 32 infected cells. We plotted capsid position versus normalized cell length and found that the distribution of capsids is biased toward the midcell near the nucleus in cells expressing wild-type PhuZ, with approximately 63% of capsids occurring within 30% of the cell midpoint (Figures 2E and 2F). However, in the presence of the PhuZD190A mutant, the capsids are more evenly distributed throughout the cell (Figures 2E and 2F). The effect of the PhuZD190A catalytic mutation on capsid distribution is consistent with the PhuZ spindle playing a role in capsid migration.

We then used cryo-focused ion beam milling (cryo-FIB) coupled with cryo-ET to visualize capsids associated with filaments at high resolution in a near-native state (Chaikeeratisak et al., 2017b). Since capsids only transiently interacted with filaments as they translocated to the phage nucleus in wild-type cells, we performed cryo-FIB-ET on cells expressing PhuZD190A mutants in which capsids appeared to become trapped. In samples of *P. aeruginosa* cells expressing mutant PhuZD190A and infected with phage ΦPA3 for 70 min, 18 empty capsids (green) were clustered around PhuZ filaments (blue) in a ~200 nm slice of the sample (Figure 3A, 3B, and S2E). At this time point, capsids are normally filled with DNA in wild-type cells (Figure S2F), yet these capsids are empty, suggesting that capsids associated with the mutant PhuZ filaments are unable to traffic to the nucleus for DNA packaging, in agreement with fluorescence microscopy data (Figure 2G). Since capsids appear in close proximity (3–4 nm) to the filament (Figures 3C–3H), we attempted to identify amino acids that are conserved on the outer surface of PhuZ filaments that might possibly serve as a point of attachment. Three aspartic acid residues (D235, D259, D263) that are conserved among PhuZ proteins encoded by ΦPA3, ΦKZ, and 201Φ2-1 were mutated to alanine (Figure S3D). One of them, D235A, completely blocked filament assembly (data not shown). The mutants D259A and D263A retained their ability to assemble filaments, while the double mutant, D259A-D263A, appeared slightly impaired in filament formation. We examined the ability of capsids to traffic along all three of these mutant filaments using time-lapse microscopy (Figure S3C). We also examined DNA packaging into capsids (a hallmark of successful trafficking) and nucleus rotation in the three mutants (Figure S3B). In each case, capsids were still able to move along the mutant filaments, mature capsids filled with DNA were observed, and the phage nucleus rotated at midcell. Attempts to detect a direct interaction between PhuZ and capsid proteins using yeast two-hybrid systems also yielded a negative result (Figure S3A).

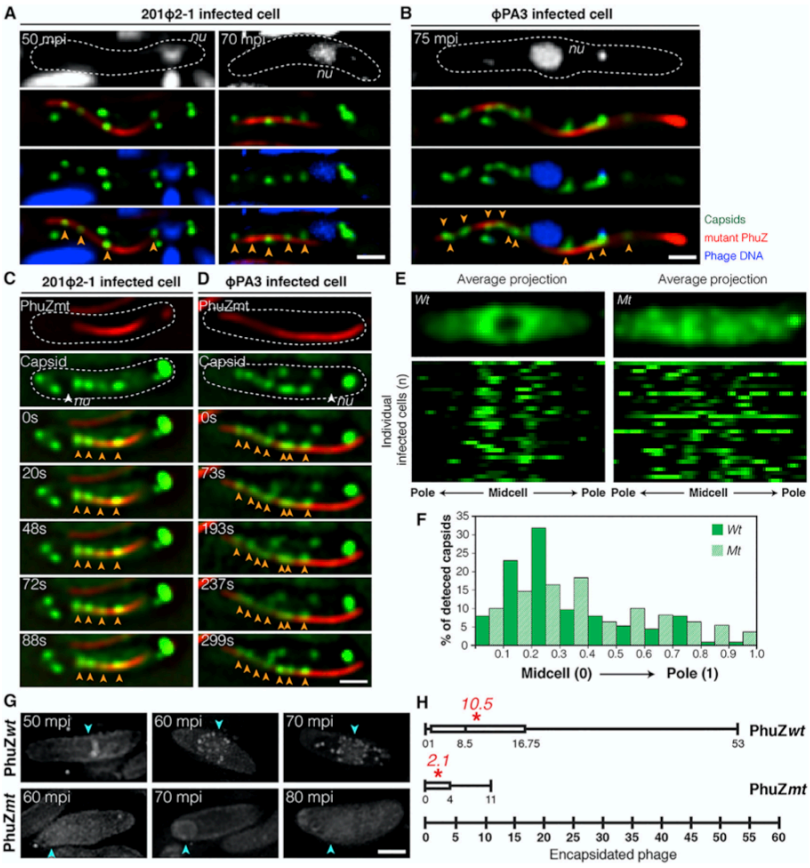

Figure 2. Phage Capsids Are Trapped along Mutant PhuZ Spindles in Both Phage 201Φ2-1 and Phage ΦPA3, Resulting in Reduced Encapsidation

(A) Fluorescence images of *P. chlororaphis* expressing GFP-tagged 201-capsid (gp200; green) and catalytically defective mCherry-tagged 201-PhuZD190A (gp059; red) infected with phage 201Φ2-1 at 50 and 70 mpi.

(B) Fluorescence images of *P. aeruginosa* expressing mCherry-tagged PA3-capsid (gp136; false color, green) and catalytically defective GFP-tagged PA3-PhuZD190A (gp028; false color, red) infected with phage ΦPA3 at 75 mpi.

(C) Time-lapse imaging of *P. chlororaphis* expressing GFP-tagged 201-capsid (gp200; green) with mCherry-tagged 201-PhuZD190A (gp059; red) over an interval of 88 s. See also Data S1 (see Movie 4).

(D) Time-lapse imaging of *P. aeruginosa* expressing mCherry-tagged PA3-capsid (gp136; false color, green) with GFP-tagged PA3-PhuZD190A (gp028; false color, red) over an interval of 299 s. See also Data S1 (see Movie 6).

(E) Distribution of GFP-tagged 201-capsids (gp200) in *P. chlororaphis* cells expressing either wild-type (left) or mutant (right) PhuZD190A infected with phage 201Φ2-1 at 50 mpi. Average Z-projection images (n = 32) of GFP intensity (top); distribution plots of GFP intensity of individuals (n = 32) (bottom).

(F) Graph showing percentage of detected GFP-tagged capsids in phage 201Φ2-1-infected *P. chlororaphis* cells expressing either wild-type (green) or mutant PhuZD190A (hatched bar) versus the fraction of cell length from the midcell to the cell pole.

(G) 3D-SIM images of encapsidated phage particles in phage 201Φ2-1-infected *P. chlororaphis* cells expressing either wild-type (top) or mutant (bottom) PhuZD190A at various time points. Arrows indicate positions of the phage nuclei.

(H) Box plot showing the number of encapsidated phage particles counted in phage 201Φ2-1-infected *P. chlororaphis* cells expressing either wild-type (top) or mutant (bottom) PhuZ at 80 mpi.

Asterisks indicate the average number of the encapsidated particles counted per strain. Dashed lines indicate the border of the cells. Scale bars, 1 micron. See also Figure S2.

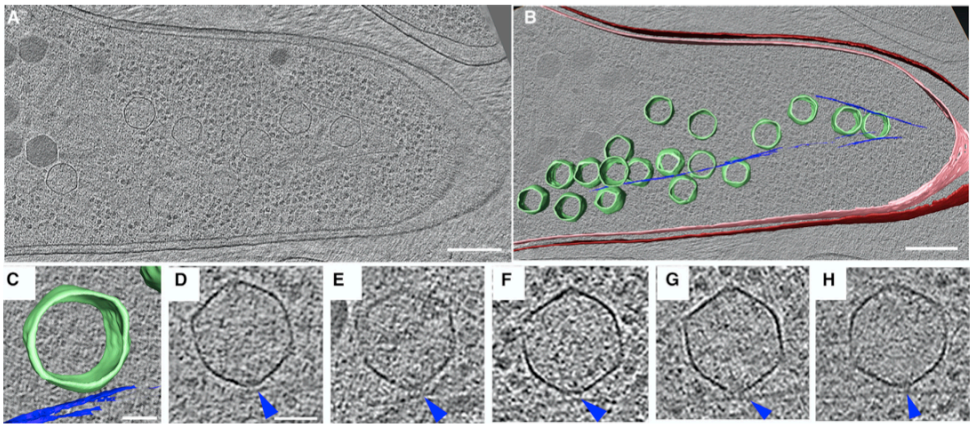

Figure 3. Cryo-electron Tomography Revealing Capsids Trapped along Mutant PhuZ Filaments during Phage ΦPA3 Infection in *P. aeruginosa* at 70 mpi

(A) A slice through a tomogram of a cryo-focused ion beam–thinned phage-infected cell at 70 mpi. Scale bar, 200 nm.

(B) Annotation of the tomogram in (A) showing extracted structures, including capsids (green), cytoplasmic membrane (pink), outer membrane (red), and mutant PhuZD190A spindles (blue). Scale bar, 200 nm.

(C and D) Zoomed-in view (C) of one of the capsids stuck on the mutant filament from the tomogram shown in (A) and its corresponding tomogram slice (D). Scale bar, 50 nm.

(E–H) Slices of tomograms of capsids trapped along the mutant filaments from tomograms of other phage-infected cells taken for this study, with blue arrow pointing towards the mutant spindle.

See also Figure S2.

During phage 201Φ2-1 infection, the phage nucleus is pushed from the cell pole to the cell midpoint where, at approximately 40–45 mpi, it suddenly begins to rotate in position (Chaikeeratisak et al., 2017b) (Figures 4A and S4A; Data S1, see Movie 7). Figure 4A and Data S1 (see Movie 7) show an example of a phage nucleus (green) being pushed transversely by the PhuZ spindle (red) and undergoing approximately two revolutions within 60 s, with an average linear velocity of 43.6 ± 7.6 nm/s (n = 10). In contrast, phage nuclei formed in the presence of mutant PhuZD190A are both mispositioned and do not rotate (Figures 4B and S4B; Data S1, see Movie 8). At 45 mpi, 46% (n = 611) of the wild-type nuclei underwent rotations in the presence of wild-type filaments, while in the presence of the PhuZD190A mutant, less than 6% (n = 286) rotated (Figure 4D). The sudden onset of phage nucleus rotation, which occurs at approximately the same time as capsid movement begins, suggests a switch in the dynamics of the PhuZ spindle from primarily centering the phage nucleus to rotating it.

Rotation is dependent upon the dynamic GTPase activity of the PhuZ spindle, raising the question of what role rotation might play in phage reproduction. In our time-lapse co-localization experiments, capsids trafficked along the spindle and docked on the rotating shell (Figure 4C; Data S1, see Movie 9). The process of rotation appears to distribute capsids widely around the nuclear shell. We obtained identical results with phage ΦPA3 in *P. aeruginosa*: capsids traveled along PhuZ filaments and docked on the rotating phage nucleus, where they then rotated together (Figures S4C and S4D; Data S1, see Movies 10 and 11), showing that this mechanism is conserved among this family of large *Pseudomonas* phages.

GTP-Dependent Treadmilling of PhuZ Filaments Is Responsible for Capsid Movement and Rotation of the Phage Nucleus

The mechanism underlying capsid movement along filaments was unclear. In eukaryotic cells, cargo trafficking along microtubules is typically dependent upon motor proteins such as kinesin and dynein that use ATP hydrolysis to drive unidirectional transport. However, phage and bacteria are generally thought to lack such motor proteins. Therefore, we explored the possibility that capsid movement is driven by filament treadmilling. In this model, insertion of new subunits occurs at one end of the filaments located near the cell poles, thereby driving capsids attached to the sides of the filaments toward midcell. To determine whether spindle filaments treadmill, we used photobleaching to mark one end of the spindle after approximately 45–50 mpi, when capsids are migrating to the nucleus. As shown in Figures 5A and 5B, bleached zones (arrows) near the ends of the spindles moved rapidly toward the nucleus (Data S1, see Movies 12 and 13). The median rate of bleached-zone movement through the cell was 51.5 nm/s (n = 40; Figures 5C and 5E), suggesting that filaments treadmill at a constant rate with no evidence of significant pausing even when taking images more frequently (Figure S5B) or expanding the length of the cells

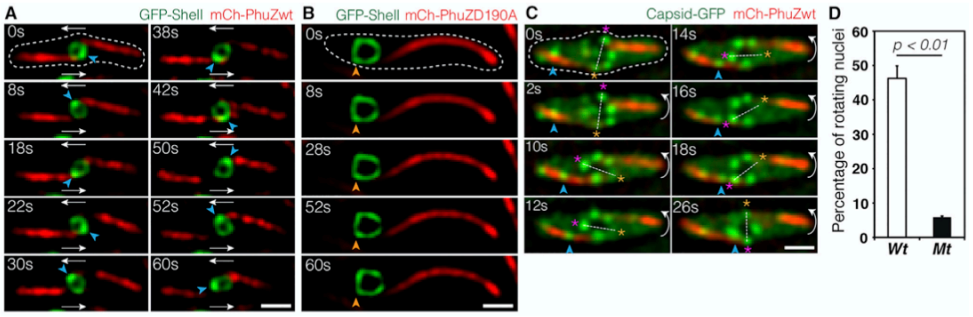

Figure 4. Rotation of the Phage Nucleus Exerted by PhuZ Spindle Distribute Phage Capsids around the Nucleus

(A and B) Rapid time-lapse imaging of phage 201Φ2-1-infected *P. chlororaphis* expressing GFP-tagged shell (gp105) with either mCherry-tagged wild-type PhuZ (gp059) (A) or mCherry-tagged mutant PhuZD190A (gp059) (B) during 60 s intervals. In the presence of wild-type filaments, the shell (green) rotates counterclockwise when the PhuZ filaments push the shell transversely; the shell successfully rotates twice within 42 s. The mutant PhuZD190A is unable to catalyze GTP hydrolysis and appears static, resulting in a mispositioned and motionless shell within the infected cell. See also Data S1 (see Movies 7 and 8).

(C) Rapid time-lapse microscopy of phage 201Φ2-1-infected *P. chlororaphis* expressing GFP-tagged capsid (gp200) and mCherry-tagged wild-type PhuZ (gp059) in a 26 s interval. A capsid (arrow) travels along the filament from cell pole toward the phage nucleus, which rotates counterclockwise. The capsid docks on the surface of the nucleus at 26 s. Dashed lines indicate cell borders. Scale bars, 1 micron. See also Data S1 (see Movie 9).

(D) Graph showing the percentage of rotating nuclei in *P. chlororaphis* infected cells in the presence of either wild-type PhuZ (wt) or mutant PhuZD190A (mt). The graph shows that the number of rotating nuclei in the presence of wild-type PhuZ (46.2%) is significantly higher ($p < 0.01$) than that in the presence of mutant PhuZD190A (5.9%). Data were collected from infected cells at 50 mpi from at least three different fields and are represented as mean ± SE (n; wt = 611 and mt = 286).

See also Figure S4.

with antibiotics to increase the distance of travel (Figure 5C). In all cases, regardless of filament length, bleached zones moved at a constant rate toward midcell. When both sides of a bipolar spindle were bleached, the two bleached zones migrated in unison toward the cell center with similar rates, arriving at the nucleus at the same time (Figure 5B; Data S1, see Movie 13). Quantitation of the rate of capsid migration toward the nucleus revealed that they move with a median rate of 50.3 nm/s (n = 10; Figures 5D and 5E), very similar to the rate of treadmilling (51.5 nm/s, n = 40). In the presence of the PhuZD190A mutant, the average rates of filament treadmilling and capsid migration both fall to near zero (Figures 5E and S4E; Data S1, see Movie 14). These results suggest that filaments of the spindle require GTP hydrolysis to treadmill and transport capsids toward the nucleus (Figure 5F), providing a potential mechanism for capsid migration driven by net filament growth near the poles and net loss near the nucleus. Nucleus rotation also occurred at a similar rate and was dependent upon PhuZ GTP hydrolysis, suggesting that treadmilling is responsible for both capsid movement and rotation, thereby temporally coupling these two processes.

DISCUSSION

Our results suggest a model in which capsids assemble on the host cell membrane and migrate along filaments of the PhuZ spindle to reach the phage nucleus (Figure 6). Delivering capsids directly to the surface of the shell increases the rate at which these large phage particles dock and begin the process of DNA encapsidation. Rotation of the nucleus by the spindle likely serves to distribute the capsids more evenly around the shell surface, maximizing efficient DNA packaging (Figure 6E). These phage genomes are 316 kilobases (kb) (phage 201Φ2-1) and 309 kb (phage ΦPA3) in size, and therefore occupy substantial space inside the phage nucleus. If two particles docked immediately adjacent to one another, only one might be able to package DNA. Capsid trafficking is driven by GTP-dependent PhuZ polymerization and is conserved between phages 201Φ2-1 and ΦPA3 and likely other phages containing PhuZ homologs (Figure S5). PhuZ is conserved in a number of large phage genomes, including those that infect *Vibrio* and *Erwinia* (Figure S5C). These results show that phages evolved a mechanism for trafficking cargo using a cytoskeletal element in bacteria.

Our results suggest a simple transport mechanism in which treadmilling filaments are responsible for rapid and directional capsid movement. Newly formed capsids release from the membrane, diffuse a short distance, and attach to the sides of filaments (Figures 6C–6F). As new subunits are added to filament ends located at the cell poles, capsids are transported by the polymer to the phage nucleus. Capsids are released from filaments when they reach the depolymerizing ends adjacent to the nucleus, allowing them to dock on the phage nuclear surface (Figures 6E and 6F). This model is supported by our finding that PhuZ subunits flux toward the nucleus at a rate almost identical to the rate of capsid movement.

Upon DNA injection and formation of the phage nucleus, spindle assembly begins when PhuZ monomers nucleate to form a hexameric structure to which additional monomers are added (Zehr et al., 2014). The filaments of the PhuZ spindle use dynamic instability to position and maintain the phage nucleus at midcell (Figures 6A and 6B) (Erb et. al., 2014; Kraemer et. al., 2012). We

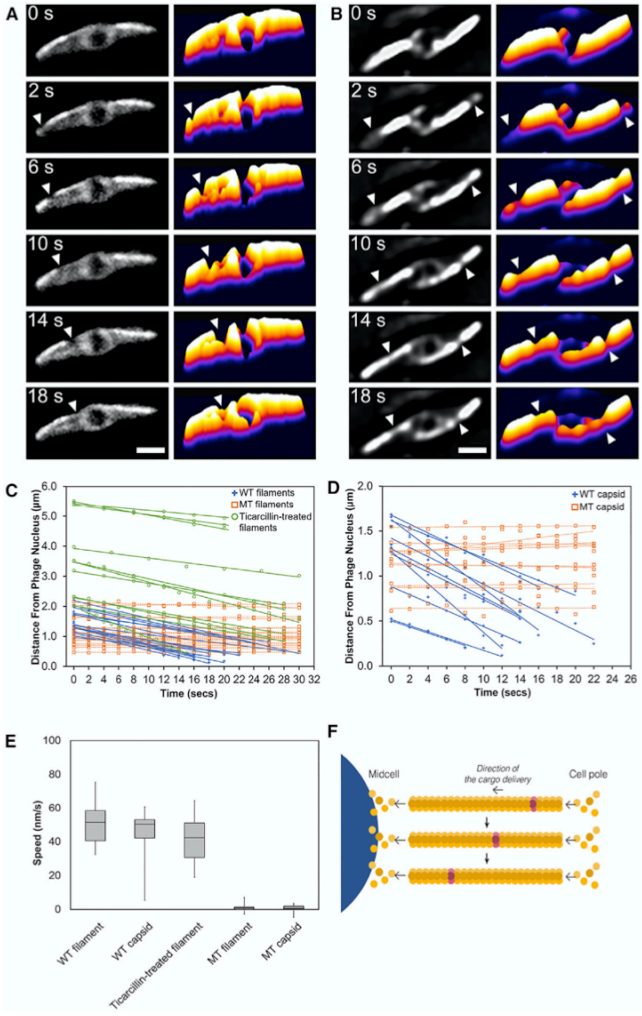

Figure 5. PhuZ Filaments Treadmill Unidirectionally toward the Nucleus at a Constant Rate

(A) A single photobleaching event at the cell pole (arrow) moves toward the phage nucleus. See also Data S1 (see Movie 12).

(B) A double photobleaching event shows that bleach spots made at both cell poles (arrows) flux down the filaments toward the phage nucleus. Scale bars, 1 micron. See also Data S1 (see Movie 13).

(C) Graph showing rates of bleach-spot movement (distance in microns versus time in seconds) in wild-type ΦPA3-PhuZ filaments, mutant ΦPA3-PhuZD190A filaments, and wild-type ΦPA3-PhuZ filaments treated with the antibiotic ticarcillin to produce elongated cells.

(D) Graph showing rates of capsid movement (distance in microns versus time in seconds) when co-expressed with either wild-type ΦPA3-PhuZ or the mutant ΦPA3-PhuZD190A.

(E) Box-and-whisker plots showing average speeds of movement of bleach spots on wild-type PA3 PhuZ filaments (WT filament), on wild-type PA3 PhuZ filaments in ticaricillin-treated cells (ticaricillin-treated filament), or on mutant PA3 PhuZD190A filaments (MT filament). Average speed of capsid movement in cells with wild PA3 PhuZ filaments (WT capsid) or mutant PA3 PhuZD190A filaments (MT capsid).

(F) Model of PhuZ filament treadmilling, indicating that addition of new subunits causes the bleached subunits (gray) to flux toward the nucleus. See also Figures S4 and S5 and Data S1 (see Movie 14).

previously demonstrated that PhuZ filaments are intrinsically polar, with the plus end of the filament exhibiting rapid growth and dynamic instability *in vitro*. *In vivo*, the minus end of the filament is localized to the cell pole, and the dynamically unstable plus end is oriented toward midcell (Figures 6A and 6B). Later during phage replication, the behavior of the spindle changes from positioning the nucleus at midcell (Figures 6A and 6B) to rotating it in position concomitant with the transport of capsids (Figures 6C and 6D), suggesting developmental regulation of spindle dynamics. PhuZ filaments flux toward the phage nucleus, suggesting that, given the previous demonstration of polarity, the minus ends located at the cell poles are capable of constant growth. While filament minus ends can also grow, albeit at a higher critical concentration than the plus ends, what is unexpected here is that minus-end growth and plus-end dynamic instability would exist simultaneously. While the cellular concentration of PhuZ monomers are unknown, proteomics experiments show that the total amount of PhuZ protein increases as infection progresses (Figure S5A), which could lead to altered filament dynamics over time. In isolated microtubules, the higher tubulin concentrations needed for minus-end growth would lead to rapid plus-end growth and less frequent catastrophic collapse, although both can occur simultaneously (Walker et al., 1988). However, the *in vivo* situation here is far more complex, leading to several plausible explanations: (1) the effective concentration of PhuZ could be higher at the poles than the midcell; (2) resistance imposed by centering the nucleus could accelerate depolymerization at the midcell; (3) bundling of the filaments toward the poles could stabilize the minus ends and enhance the effective on-rate. Previous work suggested that there is a phage-encoded mechanism for anchoring PhuZ

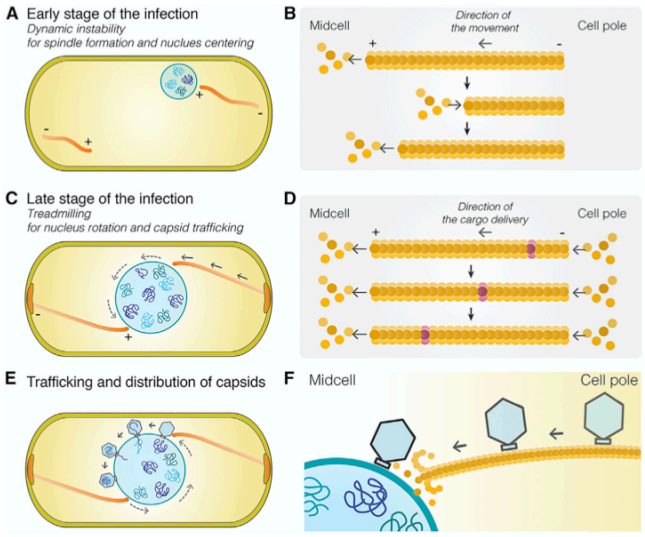

Figure 6. Model of Capsid Trafficking and the Role of Nucleus Rotation in Distributing Capsids around the Phage Nucleus

The spindle's functions are complex and change as phage development proceeds.

(A) At the onset of infection, dynamically unstable filaments assemble with minus ends anchored at the cell poles, and plus ends oriented toward midcell push the growing phage nucleus to the cell midpoint where it oscillates in position.

(B) Model of dynamically unstable filaments showing cycles of polymerization, depolymerization, and recovery at the plus end of the polymer.

(C) Later in infection, the function of the spindle switches from centering the nucleus to rotating it in position and transporting capsids to the phage nucleus for DNA packaging. Treadmilling provides the driving force and temporally couples both processes.

(D) Model of treadmilling filaments showing addition of new subunits at the minus end near the cell pole drives photobleached subunits (purple) toward midcell.

(E) Rotation of the phage nucleus serves to distribute capsids evenly around its surface.

(F) Capsids are delivered to the surface of the phage nucleus for DNA packaging.

filaments at the poles (Erb et. al., 2014) and that this could facilitate adding new subunits, much as the microtubule-associated protein XMAP215 does (Ayaz et al., 2014; Brouhard et al., 2008). *In vivo*, PhuZ filaments are clearly bundled along much of their length but splay near the midcell, becoming much harder to visualize (Erb et. al., 2014). *In vitro* studies have shown that non-dynamic PhuZ filaments are much more likely to bundle than their dynamic counterparts (Erb et al., 2014; Kraemer et al., 2012; Zehr et al., 2014). Thus, either the statistics of having many available minus ends or a structure altered by bundling could also accelerate minus-end addition. Given that the functions of the spindle change over time, it's not surprising that spindle behavior and dynamics are complex.

Microtubules also display different behaviors depending upon the specific cell type, buffer conditions, or accessory factors. While minus ends grow at a slower rate and higher threshold concentration than the plus ends, the specific conditions can affect the two ends in different ways. This variability in conditions leads to the observation of dynamic instability (Brouhard and Rice, 2018; Mitchison and Kirschner, 1984; Zhang et al., 2015) at both ends of a microtubule and treadmilling-like behavior (Grego et al., 2001; Margolis and Wilson, 2019; Rodionov et al., 1999; Rodionov and Borisy, 1997; Shaw et al., 2003; Waterman-Storer and Salmon, 1997a, 1997b). In fact, microtubules have been observed to treadmill in both the minus-to-plus and plus-to-minus directions *in vitro* (Grego et al., 2001). Similarly, our results show that PhuZ filaments are capable of displaying two distinct behaviors coupled to the spindle's biological functions: dynamic instability, which is essential for centering the phage nucleus, and treadmilling, which is necessary for transporting phage capsids and rotating the nucleus. These two types of behaviors are consistent with our prior studies, further illuminate the central role of the PhuZ cytoskeleton in phage reproduction, and highlight the plasticity of tubulins in assembling unique polymers tailored to performing specific cellular activities.

The nature of the proposed interaction between capsids and PhuZ polymers is unclear. In principle, capsids might associate with the sides of PhuZ filaments directly or indirectly via another protein. Precedence for capsids directly interacting with microtubules has been reported for several eukaryotic viruses. For example, the Hepatitis C virus interacts with tubulins, affects microtubule dynamics, and has been proposed to move through the cytoplasm by associating with dynamic microtubules (Roohvand et al., 2009). Our results suggest a common solution to viral transport that occurs in evolutionarily divergent domains of life.

STAR★METHODS

Detailed methods are provided in the online version of this paper and include the following:

- KEY RESOURCES TABLE
- CONTACT FOR REAGENT AND RESOURCE SHARING
- EXPERIMENTAL MODEL AND SUBJECT DETAILS
  - Strain, growth condition, and bacteriophage preparation
  - Plasmid constructions and bacterial transformation
- METHOD DETAILS
  - Single cell-infection assay
  - Fixed and live cell static-image fluorescence microscopy

- Time-lapse fluorescence microscopy
- 3D-Structured Illumination Microscopy
- Fluorescence Recovery After Photobleaching
- Yeast Two-hybrid assay
- Tomography Sample Preparation and Data Acquisition

● QUANTIFICATION AND STATISTICAL ANALYSIS

SUPPLEMENTAL INFORMATION

Supplemental Information can be found online at https://doi.org/10.1016/j.cell.2019.05.032.

ACKNOWLEDGMENTS

This research was supported by National Institutes of Health grants GM031627, R35GM118099 (D.A.A.), GM104556 (J.P. and D.A.A.), GM129245 (J.P. and E.V.), R01-GM57045 (K.P.), and 1DP2GM123494-01 (E.V.) and by the Howard Hughes Medical Institute (D.A.A.). V.C. was supported by the Thailand research fund and the office of the higher education commission (MRG6180027). P.N. was supported by the Thailand research fund and the office of the higher education commission (MRG6080081). We used the UCSD Cryo-EM Facility (supported by NIH grants to Dr. Timothy S. Baker and the Agouron Institute) and the San Diego Nanotechnology Infrastructure of UCSD (supported by the NSF grant ECCS-1542148). We would like to thank Ethan Garner and Arshad Desai for helpful discussions.

AUTHOR CONTRIBUTIONS

V.C., K.K., K.T.N., J.S., M.E.E., M.L.E., P.N., and A.V. conducted experiments, analyzed data, and contributed to writing the manuscript. E.N., K.P., D.A.A., E.V., and J.P. analyzed data and contributed to writing the manuscript.

DECLARATION OF INTERESTS

The authors declare no competing interests.

Received: May 11, 2018
Revised: January 24, 2019
Accepted: May 17, 2019
Published: June 13, 2019

REFERENCES

Ayaz, P., Munyoki, S., Geyer, E.A., Piedra, F.A., Vu, E.S., Bromberg, R., Otwinowski, Z., Grishin, N.V., Brautigam, C.A., and Rice, L.M. (2014). A tethered delivery mechanism explains the catalytic action of a microtubule polymerase. eLife *3*, e03069.

Aylett, C.H., Izoré, T., Amos, L.A., and Löwe, J. (2013). Structure of the tubulin/FtsZ-like protein TubZ from Pseudomonas bacteriophage ΦKZ. J. Mol. Biol. *425*, 2164–2173.

Brouhard, G.J., and Rice, L.M. (2018). Microtubule dynamics: an interplay of biochemistry and mechanics. Nat. Rev. Mol. Cell Biol. *19*, 451–463.

Brouhard, G.J., Stear, J.H., Noetzel, T.L., Al-Bassam, J., Kinoshita, K., Harrison, S.C., Howard, J., and Hyman, A.A. (2008). XMAP215 is a processive microtubule polymerase. Cell *132*, 79–88.

Chaikeeratisak, V., Nguyen, K., Egan, M.E., Erb, M.L., Vavilina, A., and Pogliano, J. (2017a). The Phage Nucleus and Tubulin Spindle Are Conserved among Large Pseudomonas Phages. Cell Rep. *20*, 1563–1571.

Chaikeeratisak, V., Nguyen, K., Khanna, K., Brilot, A.F., Erb, M.L., Coker, J.K., Vavilina, A., Newton, G.L., Buschauer, R., Pogliano, K., et al. (2017b). Assembly of a nucleus-like structure during viral replication in bacteria. Science *355*, 194–197.

Cohen, S., Au, S., and Pante, N. (2011). How viruses access the nucleus. Biochim. Biophys. Acta *1813*, 1634–1645.

Dohner, K., Wolfstein, A., Prank, U., Echeverri, C., Dujardin, D., Vallee, R., and Sodeik, B. (2002). Function of dynein and dynactin in herpes simplex virus capsid transport. Mol. Biol. Cell *13*, 2795–2809.

Erb, M.L., Kraemer, J.A., Coker, J.K., Chaikeeratisak, V., Nonejuie, P., Agard, D.A., and Pogliano, J. (2014). A bacteriophage tubulin harnesses dynamic instability to center DNA in infected cells. eLife *3*, e03197.

Greber, U.F., and Way, M. (2006). A superhighway to virus infection. Cell *124*, 741–754.

Grego, S., Cantillana, V., and Salmon, E.D. (2001). Microtubule treadmilling in vitro investigated by fluorescence speckle and confocal microscopy. Biophys. J. *81*, 66–78.

Iwamoto, M., Cai, D., Sugiyama, M., Suzuki, R., Aizaki, H., Ryo, A., Ohtani, N., Tanaka, Y., Mizokami, M., Wakita, T., et al. (2017). Functional association of cellular microtubules with viral capsid assembly supports efficient hepatitis B virus replication. Sci. Rep. *7*, 10620.

Kraemer, J.A., Erb, M.L., Waddling, C.A., Montabana, E.A., Zehr, E.A., Wang, H., Nguyen, K., Pham, D.S., Agard, D.A., and Pogliano, J. (2012). A phage tubulin assembles dynamic filaments by an atypical mechanism to center viral DNA within the host cell. Cell *149*, 1488–1499.

Kremer, J.R., Mastronarde, D.N., and McIntosh, J.R. (1996). Computer visualization of three-dimensional image data using IMOD. J. Struct. Biol. *116*, 71–76.

Lamprecht, M.R., Sabatini, D.M., and Carpenter, A.E. (2007). CellProfiler: free, versatile software for automated biological image analysis. Biotechniques *42*, 71–75.

Margolis, R.L., and Wilson, L. (2019). Microtubule treadmills—possible molecular machinery. Nature *293*, 705.

Martinez-Sanchez, A., Garcia, I., Asano, S., Lucic, V., and Fernandez, J.J. (2014). Robust membrane detection based on tensor voting for electron tomography. J. Struct. Biol. *186*, 49–61.

Mendoza, S.D., Berry, J.D., Nieweglowska, E.S., Leon, L.M., Agard, D., and Bondy-Denomy, J. (2018). A nucleus-like compartment shields bacteriophage DNA from CRISPR-Cas and restriction nucleases. bioRxiv. https://doi.org/10.1101/370791.

Mitchison, T., and Kirschner, M. (1984). Dynamic instability of microtubule growth. Nature *312*, 237–242.

Nturibi, E., Bhagwat, A.R., Coburn, S., Myerburg, M.M., and Lakdawala, S.S. (2017). Intracellular Colocalization of Influenza Viral RNA and Rab11A Is Dependent upon Microtubule Filaments. J. Virol. *19*, e01179-17.

Portilho, D.M., Persson, R., and Arhel, N. (2016). Role of non-motile microtubule-associated proteins in virus trafficking. Biomol. Concepts *7*, 283–292.

Rodionov, V.I., and Borisy, G.G. (1997). Microtubule Treadmilling in Vivo. Science *275*, 215–218.

Rodionov, V., Nadezhdina, E., and Borisy, G. (1999). Centrosomal control of microtubule dynamics. Proc Natl Acad Sci USA *96*, 115–120.

Roohvand, F., Maillard, P., Lavergne, J.P., Boulant, S., Walic, M., Andreo, U., Goueslain, L., Helle, F., Mallet, A., McLauchlan, J., et al. (2009). Initiation of hepatitis C virus infection requires the dynamic microtubule network: role of the viral nucleocapsid protein. J. Biol. Chem. *284*, 13778–13791.

Schindelin, J., Arganda-Carreras, I., Frise, E., Kaynig, V., Longair, M., Pietzsch, T., Preibisch, S., Rueden, C., Saalfeld, S., Schmid, B., et al. (2012). Fiji: an open-source platform for biological-image analysis. Nat. Methods *9*, 676–682.

Shaw, S.L., Kamyar, R., and Ehrhardt, D.W. (2003). Sustained microtubule treadmilling in Arabidopsis cortical arrays. Science *300*, 1715–1718.

Sodeik, B., Ebersold, M.W., and Helenius, A. (1997). Microtubule-mediated transport of incoming herpes simplex virus 1 capsids to the nucleus. J. Cell Biol. *136*, 1007–1021.

Walker, R.A., O'Brien, E.T., Pryer, N.K., Soboeiro, M.F., Voter, W.A., Erickson, H.P., and Salmon, E.D. (1988). Dynamic instability of individual microtubules analyzed by video light microscopy: rate constants and transition frequencies. J. Cell Biol. *107*, 1437–1448.

Ward, B.M. (2011). The taking of the cytoskeleton one two three: how viruses utilize the cytoskeleton during egress. Virology *411*, 244–250.

Waterman-Storer, C.M., and Salmon, E.D. (1997a). Actomyosin-based retrograde flow of microtubules in the lamella of migrating epithelial cells influences microtubule dynamic instability and turnover and is associated with microtubule breakage and treadmilling. J. Cell Biol. *139*, 417–434.

Waterman-Storer, C.M., and Salmon, E.D. (1997b). Microtubule dynamics: Treadmilling comes around again. Curr. Biol. *7*, R369–R372.

Zehr, E.A., Kraemer, J.A., Erb, M.L., Coker, J.K., Montabana, E.A., Pogliano, J., and Agard, D.A. (2014). The structure and assembly mechanism of a novel three-stranded tubulin filament that centers phage DNA. Structure *22*, 539–548.

Zehr, E.A., Rohu, A., Liu, Y., Verba, K.A., Pogliano, J., Grigorieff, N., and Agard, D.A. (2018). Mechanistic Origins of Dynamic Instability in Filaments from the Phage Tubulin, PhuZ. bioRxiv. https://doi.org/10.1101/311498.

Zhang, R., Alushin, G.M., Brown, A., and Nogales, E. (2015). Mechanistic Origin of Microtubule Dynamic Instability and Its Modulation by EB Proteins. Cell *162*, 849–859.

STAR★METHODS

KEY RESOURCES TABLE

REAGENT or RESOURCE	SOURCE	IDENTIFIER
Bacterial and Virus Strains		
NEB 5-alpha Competent E. coli	New England Biolabs	Cat#C2987H
Pseudomonas aeruginosa (PAO1)	Pogliano strain collection	N/A
Pseudomonas aeruginosa K2733	Keith Poole of Queen's University Kingston, ON, Canada	N/A
Pseudomonas chlororaphis 200-B	Drs. Julie Thomas and Steven Hardies of UT Health Sciences San Antonio	N/A
Pseudomonas aeruginosa phage PhiPA3	Dr. Marcy Erb	N/A
Pseudomonas chlororaphis phage 201phi2-1	Drs. Julie Thomas and Steven Hardies of UT Health Sciences San Antonio	N/A
Saccharomyces cerevisiae Y2H Gold	Clontech	Cat#630489
Saccharomyces cerevisiae Y187	Clontech	Cat#630489
See Table S1 for a complete list of strains used in this paper		N/A
Chemicals, Peptides, and Recombinant Proteins		
FM 4-64	Thermo Fisher Scientific	Cat#T13320
DAPI (4',6-Diamidino-2-Phenylindole, Dihydrochloride)	Thermo Fisher Scientific	Cat#D1306
Ticarcillin disodium salt	Sigma-Aldrich	Cat#T5639
Gentamycin sulfate	Sigma-Aldrich	Cat#G1914
Phusion High-Fidelity DNA Polymerase	New England Biolabs	Cat#M0530L
Deoxynucleotide (dNTP) Solution Mix	New England Biolabs	Cat#N0447L
NEBuilder HiFi DNA Assembly Cloning Kit	New England Biolabs	Cat#E5520S
T4 DNA ligase	New England Biolabs	Cat#M0202L
Nucleospin plasmid extraction kit	Macherey-Nagel	Cat#740588
NucleoSpin Gel and PCR Clean-up	Macherey-Nagel	Cat#740609
Matchmaker Gold Yeast Two-Hybrid System	Clontech	Cat#630489
Oligonucleotides		
See Table S2 for a complete list of oligonucleotides used in this paper		N/A
Recombinant DNA		
pHERD30T plasmid	Dr. Hongwei D Yu of Marshall University	N/A
See Tables S3 and S4		N/A
Software and Algorithms		
DeltaVision SoftWoRx 6.5.2	GE HealthCare	http://incelldownload.gehealthcare.com/bin/download_data/SoftWoRx/7.0.0/SoftWoRx.htm
FIJI/ImageJ	NIH	https://imagej.nih.gov/ij/
CellProfiler 2.0	Lamprecht et al., 2007	cellprofiler.org
Amira	Commercial software by Thermo Scientific (formerly FEI)	https://www.fei.com/software/amira-3d-for-life-sciences/; RRID:SCR_014305
TomoSegMemTV	Martinez-Sanchez et al., 2014	https://sites.google.com/site/3demimageprocessing/tomosegmemtv
IMOD	Kremer et al., 1996	http://bio3d.colorado.edu/imod/; RRID:SCR_003297
Microsoft Excel	Microsoft Office	https://products.office.com/en-us/excel
Adobe Photoshop	Adobe	https://www.adobe.com/products/photoshop.html
Adobe Illustrator	Adobe	https://www.adobe.com/products/illustrator.html
Adobe Acrobat	Adobe	https://www.adobe.com/products/acrobat.html

CONTACT FOR REAGENT AND RESOURCE SHARING

Further information and requests for resources and reagents should be directed to and will be fulfilled by the Lead Contact, Joe Pogliano (jpogliano@ucsd.edu).

EXPERIMENTAL MODEL AND SUBJECT DETAILS

Strain, growth condition, and bacteriophage preparation

Bacterial strains used in this study are listed in Key Resource Table and Table S1. To amplify the strain, *Pseudomonas chlororaphis* strain 200-B was grown on Hard Agar (HA) containing 10 g Bacto-Tryptone, 5 g NaCl, and 10 g agar in 1L ddH_2O and incubated at 30°C overnight. *Pseudomonas aeruginosa* strains PA01 and PA01-K2733 (pump-knockout strain) were grown on Luria-Bertani (LB) media containing 10g Bacto-Tryptone, 5g NaCl, 5g Bacto-yeast extract in 1L ddH_2O and incubated at 30°C overnight. Lysates for phages 201Φ2-1 and ΦPA3 were made by infecting respective saturated host cultures with 10μl of high titer lysate, incubating for 15 minutes at room temperature, mixing with HA top agar (0.35%; phage 201Φ2-1) or LB top agar (0.35%; phage ΦPA3) and pouring over corresponding HA or LB plates. Plates were incubated at 30°C overnight. Plates that formed web-lysis were then flooded with 5mL of phage buffer and incubated at room temperature for 5 hours. The phage lysates were then aspirated, clarified by centrifugation at 15,000 rpm for 10 minutes, and stored at 4°C with 0.01% chloroform by volume.

Plasmid constructions and bacterial transformation

Fluorescent-tagged phage proteins were constructed into the pHERD 30T vector backbone using oligonucleotides as listed in Table S2. Phage genes were directly amplified from high-titer lysates of phages 201Φ2-1 or ΦPA3 using PCR amplification. Amplicons and vector backbones were then ligated together to generate phage gene-containing plasmids via isothermal assembly, immediately followed by transformation into *E. coli* DH5α plated on LB supplemented with gentamycin sulfate (15μg/mL). See also Table S4 for more detail on plasmid construction. Constructs were confirmed with sequencing and subsequently electroporated into either *P. chlororaphis* strain 200-B or *P. aeruginosa* strains PA01 and/or PA01-K2733. *P. chlororaphis* strain was grown on HA supplemented with gentamycin sulfate (25μg/mL) and *P. aeruginosa* strains PA01 and PA01-K2733 were grown on LB supplemented with gentamycin sulfate either at 300 μg/mL or 15μg/mL, respectively. See Tables S1 and S3 for a list of plasmids and strains.

METHOD DETAILS

Single cell-infection assay

The bacterial cells were grown on 1.2% agarose pads, supplemented with desired arabinose to induce fluorescent-tagged protein expression to label wild-type proteins from phage. The cells were then incubated at 30°C for 3 hours without a coverslip in a humid chamber. 5 μl of high-titer lysate (10^{10} pfu/ml) was added to the corresponding host cells on agarose pads to begin the phage infection, and then the cells were further incubated to allow phage infections occur. For ticarcillin treated experiments, 10μl of 50mg/ml TIC stock was added to cells 1.5 hours post inoculation on agarose pads and infection was performed thereafter as mentioned above. At desired time points after phage infection, a coverslip was put on the slide and fluorescent microscopy was then initiated. Data of static images and time-lapse imaging were collected and processed as described below.

Fixed and live cell static-image fluorescence microscopy

The fixed cell imaging protocol was adopted from "Fixed Cell Imaging" methodology in Chaikeeratisak et al., 2017. The DeltaVision Spectris Deconvolution microscope (Applied Precision, Issaquah, WA, USA) was used to visualize the fixed and live cells. For static images, the cells were imaged at 8 stacks in the Z-axis from the focal plane with 0.15 μm increments. Images were further processed by the deconvolution algorithm in DeltaVision SoftWoRx Image Analysis Program. Further image analysis and processing was performed in Fiji.

Time-lapse fluorescence microscopy

For time-lapse imaging, the cells were prepared and infected as indicated above. Cells were imaged from a single stack at the focal plane for desired length of time at selected intervals using Ultimate Focusing mode. Timelapse images were later deconvolved and analyzed as stated above.

3D-Structured Illumination Microscopy

Pseudomonas cells were grown, infected, and fixed as indicated above. Cells were stained with 1 μg/mL DAPI and then imaged using an Applied Precision/GE OMX V2.2 Microscope. Microscopic raw data were sequentially taken by SI-super-resolution light path to collect 3 mm thickness of samples with 125 nm increments in the z-axis with compatible immersion oils (Applied Precision). 3D-structured illumination microscopy (SIM) images were then rendered by standard OMX SI reconstruction parameters in DeltaVision SoftWoRx Image Analysis Program.

Fluorescence Recovery After Photobleaching

For time-lapse imaging, the cells were prepared and infected as indicated above. Filaments were photobleached using a laser (QLM module, API) for 0.05 sec at 31.3% power and then followed with time lapse imaging – images taken every 2 seconds for 1 minute with the Applied Precision/GE OMX V2.2 Microscope. Images were deconvolved with DeltaVision SoftWoRx.

Yeast Two-hybrid assay

Interaction between the proteins of interest was investigated using the Yeastmaker Yeast Transformation System 2. Partial gene and full-length gene were cloned into the bait (pGBKT7) and prey (pGADT7) vector (Clontech), as described in Table S1. The resulting recombinant constructs were transformed into the yeast *Saccharomyces cerevisiae* strain Gold and Y187 (Clontech) using the Yeastmaker™ Yeast Transformation System 2 (Clontech). Both yeast colonies containing the protein of interest were paired in a single 1.5mL centrifuge tube containing 500μL of 2X YPDA and vortexed to mix. Colonies were incubated shaking at 200 rpm at 30°C overnight. The mated cultures were plated on selective agar plates DDO and QDO/X/A to investigate the positive interaction. All constructs were tested for toxicity and autoactivation prior to the experiments. Y2HGold containing pGBKT7-53 with Y187 containing pGADT7-T was used as the positive control and Y2HGold containing pGBKT7-Lam with Y187 containing pGADT7-T was used as the negative control.

Tomography Sample Preparation and Data Acquisition

Infection of *P. aeruginosa* cells with phage ΦPA3 was done as indicated above. At 70 mpi, cells were scraped off from the surface of the pad using ¼ LB media. 7 μl of cells were deposited on holey carbon coated QUANTIFOIL® R 2/1 copper grids that were glow discharged using Pelco easiGlow™ glow discharge cleaning system. Manual blotting from the side of the grid opposite to the cells using Whatman No. 1 filter paper removed excess liquid such that cells form a monolayer on the surface of the grid. Cells were then plunge-frozen in a mixture of ethane/propane using a custom-built vitrification device (Max Planck Institute for Biochemistry, Munich).

Grids were then mounted into modified FEI Autogrids™ to avoid any mechanical damage to the delicate grids during subsequent transfer steps. Then, these clipped grids were transferred into Scios (Thermo Fisher Scientific, formerly FEI), a dual-beam (cryo-FIB/SEM) microscope equipped with a cryogenic stage. Thin sections of 100-250 nm, or lamellae, were prepared as previously described in Chaikeeratisak et al., 2017 containing 10-12 cells each.

Tilt-series were collected from typically -65° to +65° with 1.5° or 2° tilt increments using SerialEM[4] in a 300-keV Tecnai G2 Polara microscope (FEI) equipped with post-column Quantum Energy Filter (Gatan) and a K2 Summit 4k x 4k direct detector camera (Gatan). Images were recorded at a nominal magnification of 34,000 with a pixel size of 0.61 nm. The dose rate was set to 10-12 e/physical pixel at the camera level. Frame exposure was set to 0.1 seconds, with a total exposure in a frame set to be determined by an algorithm targeting an average count number. The total dose in a tomogram was typically ~100-120 e/A^2 with a defocus of -5 μm. The dataset for this study consists of 16 tomograms from 7 FIB-milled lamellas. Reconstruction of tilt-series was done in IMOD (Kremer et al., 1996) using patch tracking method. Semi-automatic segmentation of the membranes was done using TomoSegMemTV (Martinez-Sanchez et al., 2014), an open-source software based on tensor voting, followed by manual segmentation with Amira software (FEI Visualization Sciences Group). Filaments were traced manually using Amira as well.

QUANTIFICATION AND STATISTICAL ANALYSIS

To visualize the consensus location of gp200 (capsids), 32 single cell images from each experiment, wild type and mutant, were aligned and stacked using FIJI image analysis program (Schindelin et al., 2012). Then, the average GFP signals of all images in the stack were projected onto a single image. To visualize gp200 distribution of each cell, the GFP signal from each single cell image was combined in to a 1-pixel line and stacked. Performing on 8-bit GFP channel images, the location of gp200 from mid-cell was automatically measured by CellProfiler 2.0 image analysis program (Lamprecht et al., 2007) and normalized by cell length. Locations of bleach spots and capsids were measured from microscopy images in FIJI and plotted as distance over time in Microsoft Excel.

Analyses of the number of cells or phage particles were done from at least 3 independent biological experiments. Data represent as mean values or mean ±SEM. Pairwise comparison between the data were performed using Student's t test for unpaired data with unequal variance. (A p value less than 0.05 indicates a significant difference) All statistical analysis, data processing, and data presentation were conducted using KaleidaGraph and Microsoft Excel.

Accepted manuscript ฉบับที่ 3 (งานวิจัยเสริม)

วารสาร Antimicrobial Agents and Chemotherapy (AAC) ซึ่งเป็นวารสารที่อยู่ใน Quartile in Category Q1 และมี Impact Factor 4.256

Htoo, H.H., Brumage, L., Chaikeeratisak, V., Tsunemoto, H., Sugie, J., Tribuddharat, C., Pogliano, J., and Nonejuie, P. (2019). Bacterial Cytological Profiling as a Tool To Study Mechanisms of Action of Antibiotics That Are Active against Acinetobacter baumannii. Antimicrobial agents and chemotherapy 63 (4), e02310-18

AMERICAN SOCIETY FOR MICROBIOLOGY | Antimicrobial Agents and Chemotherapy®

Bacterial Cytological Profiling as a Tool To Study Mechanisms of Action of Antibiotics That Are Active against *Acinetobacter baumannii*

Htut Htut Htoo,[a] Lauren Brumage,[b] Vorrapon Chaikeeratisak,[c] Hannah Tsunemoto,[b] Joseph Sugie,[b] Chanwit Tribuddharat,[d] Joe Pogliano,[b] Poochit Nonejuie[a]

[a]Institute of Molecular Biosciences, Mahidol University, Salaya, Nakhon Pathom, Thailand
[b]Division of Biological Sciences, University of California, San Diego, La Jolla, California, USA
[c]Department of Biochemistry, Faculty of Science, Chulalongkorn University, Bangkok, Thailand
[d]Department of Microbiology, Faculty of Medicine Siriraj Hospital, Mahidol University, Bangkok, Thailand

ABSTRACT An increasing number of multidrug-resistant *Acinetobacter baumannii* (MDR-*AB*) infections have been reported worldwide, posing a threat to public health. The establishment of methods to elucidate the mechanism of action (MOA) of *A. baumannii*-specific antibiotics is needed to develop novel antimicrobial therapeutics with activity against MDR-*AB*. We previously developed bacterial cytological profiling (BCP) to understand the MOA of compounds in *Escherichia coli* and *Bacillus subtilis*. Given how distantly related *A. baumannii* is to these species, it was unclear to what extent it could be applied. Here, we implemented BCP as an antibiotic MOA discovery platform for *A. baumannii*. We found that the BCP platform can distinguish among six major antibiotic classes and can also subclassify antibiotics that inhibit the same cellular pathway but have different molecular targets. We used BCP to show that the compound NSC145612 inhibits the growth of *A. baumannii* via targeting RNA transcription. We confirmed this result by isolating and characterizing resistant mutants with mutations in the *rpoB* gene. Altogether, we conclude that BCP provides a useful tool for MOA studies of antibacterial compounds that are active against *A. baumannii*.

KEYWORDS *Acinetobacter baumannii*, antibiotic screening, mechanisms of action

The discovery of penicillin led to the "golden era" of antibiotic research which lasted for many decades before fading away in the 1970s. Since then, the rate of discovery of novel antibacterial molecules has decreased dramatically, and most of the newly commercialized antibiotics are analogues of existing ones (1–3). Although five new classes of antibiotics acting on Gram-positive bacteria were recently discovered, fewer novel antibiotics against Gram-negative bacteria have been developed (4). The incidence of Gram-negative pathogens that are resistant to almost all existing antibiotics is growing rapidly (5, 6). As a result, the options for treating drug-resistant Gram-negative infections are limited; thus, new antibiotics that act against Gram-negative bacteria are urgently needed (7). Among the *Enterococcus faecium*, *Staphylococcus aureus*, *Klebsiella pneumoniae*, *Acinetobacter baumannii*, *Pseudomonas aeruginosa*, and *Enterobacter* species (ESKAPE) pathogens (5), *A. baumannii* is of particular concern as it is (8, 9) responsible for a wide range of hospital-acquired infections, including meningitis, bacteremia, and skin infections (10). Apart from their intrinsic resistance, some clinically isolated *A. baumannii* strains have developed resistance to antibiotics commonly used for treatment, such as β-lactams, aminoglycosides, and tetracyclines (11). Also, a number of cases have been reported of strains that are resistant to colistin

Citation Htoo HH, Brumage L, Chaikeeratisak V, Tsunemoto H, Sugie J, Tribuddharat C, Pogliano J, Nonejuie P. 2019. Bacterial cytological profiling as a tool to study mechanisms of action of antibiotics that are active against *Acinetobacter baumannii*. Antimicrob Agents Chemother 63:e02310-18. https://doi.org/10.1128/AAC.02310-18.

Address correspondence to Poochit Nonejuie, poochit.non@mahidol.edu.

Received 15 November 2018
Returned for modification 6 December 2018
Accepted 30 January 2019
Accepted manuscript posted online 11 February 2019
Published 27 March 2019

(11–13) and tigecycline (11, 14, 15), antibiotics considered to be the last line of defense (16), emphasizing the need for novel antibiotics that are active against the pathogen.

In order to minimize the harmful effects of antibiotics on the microbiome and prevent the spread of antibiotic resistance across various pathogens, narrow spectrum antibiotics may be preferable over broad spectrum ones in some cases (2). Species-specific antibiotic screening platforms have been proposed as a potential approach to discover narrow spectrum antibiotics (17). A mycobacterium-specific screening platform is an example of a successful case of such screening approaches (4, 18). These screens resulted in the discovery of many antibiotics exhibiting both broad spectrum, such as streptomycin (19), and mycobacterium-specific activity, including isoniazid, pyrazinamide, ethionamide, ethambutol (4), and bedaquiline (20). Recently, Gram-specific (21–24) and pathogen-specific (25, 26) antibiotic discovery were also proven to be successful, leading to the identification of narrow spectrum compounds, including some that are active only against *A. baumannii* (27–29). As more candidate compounds are revealed through screening, there will be a need for better methods to elucidate their mechanism of action (MOA) in *A. baumannii*.

In recent years, we have developed a method for antibiotic mechanism of action (MOA) study called bacterial cytological profiling (BCP) that can be applied to various bacterial species (30–32). BCP generates reference cytological profiles of bacterial cells upon treatment with different classes of antibiotics. BCP has been proven to be beneficial in MOA studies of antibiotics (30, 31, 33–37) and in a rapid antibiotic susceptibility test (32). Although a BCP-derived method was successfully used in a synergy study between azithromycin and human antimicrobial peptide LL-37 against multidrug-resistant *A. baumannii* (MDR-*AB*) (38), reference BCP profiles of *A. baumannii* treated with various types of antibiotics have not been reported. *A. baumannii* is very distantly related to *Escherichia coli*, and it was, therefore, unclear to what extent BCP could be applied. Here, we investigated the utility of BCP for *A. baumannii*. We showed that BCP is a useful tool for identifying the MOA of antibacterial molecules that inhibit the growth of *A. baumannii* (see Table S1 in the supplemental material) and used this platform to determine that the compound NSC145612 inhibits transcription in *A. baumannii*.

RESULTS

BCP in *A. baumannii* can distinguish different classes of antibiotics. We first determined, based on cell morphological changes in *A. baumannii* ATCC 19606, if BCP can distinguish between antibiotics that interfere with six major cellular pathways, namely, protein translation (chloramphenicol), RNA transcription (rifampin), membrane integrity (colistin), lipid synthesis (triclosan), cell wall synthesis (piperacillin), and DNA replication (Ciprofloxacin). After *A. baumannii* ATCC 19606 was incubated with antibiotics, we found unique cell cytological profiles depending on the class of antibiotics used for treatment (Fig. 1A to F). Chloramphenicol-treated cells had a signature toroidal-shaped chromosome (Fig. 1B), while treatment with the transcription inhibitor rifampin resulted in diffuse 4′,6-diamidino-2-phenylindole (DAPI) staining throughout the cell except for a small rounded region near the cell membrane (Fig. 1C) similar to the BCP profile of actinomycin D-treated *E. coli* from the previous study (30). Colistin-treated cells were attached together, creating a long chain of small and round cells (Fig. 1D) similar to what we previously reported (38). Triclosan-treated cells were shorter and slightly rounder than untreated cells (Fig. 1E). The cell wall synthesis inhibitor piperacillin resulted in cell elongation without visible cell septation (Fig. 1F). In the case of DNA replication inhibitors, we found that even though DNA replication inhibitors effectively inhibited growth of *A. baumannii* ATCC 19606 as measured by MIC, only less than 10% of the cells treated with these inhibitors showed a possible DNA replication inhibition phenotype in this strain (Fig. S1). Thus, another well-studied *A. baumannii* strain, ATCC 17978 (39), was used in a DNA replication experiment (see Fig. S2 and Table S1 in the supplemental material). We found that the cell morphology of *A. baumannii* ATCC 17978 changed upon ciprofloxacin treatment. The treated cells were

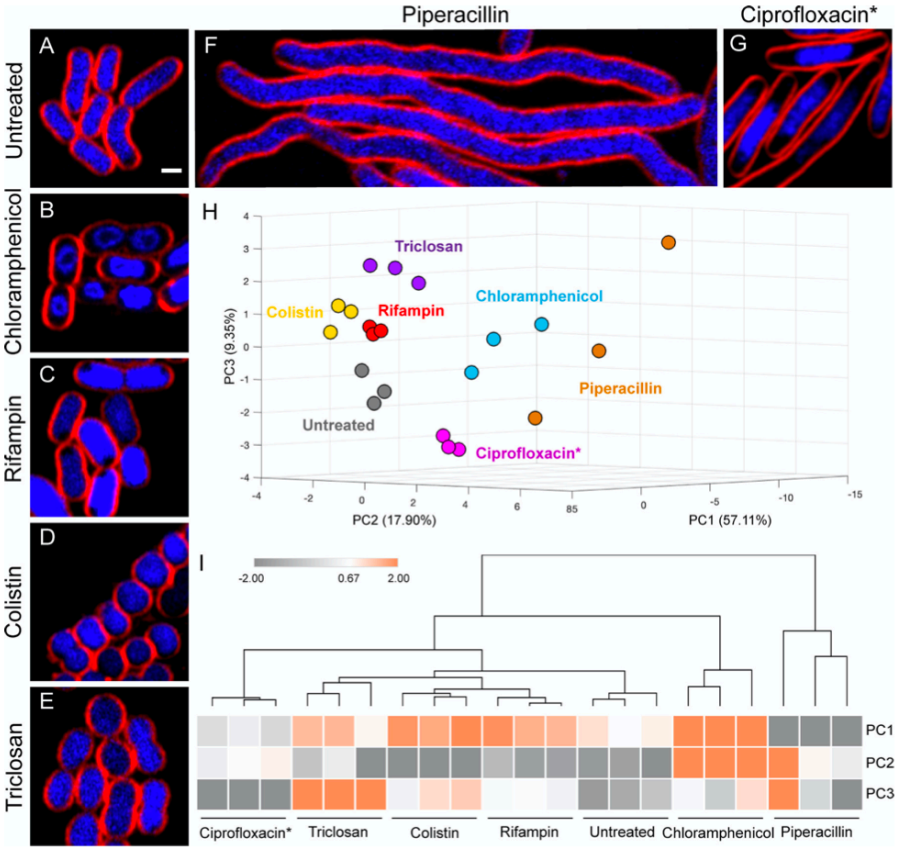

FIG 1 *A. baumannii* cells treated with antibiotics targeting different cellular pathways show distinct morphological changes. (A) Untreated bacterial cells. Bacterial cells were treated with 5× MIC (B, D to F) and 2× MIC (C and G) of each antibiotic for 2 hours and then stained with FM 4-64 (red) and DAPI (blue). Scale bar represents 1 μm. (H) A three-dimensional (3D) PCA graph constructed from PC1 (57.11%), PC2 (17.90%), and PC3 (9.35%) shows antibiotics that are distinguished into different subgroups as coded by colors. Three independent experiments were performed for each antibiotic treatment and cytological parameters (Table S2) measured as described in Materials and Methods. (I) Euclidean cluster map of antibiotics, using values from PC1, PC2, and PC3 of PCA. Ciprofloxacin* indicates that all data for treatment with ciprofloxacin were obtained in *A. baumannii* ATCC 17978 strain.

elongated and their chromosomes formed a single large nucleoid in the cell center (Fig. 1G). Overall, *A. baumannii* cytological profiles of cells treated with different antibiotics were similar to those of *E. coli* shown in our previous study (30). Next, we quantitated 36 different cytological parameters of cells treated with each antibiotic (see Table S2 in the supplemental material) and used principal-component analysis (PCA) to determine if these cell profiles can be used to quantitatively classify the MOAs. The results showed that antibiotics with different MOAs were distinguishable from each other (Fig. 1H) and replicates of each antibiotic treatment were clustered together (Fig. 1I). These results suggest that BCP can be applied to *A. baumannii* in discriminating antibiotics targeting six major cellular pathways, including protein translation, RNA transcription, membrane integrity, lipid synthesis, cell wall synthesis, and DNA replication.

In *A. baumannii*, BCP can subclassify different antibiotics that inhibit the same cellular pathway based on their mechanism of action. Our previous study in *E. coli* also showed that BCP can be used to classify subgroups of antibiotics based on their

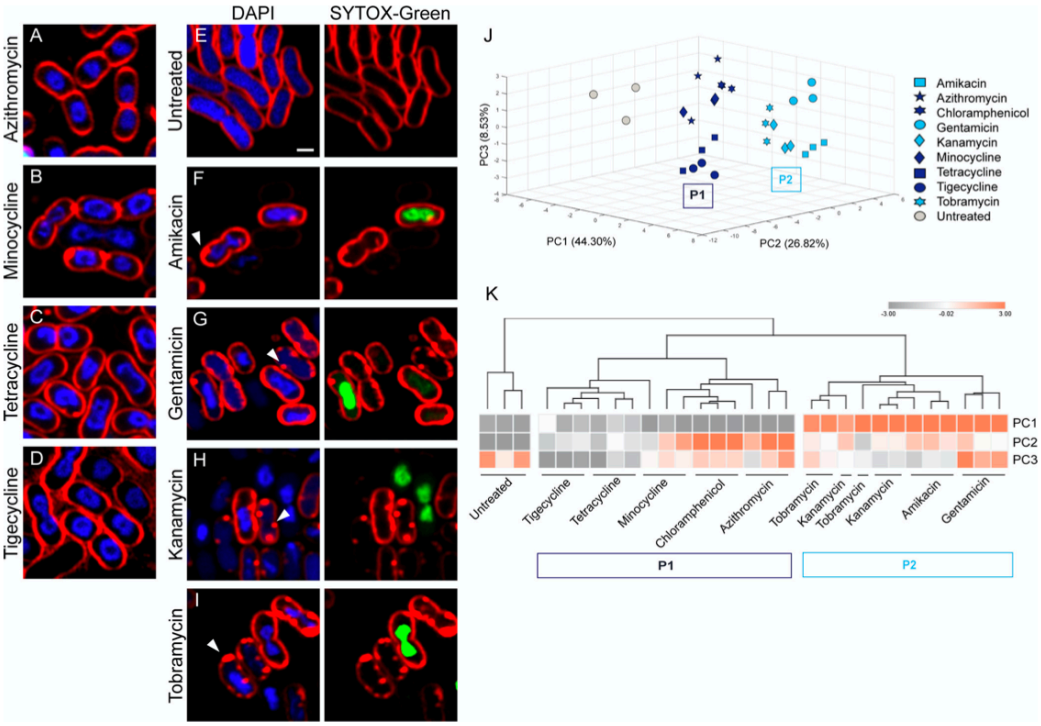

FIG 2 *A. baumannii* cytological profiling differentiating protein translation inhibitors into subgroups by their MOA. Bacterial cells were treated with each antibiotic at 5× MIC for 2 hours and then stained with FM 4-64 (red), DAPI (blue), and Sytox green (green). Scale bar represents 1 μm. (A to D) Cells treated with protein translation inhibitors (P1 group) show distinct cell profiles. (E) Untreated cells. (F to I) Cells treated with aminoglycosides (P2 group) showing altered membrane permeability. Arrows indicate membrane pooling. Sytox green (*Right* panels) only stains nucleoids in the cells with permeabilized membranes. PCA graph of protein translation inhibitors using PC1 (44.30%), PC2 (26.82%), and PC3 (8.53%) (J) and Euclidean cluster map, using PC1, PC2, and PC3 from PCA (K).

MOA (30). To test if the ability of subclassification by BCP is also observed in *A. baumannii*, we investigated whether BCP can differentiate various protein translation inhibitors and cell wall synthesis inhibitors. From all protein translation inhibitors tested (Fig. 2A to I), we found that they were classified into 2 groups that correlated with their known MOA, similar to the previous study in *E. coli* (30), namely, translation inhibition (P1) and aminoglycosides (P2) (Fig. 2J and K). Tetracycline, tigecycline, and minocycline, which are structurally related, were closely clustered in the analysis (Fig. 2K). Protein translation inhibitors belonging to the P1 group bind directly to the ribosome to inhibit translation (40–43), resulting in the formation of toroidal-shaped DNA (Fig. 1B and Fig. 2B to D). In addition to the translation inhibition, aminoglycosides (44) displayed a significant effect on *A. baumannii* membrane permeability, as indicated by the increase in Sytox green uptake (Fig. 2F to I, right panel) whereas Sytox green signal was not detected in the untreated cells (Fig. 2E, right panel). The increase in Sytox green intensity found in aminoglycoside-treated cells is more than 20 times higher than those of untreated cells (Table S2). This permeability effect of aminoglycosides separated them from the untreated and the others in the P1 group (Fig. 2J and K). We also found that BCP could distinguish between two types of penicillin binding protein (PBP) inhibitors in *A. baumannii* (Fig. 3), as expected (45, 46). Among all cell wall synthesis inhibitors tested in this study (Table S1), only meropenem, a preferred choice for treating *A. baumannii* infections (10, 47–49), and piperacillin are active against the

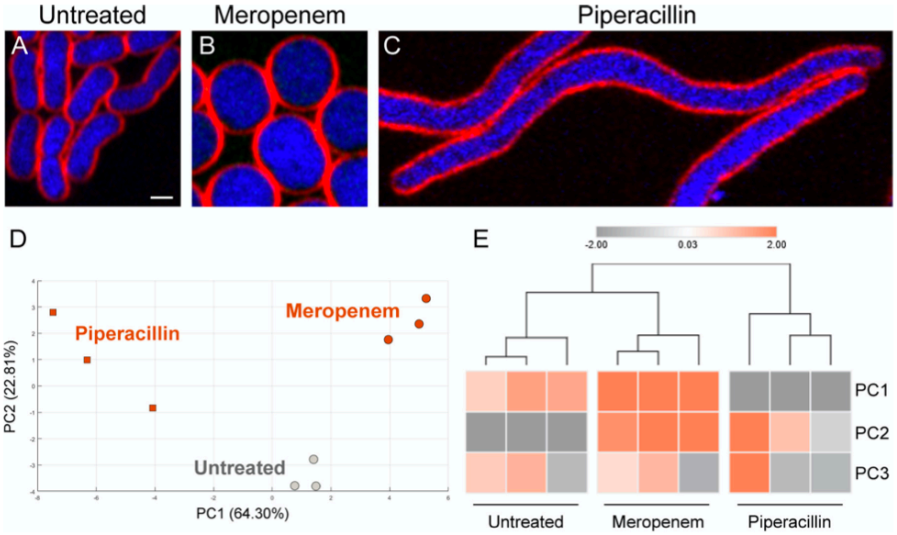

FIG 3 Cytological profiling of cell wall synthesis inhibitors; meropenem-treated cells showing different profiles to the cells treated with piperacillin. (A to C) Bacterial cells were treated with antibiotics at 5× MIC for 2 hours and then stained with FM 4-64 (red) and DAPI (blue). Scale bar represents 1 μm. PCA graph of cell wall synthesis inhibitors showing only PC1 (64.30%) and PC2 (22.81%) (D) and Euclidean cluster map using PC1, PC2, and PC3 from PCA showing distinct morphological clusters (E).

strain according to the MIC assay. Meropenem-treated *A. baumannii* cells were round and bloated compared with control cells, in agreement with its affinity toward PBP2 (50) (Fig. 3A and B). Cells treated with piperacillin were elongated with an average length of 12 μm (Fig. 3C and Table S2), likely due to the affinity of piperacillin toward PBP3 (49), which is required for cell septa formation in *A. baumannii*. Altogether, these results suggest that BCP in *A. baumannii* can also subclassify antibiotics based on their MOA (Fig. 2 and 3), similar to what we previously reported in *E. coli* (30).

The compound NSC145612 inhibits the growth of *A. baumannii* via RNA transcription inhibition. In this study, we have tested 64 compounds from National Cancer Institute's Developmental Therapeutics Program library for their antibacterial activities against Gram-negative bacterium *E. coli* ATCC 25922 and found that 17 compounds were active. Among those Gram-negative active compounds, the compound NSC145612 (Fig. 4A, right panel) showed a promising MIC against *A. baumannii* ATCC 19606 at 25 μM (Table S1). Although the chemical scaffold of NSC145612 is closely related to rifampin (51), which is an antibiotic inhibiting DNA-dependent RNA polymerase (52), the compound has never been tested for its mechanism of action. In order to investigate if the compound exhibits the same MOA as rifampin, we performed BCP on the compound against *A. baumannii*. As expected, the result showed that NSC145612-treated *A. baumannii* cells exhibited a cytological profile identical to rifampin-treated cells (Fig. 4B to D) and grouped together in PCA analysis (Fig. 4E and F), suggesting that NSC145612 inhibits RNA transcription of *A. baumannii*, similar to rifampin. This conclusion was supported by examining NSC145612 in *E. coli* Δ*tolC*, whose growth was inhibited at 30 μM (see Table S3 in the supplemental material). BCP of NSC145612-treated *E. coli* Δ*tolC* cells showed decondensed DNA (see Fig. S3 in the supplemental material), which is a hallmark of transcription inhibition in *E. coli* (30).

In order to gain more information regarding the molecular target of the compound NSC145612, we isolated and characterized resistant mutations in both *A. baumannii and E. coli* Δ*tolC*. A total of four NSC145612-resistant mutants of *E. coli* were isolated (Table S3). Whole-genome sequencing of the resistant mutants revealed various mu-

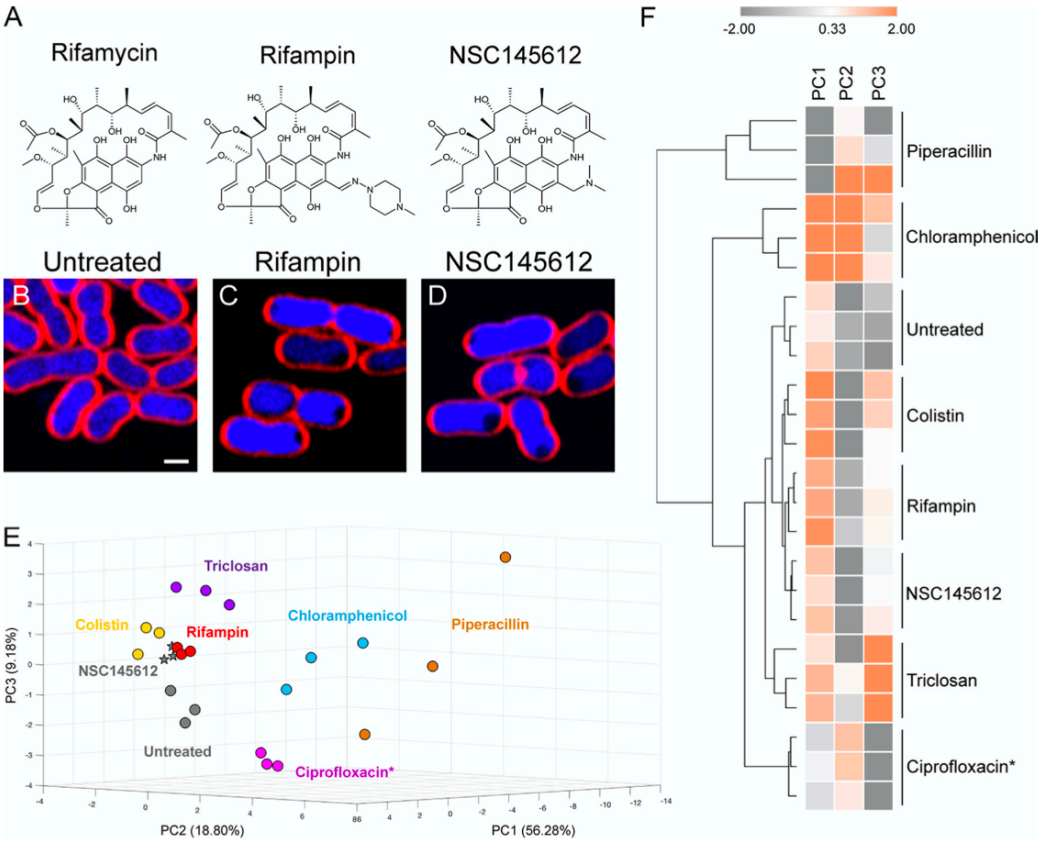

FIG 4 *A. baumannii* cell treated with NSC145612 show similar profiles to the RNA transcription inhibitor rifampin. (A) Chemical structure of rifamycin, rifampin, and NSC145612. (B) Untreated cells. Bacterial cells were treated with 2× MIC of rifampin (C) or NSC145612 (D) for 2 hours and then stained with FM 4-64 (red) and DAPI (blue). Scale bar represents 1 μm. PCA graph of 6 major classes of representative antibiotics and NSC145612 using PC1 (56.28%), PC2 (18.80%), and PC3 (9.18%) (E) and Euclidean cluster map, using values from PC1, PC2, and PC3 from PCA, showing NSC145612 closely clustered to rifampin (F). Ciprofloxacin* indicates that all data for treatment with Ciprofloxacin was obtained in *A. baumannii* ATCC 17978 strain.

tations in DNA-dependent RNA polymerase subunit B (*rpoB* gene) (Table S3), a well-known gene responsible for rifampin resistance in *E. coli* and *Mycobacterium tuberculosis* (52, 53). Notably, three of our four resistant mutants contain mutations (Table S3) which are located in the rifampin resistance-determining region (RRDR) of the *rpoB* gene spanning from codon 507 to 533 (54). The rare mutation *rpoB*(*V146F*), which is located near the rifampin-binding pocket of the enzyme (55), was also found in one of the NSC145612-resistant mutants (LB143 strain). In accordance with the genetic profiles, the BCP profile of resistant mutants treated with NSC145612 and rifampin showed no cytological changes compared with the untreated controls (Fig. S3), confirming that NSC145612 and rifampin are inactive against the strains containing the *rpoB* mutation.

To confirm the molecular target of NSC145612 in *A. baumannii*, two NSC145612-resistant *A. baumannii* strains were also isolated with MIC above 200 μM (Table 1). As expected, NSC145612-resistant *A. baumannii* contained a mutation in the *rpoB* gene, *rpoB*(*G543S*) (Table 1), which is located in the RRDR and is known to be responsible for rifampin resistance in *A. baumannii* (56, 57). BCP results showed that neither NSC145612 nor rifampin treatment resulted in cytological changes of NSC145612-resistant *A.*

TABLE 1 MIC of NSC145612 and rifampin against *A. baumannii* strains

Strain	*rpoB* mutation	MIC (μM) by compound:	
		NSC145612	Rifampin
A. baumannii		25	1.2
A. baumannii HH1102	*rpoB*(*G543S*)	>200	24
A. baumannii HH1105	*rpoB*(*G543S*)	>200	24

baumannii strains compared with the controls (Fig. 5), confirming that NSC145612 and rifampin are inactive against the resistant strains. Overall, these results suggest that NSC145612 inhibits RNA transcription of *A. baumannii* by targeting its RNA polymerase subunit B.

DISCUSSION

A recent report from the World Health Organization revealed that among the ESKAPE pathogens, *A. baumannii* poses a threat to public health and economies worldwide (9). *A. baumannii* is a successful pathogen due to its ability to survive in desiccated environments and its intrinsic antibiotic resistance (8). As a result, MDR-*AB* is spreading at an alarming rate (58–60). Multiple approaches exist in order to help mitigate the rise of MDR-*AB*, including developing more stringent guidelines for antibiotic usage and establishing effective surveillance and containment programs (9). A direct approach to combat MDR-*AB* is to find new antibiotics that are effective against this pathogen.

BCP has been developed for several species of bacteria, including *E. coli*, *S. aureus*, and *B. subtilis*, but it has not been systematically applied to *A. baumannii* (31, 32, 61). We studied the cytological profiles of antibiotics commonly used to treat *A. baumannii*. We show that BCP can be used to identify the MOA of newly discovered compounds to facilitate *A. baumannii*-specific antibiotic discovery. BCP successfully differentiates *A. baumannii* cells treated with different antibiotics targeting major cellular pathways, namely, protein translation, RNA transcription, membrane integrity, lipid synthesis, cell wall synthesis, and DNA replication. Similar to *E. coli*, *A. baumannii* cytological changes

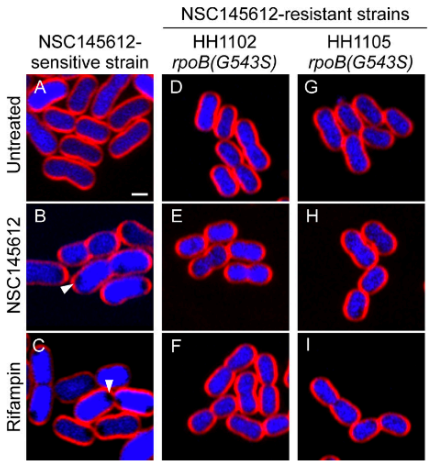

FIG 5 NSC145612-resistant *A. baumannii* cells show no morphological change upon NSC145612 and rifampin treatment. (A to C) NSC145612-sensitive strain. Arrows indicate signature phenotype of RNA transcription inhibition. (D to I) NSC145612-resistant strains with rpoB mutations indicated. Bacterial cells were treated with 2× MIC of NSC145612 (B, E, and H) or rifampin (C, F, and I) for 2 hours and then stained with FM 4-64 (red) and DAPI (blue). Scale bar represents 1 μm.

can reveal subgroups of protein translation inhibitors and cell wall synthesis inhibitors, suggesting similar cytological responses across Gram-negative bacterial species.

While *A. baumannii* ATCC 17978 treated with ciprofloxacin showed a clear cytological profile consistent with inhibiting DNA replication (Fig. S2), treatment of *A. baumannii* ATCC 19606 with ciprofloxacin did not induce similar cytological changes (Fig. S1). The fact that *A. baumannii* ATCC 19606 did not respond to DNA replication inhibitors made it unpractical for data from this strain to be used in the analysis. DNA damage and replication inhibition caused by quinolone antibiotics induce SOS responses in *E. coli* (62–64) and other bacteria (65, 66). In previous studies of *E. coli* (30, 67), filamentous *E. coli* observed after quinolone antibiotic treatment was a result of replication-halt-induced SOS response (65). Upon SOS response induction, *sulA* is derepressed due to the decrease in LexA protein, a master regulator of SOS response genes. SulA then inhibits FtsZ polymerization which leads to cell division inhibition and filamentation (68, 69). However, the SOS response of *Acinetobacter* spp. is not well understood due to the lack of similar SOS response genes, including *lexA* and *sulA* (68, 70–72). Since distinct responses to DNA damage have been observed in different species of *Acinetobacter* (73, 74), it is possible that *A. baumannii* ATCC 19606 and ATCC 17978 respond differently to the DNA replication inhibitors. Based on these results, multiple *A. baumannii* strains should be used to establish a comprehensive database of cytological profiles.

The compound NSC145612 from the National Cancer Institute's Developmental Therapeutics Program has previously been tested for anticancer and AIDS antiviral activity, all of which gave negative results (51). In this study, its antibacterial activity was tested by BCP and later confirmed by resistant mutant selection and genome sequencing. NSC145612 inhibits the growth of *A. baumannii* and *E. coli* via RNA transcription inhibition by targeting the RpoB protein. Altogether, this study proves the utility of BCP as a potential method to reveal the mechanism of action of compounds that are active against *A. baumannii*.

MATERIALS AND METHODS

Bacteria strains and growth and antibiotics. *Acinetobacter baumannii* strain ATCC 19606, strain ATCC 17978, and *Escherichia coli* strain AD3644 (Δ*tolC*) were used in this study. The bacteria were grown in LB medium or LB agar at 30°C. A total of 22 antibiotics were tested on *A. baumannii* from which 15 antibiotics with MIC of less than 112 μg/ml were used in this study (Table S1). The compound NSC145612 was obtained from the National Cancer Institute's Developmental Therapeutics Program. Preparation of the antibiotics was performed according to the manufacture's recommendations.

MICs. MICs of all antibiotics are shown in Table S1. MICs were determined using the microdilution method (30). Overnight cultures of *A. baumannii* were diluted 1:100 in LB broth and allowed to grow at 30°C on a roller until exponential phase or until an optical density at 600 (OD_{600}) of 0.2 was obtained. The bacterial culture was further diluted 1:100 into each well of a 96-well plate containing antibiotics in LB medium at appropriate concentrations. Cultures were allowed to grow at 30°C for 24 hours. MICs were determined by observing the concentration of the antibiotic in the well where the bacteria was unable to grow.

Fluorescence microscopy. Overnight cultures of *A. baumannii* were diluted 1:500 and those of *E. coli* at 1:100 in LB broth and grown at 30°C on a roller until exponential phase. Antibiotics were added at concentrations of 0.75 times MIC for colistin; 2 times the MIC for rifampin, NSC145612, and ciprofloxacin; and 5 times the MIC for the rest of the tested antibiotics. Cultures were then grown at 30°C on a roller for 2 hours. *A. baumannii* cultures were stained with FM 4-64 (2 μg/ml), DAPI (4 μg/ml), and Sytox green (0.5 μM). *E. coli* cells were stained with FM 4-64 (1 μg/ml), DAPI (2 μg/ml), and Sytox green (0.5 μM). Stained bacterial cultures were harvested by centrifugation at 6,000 $\times$ *g* for 30 seconds and resuspended in 1/10 volume of the same culture medium. Three microliters of this was added to agarose pads (1.2% agarose in 20% LB broth) on concave glass slides. Fluorescence microscopy was performed with consistent imaging parameters throughout all experiments.

Cytological profiling. Cytological profiles were determined by automated cell analysis using CellProfiler 3.0 (75). Briefly, images were preprocessed on Fiji software (76) and subsequently analyzed on CellProfiler 3.0 software. Cell morphological parameters, such as length, width, area, perimeter, form factor, ferret diameter, radius, compactness, solidity, and eccentricity, of both cell membrane and nucleoid were determined. To obtain the average intensity of Sytox green and DAPI, both the membrane and nucleoid outlines were used and subtracted by background intensity in corresponding images. The fold increase in permeability of aminoglycosides (P2 group) was determined by dividing the Sytox green intensity of aminoglycoside-treated cells with that of the untreated cells (Table S2). Decondensation of the nucleoid was determined by the ratio of the area of the nucleoid to that of the cell membrane.

Statistical analysis. As described previously (30, 31, 38), the cytological parameters of each antibiotic were obtained from three independent experiments. Profiling data was from automated analysis of the cells in each imaging field. Only images containing more than 20 for long cells and for the rest, more than 30 cells per imaging field were selected into data points. Weighed principal-component analysis (PCA) was performed using statistic tools on MATLAB 2017a. Euclidean cluster analysis was generated from Morpheus (https://software.broadinstitute.org/morpheus).

Isolation of NSC145612-resistant mutants. In *E. coli*, resistant mutants were obtained by plating *E. coli* AD3644 (Δ*tolC*) onto LB agar plates containing 2× MIC of NSC145612. The plates were incubated at 30°C, and resistant mutants were purified and stabilized on additional 2× MIC of NSC145612 selection plates. In *A. baumannii*, *A. baumannii* ATCC 19606 culture was diluted into the LB medium containing NSC145612 starting at 0.5× MIC. This process was repeated with escalating concentrations of NSC145612 until the NSC145612-resistant *A. baumannii* was obtained. The resistant strains were purified on LB agar plates, and the MICs for NSC145612 and rifampin were determined by the broth dilution method, as mentioned above.

SUPPLEMENTAL MATERIAL

Supplemental material for this article may be found at https://doi.org/10.1128/AAC.02310-18.

SUPPLEMENTAL FILE 1, PDF file, 1.2 MB.

ACKNOWLEDGMENTS

This research was supported by the Thailand Research Fund and the Office of the Higher Education Commission (MRG6080081). V.C. was supported by MRG6180027 and Grants for Development of New Faculty Staff, Ratchadaphiseksomphot Endowment Fund.

We thank Naraporn Sirinonthanaweeh and Potchaman Sittipaisankul for fluorescence microscope services and thank Ittipat Meewan for providing chemical structures.

REFERENCES

1. Walsh CT, Wencewicz TA. 2014. Prospects for new antibiotics: a molecule-centered perspective. J Antibiot (Tokyo) 67:7–22. https://doi.org/10.1038/ja.2013.49.
2. Fischbach MA, Walsh CT. 2009. Antibiotics for emerging pathogens. Science 325:1089–1093. https://doi.org/10.1126/science.1176667.
3. Silver LL. 2011. Challenges of antibacterial discovery. Clin Microbiol Rev 24:71–109. https://doi.org/10.1128/CMR.00030-10.
4. Lewis K. 2013. Platforms for antibiotic discovery. Nat Rev Drug Discov 12:371–387. https://doi.org/10.1038/nrd3975.
5. Boucher HW, Talbot GH, Bradley JS, Edwards JE, Gilbert D, Rice LB, Scheld M, Spellberg B, Bartlett J. 2009. Bad bugs, no drugs: no ESKAPE! an update from the Infectious Diseases Society of America. Clin Infect Dis 48:1–12. https://doi.org/10.1086/595011.
6. Berdy J. 2012. Thoughts and facts about antibiotics: where we are now and where we are heading. J Antibiot 65:385–395. https://doi.org/10.1038/ja.2012.27.
7. Butler MS, Blaskovich MA, Cooper MA. 2013. Antibiotics in the clinical pipeline in 2013. J Antibiot (Tokyo) 66:571–591. https://doi.org/10.1038/ja.2013.86.
8. Peleg AY, Seifert H, Paterson DL. 2008. *Acinetobacter baumannii*: emergence of a successful pathogen. Clin Microbiol Rev 21:538–582. https://doi.org/10.1128/CMR.00058-07.
9. Tacconelli E, Carrara E, Savoldi A, Harbarth S, Mendelson M, Monnet DL, Pulcini C, Kahlmeter G, Kluytmans J, Carmeli Y, Ouellette M, Outterson K, Patel J, Cavaleri M, Cox EM, Houchens CR, Grayson ML, Hansen P, Singh N, Theuretzbacher U, Magrini N. 2018. Discovery, research, and development of new antibiotics: the WHO priority list of antibiotic-resistant bacteria and tuberculosis. Lancet Infect Dis 18:318–327. https://doi.org/10.1016/S1473-3099(17)30753-3.
10. Lee C-R, Lee JH, Park M, Park KS, Bae IK, Kim YB, Cha C-J, Jeong BC, Lee SH. 2017. Biology of *Acinetobacter baumannii*: pathogenesis, antibiotic resistance mechanisms, and prospective treatment options. Front Cell Infect Microbiol 7:55. https://doi.org/10.3389/fcimb.2017.00055.
11. Doi Y, Murray G, Peleg A. 2015. *Acinetobacter baumannii*: evolution of antimicrobial resistance—treatment options. Semin Respir Crit Care Med 36:085–098. https://doi.org/10.1055/s-0034-1398388.
12. Beceiro A, Moreno A, Fernandez N, Vallejo JA, Aranda J, Adler B, Harper M, Boyce JD, Bou G. 2014. Biological cost of different mechanisms of colistin resistance and their impact on virulence in *Acinetobacter baumannii*. Antimicrob Agents Chemother 58:518–526. https://doi.org/10.1128/AAC.01597-13.
13. Rolain J-M, Diene SM, Kempf M, Gimenez G, Robert C, Raoult D. 2013. Real-time sequencing to decipher the molecular mechanism of resistance of a clinical pan-drug-resistant *Acinetobacter baumannii* isolate from Marseille, France. Antimicrob Agents Chemother 57:592–596. https://doi.org/10.1128/AAC.01314-12.
14. Peleg AY, Potoski BA, Rea R, Adams J, Sethi J, Capitano B, Husain S, Kwak EJ, Bhat SV, Paterson DL. 2007. *Acinetobacter baumannii* bloodstream infection while receiving tigecycline: a cautionary report. J Antimicrob Chemother 59:128–131. https://doi.org/10.1093/jac/dkl441.
15. Ruzin A, Keeney D, Bradford PA. 2007. AdeABC multidrug efflux pump is associated with decreased susceptibility to tigecycline in *Acinetobacter calcoaceticus–Acinetobacter baumannii* complex. J Antimicrob Chemother 59:1001–1004. https://doi.org/10.1093/jac/dkm058.
16. Li J, Nation RL, Turnidge JD, Milne RW, Coulthard K, Rayner CR, Paterson DL. 2006. Colistin: the re-emerging antibiotic for multidrug-resistant Gram-negative bacterial infections. Lancet Infect Dis 6:589–601. https://doi.org/10.1016/S1473-3099(06)70580-1.
17. Waksman SA, Schatz A, Reynolds DM. 2010. Production of antibiotic substance by actinomycetes. Ann N Y Acad Sci 1213:112–124. https://doi.org/10.1111/j.1749-6632.2010.05861.x.
18. Sneader W. 2005. Drug discovery: a history. John Wiley & Sons Ltd. https://doi.org/10.1002/0470015535.
19. Schatz A, Bugle E, Waksman SA. 1944. Streptomycin, a substance exhibiting antibiotic activity against gram-positive and gram-negative bacteria. Proc Soc Exp Biol Med 55:66–69. https://doi.org/10.3181/00379727-55-14461.
20. Andries K, Verhasselt P, Guillemont J, Göhlmann HWH, Neefs J-M, Winkler H, Van GJ, Timmerman P, Zhu M, Lee E, Williams P, de CD, Huitric E, Hoffner S, Cambau E, Truffot PC, Lounis N, Jarlier V. 2005. A diarylquinoline drug active on the ATP synthase of *Mycobacterium tuberculosis*. Science 307:223–227. https://doi.org/10.1126/science.1106753.
21. Maxson T, Mitchell DA. 2016. Targeted treatment for bacterial infections: prospects for pathogen-specific antibiotics coupled with rapid diagnostics. Tetrahedron 72:3609–3624. https://doi.org/10.1016/j.tet.2015.09.069.
22. Swaney SM, Aoki H, Ganoza MC, Shinabarger DL. 1998. The oxazolidinone linezolid inhibits initiation of protein synthesis in bacteria. Antimi-

crob Agents Chemother 42:3251–3255. https://doi.org/10.1128/AAC.42.12.3251.
23. Brickner SJ, Hutchinson DK, Barbachyn MR, Manninen PR, Ulanowicz DA, Garmon SA, Grega KC, Hendges SK, Toops DS, Ford CW, Zurenko GE. 1996. Synthesis and antibacterial activity of U-100592 and U-100766, two oxazolidinone antibacterial agents for the potential treatment of multidrug-resistant gram-positive bacterial infections. J Med Chem 39:673–679. https://doi.org/10.1021/jm9509556.
24. Oleson FB, Jr, Baltz RH, Eisenstein BI. 2010. Daptomycin: from the mountain to the clinic, with essential help from Francis Tally, MD. Clin Infect Dis 50:S10–S15. https://doi.org/10.1086/647938.
25. Ackermann G, Löffler B, Adler D, Rodloff AC. 2004. In vitro activity of OPT-80 against *Clostridium difficile*. Antimicrob Agents Chemother 48:2280–2282. https://doi.org/10.1128/AAC.48.6.2280-2282.2004.
26. Melander RJ, Zurawski DV, Melander C. 2018. Narrow-spectrum antibacterial agents. MedChemComm 9:12–21. https://doi.org/10.1039/C7MD00528H.
27. Corey BW, Thompson MG, Hittle LE, Jacobs AC, Asafo-Adjei EA, Huggins WM, Melander RJ, Melander C, Ernst RK, Zurawski DV. 2017. 1,2,4-triazolidine-3-thiones have specific activity against *Acinetobacter baumannii* among common nosocomial pathogens. ACS Infect Dis 3:62–71. https://doi.org/10.1021/acsinfecdis.6b00133.
28. Lee J-Y, Jeong M-C, Jeon D, Lee Y, Lee WC, Kim Y. 2017. Structure-activity relationship-based screening of antibiotics against Gram-negative *Acinetobacter baumannii*. Bioorg Med Chem 25:372–380. https://doi.org/10.1016/j.bmc.2016.11.001.
29. Cheng Y-S, Sun W, Xu M, Shen M, Khraiwesh M, Sciotti RJ, Zheng W. 2018. Repurposing screen identifies unconventional drugs with activity against multidrug resistant *Acinetobacter baumannii*. Front Cell Infect Microbiol 8:438. https://doi.org/10.3389/fcimb.2018.00438.
30. Nonejuie P, Burkart M, Pogliano K, Pogliano J. 2013. Bacterial cytological profiling rapidly identifies the cellular pathways targeted by antibacterial molecules. Proc Natl Acad Sci U S A 110:16169–16174. https://doi.org/10.1073/pnas.1311066110.
31. Lamsa A, Lopez-Garrido J, Quach D, Riley EP, Pogliano J, Pogliano K. 2016. Rapid inhibition profiling in *Bacillus subtilis* to identify the mechanism of action of new antimicrobials. ACS Chem Biol 11:2222–2231. https://doi.org/10.1021/acschembio.5b01050.
32. Quach DT, Sakoulas G, Nizet V, Pogliano J, Pogliano K. 2016. Bacterial cytological profiling (BCP) as a rapid and accurate antimicrobial susceptibility testing method for *Staphylococcus aureus*. EBioMedicine 4:95–103. https://doi.org/10.1016/j.ebiom.2016.01.020.
33. Alpha CJ, Campos M, Jacobs-Wagner C, Strobel SA. 2015. Mycofumigation by the volatile organic compound-producing fungus Muscodor albus induces bacterial cell death through DNA damage. Appl Environ Microbiol 81:1147–1156. https://doi.org/10.1128/AEM.03294-14.
34. Nayar AS, Dougherty TJ, Ferguson KE, Granger BA, McWilliams L, Stacey C, Leach LJ, Narita S, Tokuda H, Miller AA, Brown DG, McLeod SM. 2015. Novel antibacterial targets and compounds revealed by a high-throughput cell wall reporter assay. J Bacteriol 197:1726–1734. https://doi.org/10.1128/JB.02552-14.
35. Wilson MZ, Wang R, Gitai Z, Seyedsayamdost MR. 2016. Mode of action and resistance studies unveil new roles for tropodithietic acid as an anticancer agent and the γ-glutamyl cycle as a proton sink. Proc Natl Acad Sci U S A 113:1630–1635. https://doi.org/10.1073/pnas.1518034113.
36. Hurley KA, Santos TMA, Nepomuceno GM, Huynh V, Shaw JT, Weibel DB. 2016. Targeting the bacterial division protein FtsZ. J Med Chem 59:6975–6998. https://doi.org/10.1021/acs.jmedchem.5b01098.
37. Jayamani E, Rajamuthiah R, Larkins-Ford J, Fuchs BB, Conery AL, Vilcinskas A, Ausubel FM, Mylonakis E. 2015. Insect-derived cecropins display activity against *Acinetobacter baumannii* in a whole-animal high-throughput *Caenorhabditis elegans* model. Antimicrob Agents Chemother 59:1728–1737. https://doi.org/10.1128/AAC.04198-14.
38. Lin L, Nonejuie P, Munguia J, Hollands A, Olson J, Dam Q, Kumaraswamy M, Rivera H, Corriden R, Rohde M, Hensler ME, Burkart MD, Pogliano J, Sakoulas G, Nizet V. 2015. Azithromycin synergizes with cationic antimicrobial peptides to exert bactericidal and therapeutic activity against highly multidrug-resistant gram-negative bacterial pathogens. EBioMedicine 2:690–698. https://doi.org/10.1016/j.ebiom.2015.05.021.
39. Baumann P, Doudoroff M, Stanier RY. 1968. A study of the Moraxella group. II. Oxidative-negative species (genus Acinetobacter). J Bacteriol 95:1520–1541.
40. Wilson DN. 2011. On the specificity of antibiotics targeting the large ribosomal subunit. Ann N Y Acad Sci 1241:1–16. https://doi.org/10.1111/j.1749-6632.2011.06192.x.
41. Parnham MJ, Haber VE, Giamarellos-Bourboulis EJ, Perletti G, Verleden GM, Vos R. 2014. Azithromycin: mechanisms of action and their relevance for clinical applications. Pharmacol Ther 143:225–245. https://doi.org/10.1016/j.pharmthera.2014.03.003.
42. Chopra I, Roberts M. 2001. Tetracycline antibiotics: mode of action, applications, molecular biology, and epidemiology of bacterial resistance. Microbiol Mol Biol Rev 65:232–260. https://doi.org/10.1128/MMBR.65.2.232-260.2001.
43. Mazzei T, Mini E, Novelli A, Periti P. 1993. Chemistry and mode of action of macrolides. J Antimicrob Chemother 31:1–9. https://doi.org/10.1093/jac/31.suppl_C.1.
44. Jana S, Deb JK. 2006. Molecular understanding of aminoglycoside action and resistance. Appl Microbiol Biotechnol 70:140–150. https://doi.org/10.1007/s00253-005-0279-0.
45. Typas A, Banzhaf M, Gross CA, Vollmer W. 2011. From the regulation of peptidoglycan synthesis to bacterial growth and morphology. Nat Rev Microbiol 10:123–136. https://doi.org/10.1038/nrmicro2677.
46. Spratt BG. 1975. Distinct penicillin binding proteins involved in the division, elongation, and shape of *Escherichia coli* K12. Proc Natl Acad Sci U S A 72:2999–3003. https://doi.org/10.1073/pnas.72.8.2999.
47. Davies TA, Shang W, Bush K, Flamm RK. 2008. Affinity of doripenem and comparators to penicillin-binding proteins in *Escherichia coli* and *Pseudomonas aeruginosa*. Antimicrob Agents Chemother 52:1510–1512. https://doi.org/10.1128/AAC.01529-07.
48. Cayô R, Rodríguez M-C, Espinal P, Fernández-Cuenca F, Ocampo-Sosa AA, Pascual Á, Ayala JA, Vila J, Martínez-Martínez L. 2011. Analysis of genes encoding penicillin-binding proteins in clinical isolates of *Acinetobacter baumannii*. Antimicrob Agents Chemother 55:5907–5913. https://doi.org/10.1128/AAC.00459-11.
49. Kocaoglu O, Carlson EE. 2015. Profiling of β-lactam selectivity for penicillin-binding proteins in *Escherichia coli* strain DC2. Antimicrob Agents Chemother 59:2785–2790. https://doi.org/10.1128/AAC.04552-14.
50. Sumita Y, Fukasawa M. 1995. Potent activity of meropenem against *Escherichia coli* arising from its simultaneous binding to penicillin-binding proteins 2 and 3. J Antimicrob Chemother 36:53–64. https://doi.org/10.1093/jac/36.1.53.
51. National Center for Biotechnology Information. 2008. PubChem Compound Database: CID 24192962. National Center for Biotechnology Information, Bethesda, MD. https://pubchem.ncbi.nlm.nih.gov/compound/24192962.
52. Floss HG, Yu T-W. 2005. Rifamycin mode of action, resistance, and biosynthesis. Chem Rev 105:621–632. https://doi.org/10.1021/cr030112j.
53. Goldstein BP. 2014. Resistance to rifampicin: a review. J Antibiot (Tokyo) 67:625–630. https://doi.org/10.1038/ja.2014.107.
54. Jamieson FB, Guthrie JL, Neemuchwala A, Lastovetska O, Melano RG, Mehaffy C. 2014. Profiling of rpoB mutations and MICs for rifampin and rifabutin in *Mycobacterium tuberculosis*. J Clin Microbiol 52:2157–2162. https://doi.org/10.1128/JCM.00691-14.
55. Siu GKH, Zhang Y, Lau TCK, Lau RWT, Ho P-L, Yew W-W, Tsui SKW, Cheng VCC, Yuen K-Y, Yam W-C. 2011. Mutations outside the rifampicin resistance-determining region associated with rifampicin resistance in *Mycobacterium tuberculosis*. J Antimicrob Chemother 66:730–733. https://doi.org/10.1093/jac/dkq519.
56. Giannouli M, Di Popolo A, Durante-Mangoni E, Bernardo M, Cuccurullo S, Amato G, Tripodi M-F, Triassi M, Utili R, Zarrilli R. 2012. Molecular epidemiology and mechanisms of rifampicin resistance in *Acinetobacter baumannii* isolates from Italy. Int J Antimicrob Agents 39:58–63. https://doi.org/10.1016/j.ijantimicag.2011.09.016.
57. Tupin A, Gualtieri M, Roquet-Banères F, Morichaud Z, Brodolin K, Leonetti J-P. 2010. Resistance to rifampicin: at the crossroads between ecological, genomic and medical concerns. Int J Antimicrob Agents 35:519–523. https://doi.org/10.1016/j.ijantimicag.2009.12.017.
58. Perez F, Hujer AM, Hujer KM, Decker BK, Rather PN, Bonomo RA. 2007. Global challenge of multidrug-resistant *Acinetobacter baumannii*. Antimicrob Agents Chemother 51:3471–3484. https://doi.org/10.1128/AAC.01464-06.
59. Maragakis LL, Perl TM. 2008. Antimicrobial resistance: *Acinetobacter baumannii*: epidemiology, antimicrobial resistance, and treatment options. Clin Infect Dis 46:1254–1263. https://doi.org/10.1086/529198.
60. Lin M-F, Lan C-Y. 2014. Antimicrobial resistance in *Acinetobacter baumannii*: from bench to bedside. World J Clin Cases 2:787–814. https://doi.org/10.12998/wjcc.v2.i12.787.
61. Kumaraswamy M, Lin L, Olson J, Sun C-F, Nonejuie P, Corriden R,

การเสนอผลงานในที่ประชุมวิชาการ

24TH BSGC BIOLOGICAL SCIENCES GRADUATE CONGRESS

19th – 21st December 2019, University of Malaya

[D5]

Mechanism of killing of a novel vibriophage toward Acute Hepatopancreatic Necrosis Disease-causing *Vibrio parahaemolyticus* (VP_{AHPND})

Khrongkhwan Thammatinna[a], MacKennon E. Egan[c], Htut Htut Htoo[b] Kanika Khanna[c], Joseph Sugie[c], Jason F. Nideffer[c], Elizabeth Villa[c], Anchalee Tassanakajon[a], Joe Pogliano[c], Poochit Nonejuie[b] and Vorrapon Chaikeeratisak[a]

[a]Center of Excellence for Molecular Biology and Genomics of Shrimp, Department of Biochemistry, Faculty of Science, Chulalongkorn University, Bangkok, 10330, Thailand.
[b] Institute of Molecular Biosciences, Mahidol University, Salaya, Nakhon Pathom, Thailand.
[c] Division of Biological Sciences, University of California, San Diego, La Jolla, California, USA.

Presenter's email: Khrongkhwan.kt@gmail.com

The widespread of *Vibrio parahaemolyticus* (VP_{AHPND}) that causes the acute hepatopancreatic necrosis disease (AHPND) results in a mass mortality of shrimps and aquatic animals. Due to the emergence of multidrug resistance of *V. parahaemolyticus* which makes this harder to handle, alternatives to combat VP_{AHPND} and its resistant strains are urgently needed. Bacteriophage - a virus that replicates and kills bacteria – then becomes a possible tool to use as a biocontrol against the pathogenic bacteria. In this study, we isolated a novel bacteriophage against VP_{AHPND} from sea water and named it "Seahorse" due to its structure under transmission electron microscopy. One-step growth curve revealed that it has short latency time (~20 minutes) and produces offspring at 72 pfu/cell. The genome sequence was 45,171 bp long encoding 48 putative open reading frames and 3 tRNAs. Furthermore, at 10 minute-post infection, blob-shaped nucleoids appeared in the infected cell and the number of cells containing the blobs significantly increased over the time. They turned into toroid-shaped DNA during the late infection. The cellular morphology of phage treated cells was similar to that of tetracycline treated cells suggesting that phage Seahorse exhibits a mechanism of killing that interferes host protein translation during its reproduction.

Keywords: bacteriophages, Vibriophage, *Vibrio parahaemolyticus*, VPAHPND, Mechanism of killing

<u>รายงานสรุปการนำผลงานวิจัยไปใช้ประโยชน์</u>

สัญญาเลขที่ MRG6180027

ชื่อโครงการ การบำบัดรักษาโรคติดเชื้อวิบริโอด้วยเฟจ: การคัดแยกและระบุตัวตนเฟจขนาดใหญ่ชนิดใหม่ที่มีความจำเพาะต่อกลุ่มแบคทีเรียวิบริโอ (Phage therapy for Vibrio infections: Isolation and identification of novel giant bacteriophages with broad host spectrum against vibrios)

หัวหน้าโครงการ วรพนธ์ ชัยกีรติศักดิ์ **หน่วยงาน** ภาควิชาชีวเคมี คณะวิทยาศาสตร์ จุฬาลงกรณ์มหาวิทยาลัย

โทรศัพท์ 02-218-5430 **โทรสาร – อีเมล์** Vorrapon.c@chula.ac.th

สถานะผลงาน □ **ปกปิด** ☑ **ไม่ปกปิด**

ความสำคัญ / ความเป็นมา

แบคทีเรียในสกุล *Vibrio* ซึ่งเป็นแบคทีเรียแกรมลบ (Gram Negative Bacteria) พบมากในน้ำทะเล เป็นสาเหตุหลักที่ก่อให้เกิดโรคในสัตว์น้ำเศรษฐกิจมากมายหลายชนิด โดยส่งผลกระทบต่ออุตสาหกรรมสัตว์น้ำและการส่งออกผลิตภัณฑ์จากสัตว์น้ำในประเทศไทยอย่างมาก โดยการป้องกันการระบาดของแบคทีเรียวิบริโอนั้น สามารถทำได้ทั้งหมด 2 วิธี ได้แก่ การใช้ยาปฏิชีวนะ (Antibiotics) และการบำบัดด้วยแบคเทอริโอเฟจ (Bacteriophage therapy) แต่เนื่องจากการใช้ยาปฏิชีวนะทำให้เกิดการดื้อยาของแบคทีเรีย ดังนั้นการใช้ยาปฏิชีวนะจึงไม่ใช่วิธีที่เหมาะสมสำหรับการการป้องกันการระบาดของเชื้อแบคทีเรีย รวมทั้งยาปฏิชีวนะยังเป็นสารตกค้างได้ จึงอาจถูกส่งผ่านมายังมนุษย์ผ่านการบริโภคสัตว์น้ำ ดังนั้นการบำบัดด้วยแบคเทอริโอเฟจ จึงเป็นทางเลือกใหม่ที่สามารถนำมาใช้ทดแทนการใช้ยาปฏิชีวนะ เพื่อบำบัดรักษาโรคติดเชื้อวิบริโอ รวมทั้งป้องกันการระบาดของโรคจากเชื้อแบคทีเรียวิบริโอได้

วัตถุประสงค์ของโครงการ

1. คัดเลือก และทำบริสุทธิ์เฟจที่มีฤทธิ์ฆ่าเชื้อแบคทีเรียในสกุล *Vibrio* จากแหล่งน้ำทะเลธรรมชาติ
2. ศึกษาความเป็นไปได้ในการนำเฟจมาใช้ในการบำบัดรักษาโรคติดเชื้อวิบริโอ

ผลการวิจัย *(สั้น ๆ ที่บ่งชี้ประเด็นข้อค้นพบ กระบวนการ ผลผลิต และการเรียนรู้)*

จากการคัดแยกเฟจจากธรรมชาติที่มีฤทธิ์ในการฆ่าเชื้อ *Vibrio* จากธรรมชาติ ทีมวิจัยได้ค้นพบเฟจชนิดใหม่ ที่มีฤทธิ์ฆ่าเชื้อ *V. parahemolyticus* ชนิดที่ก่อโรคตับและตับอ่อนวายฉับพลัน (Acute Hepatopancreatic Necrosis Disease, APHND) ซึ่งมีลักษณะคล้ายโรคตายด่วนในสัตว์น้ำเศรษฐกิจ โดยเฟจดังกล่าวมีความจำเพาะสูงและไม่ฆ่าเชื้อแบคทีเรียวิบริโอชนิดอื่นๆ ระหว่างกระบวนการฆ่าเชื้อแบคทีเรีย เฟจดังกล่าวมีกลไกที่คล้ายคลึงกับการฆ่าเชื้อด้วยยาปฏิชีวนะ Tetracycline คือ มีกลไกในการยับยั้งกระบวนการสังเคราะห์โปรตีนภายในเซลล์แบคทีเรีย เมื่อศึกษาจีโนมของเฟจในเชิงลึกและลำดับทางพันธุกรรมด้วยเทคนิค Whole genome sequencing และเทคนิคเทคนิคชีวสารสนเทศ (Bioinformatics) พบว่า เฟจชนิดนี้ มีขนาดของจีโนมประมาณ 45,171 คู่เบส และมีจำนวนของ Open reading frame (ORFs) ทั้งหมด 48 ORFs โดยจีโนมของเฟจนี้ สามารถสร้างโปรตีนได้หลากหลายชนิด ที่มีส่วนเกี่ยวข้องกับเมตาบอลิซึมขั้นพื้นฐานของสิ่งมีชีวิต องค์ประกอบทางโครงสร้างของเฟจ โปรตีนที่เกี่ยวข้องกับการฆ่าเซลล์แบคทีเรียและโปรตีนที่ไม่ทราบหน้าที่อีกจำนวนมาก นอกจากนี้ผลการศึกษาระดับจีโนม ไม่พบยีนที่เกี่ยวข้องกับการดื้อยาปฏิชีวนะ และการสร้างสารพิษในเฟจชนิดนี้ จึงมีความเป็นไปได้สูงในการนำเฟจดังกล่าวมาประยุกต์ใช้ เพื่อบำบัดรักษาโรคติดเชื้อวิบริโอ รวมทั้งป้องกันการระบาดของโรคจากเชื้อแบคทีเรียวิบริโอ *V. parahemolyticus* ชนิดที่ก่อโรคตับและตับอ่อนวายฉับพลันได้

คำสืบค้น (Keywords)

Vibrio, Phage therapy, Phage biocontrol, Mechanism of pre-killing (MOK)

การนำผลงานวิจัยไปใช้ประโยชน์ *(ดูคำจำกัดความ และตัวอย่างด้านหลังแบบฟอร์ม)*

☐ **ด้านนโยบาย** **โดยใคร** *(กรุณาให้ข้อมูลเจาะจง)*.....
มีการนำไปใช้อย่างไร
.....

☐ **ด้านสาธารณะ** **โดยใคร** *(กรุณาให้ข้อมูลเจาะจง)* .....
มีการนำไปใช้อย่างไร
.....

☐ **ด้านชุมชนและพื้นที่** **โดยใคร** *(กรุณาให้ข้อมูลเจาะจง)* .....
มีการนำไปใช้อย่างไร
.....

☐ **ด้านพาณิชย์** **โดยใคร** *(กรุณาให้ข้อมูลเจาะจง)* .....
มีการนำไปใช้อย่างไร
.....

☑ **ด้านวิชาการ**

โดยใคร *(กรุณาให้ข้อมูลเจาะจง)* อาจารย์ นักวิจัย นักศึกษา นวัตกร ที่สนใจนำเฟจไปใช้เพื่อบำบัดรักษาโรคหรือป้องกันการระบาดของโร
จากแบคทีเรียก่อโรค

มีการนำไปใช้อย่างไร *(กรุณาให้ข้อมูลเจาะจง)*

ตีพิมพ์เผยแพร่ผลงานวิจัยระดับนานาชาติจำนวน 3 เรื่อง

1. (งานวิจัยหลัก) ในวารสาร Scientific Reports ซึ่งเป็นวารสารที่อยู่ใน Quartile in Category Q1 และมี Impact Factor 4.122
Thammatinna, K., Egan, M.K.E., Htoo, H.H., Khanna, K., Sugie, J., Nideffer, J.F., Villa, E., Tassanakajon, A., Pogliano, J., Nonejuie
P., Chaikeeratisak, V. (2020) A novel vibriophage exhibits inhibitory activity against host protein synthesis machinery. Scientifi
Reports 10 (1), 2347.

2. (งานวิจัยเสริม) ในวารสาร Cell ซึ่งเป็นวารสารที่อยู่ใน Quartile in Category Q1 และมี Impact Factor 36.216
Chaikeeratisak, V., Khanna, K., Nguyen, K.T., Sugie, J., Egan, M.E., Erb, M.L., Vavilina, A., Nonejuie, P., Nieweglowska, E
Pogliano, K., et al. (2019). Viral Capsid Trafficking along Treadmilling Tubulin Filaments in Bacteria. Cell 177, 1771-1780.e12.

3. (งานวิจัยเสริม) ในวารสาร Antimicrobial Agents and Chemotherapy (AAC) ซึ่งเป็นวารสารที่อยู่ใน Quartile in Category Q1 และ
มี Impact Factor 4.256
Htoo, H.H., Brumage, L., Chaikeeratisak, V., Tsunemoto, H., Sugie, J., Tribuddharat, C., Pogliano, J., and Nonejuie, P. (2019)
Bacterial Cytological Profiling as a Tool To Study Mechanisms of Action of Antibiotics That Are Active against Acinetobacte
baumannii. Antimicrobial agents and chemotherapy 63 (4), e02310-18

☐ **ยังไม่มีการนำไปใช้** (โปรดกรอกในกรอบถัดไป)

(กรณีที่ยังไม่มีการใช้ประโยชน์) **ผลงานวิจัยมีศักยภาพในการนำไปใช้ประโยชน์**

☐ **ด้านนโยบาย** ☐ **ด้านสาธารณะ** ☐ **ด้านชุมชนและพื้นที่** ☐ **ด้านพาณิชย์** ☐ **ด้านวิชาการ**

ข้อเสนอแนะเพื่อให้ผลงานถูกนำไปใช้ประโยชน์

.....
.....

การเผยแพร่/ประชาสัมพันธ์ *(กรุณาให้รายละเอียด พร้อมแนบหลักฐาน)*

1. สิ่งพิมพ์ หรือสื่อทั่วไป

   ☐ หนังสือพิมพ์ ☐ วารสาร ☐ โทรทัศน์ ☑ วิทยุ ☐ เว็บไซต์ ☐ คู่มือ/แผ่นพับ ☐ จัดประชุม/อบรม ☑ อื่น ๆ

   - รายการวิทยุ "ทันโลกวิทยาศาสตร์" ถ่ายทอดผ่านวิทยุ FM 101.5 MHz วันที่ 9 กุมภาพันธ์ พ.ศ. 2562 เวลา 10.00 น. - 10.30 น.
   - นางสาวครองขวัญ ธรรมทินนะ ได้เสนอผลงานในรูปแบบ Oral presentation ในงานประชุมวิชาการนานาชาติ The 24th Biological Science Graduate Congress 2019 (BSGC2019) ที่จัดขึ้นระหว่างวันที่ 19 – 21 ธันวาคม พ.ศ. 2562

2. สิ่งพิมพ์ทางวิชาการ *(วารสาร, การประชุม ให้ระบุรายละเอียดแบบการเขียนเอกสารอ้างอิง เพื่อการค้นหาซึ่งควรประกอบด้วย ชื่อผู้แต่ง ชื่อเรื่อง แหล่งพิมพ์ ปี พ.ศ. (ค.ศ.) ฉบับที่ หน้า)*

ตีพิมพ์เผยแพร่ผลงานวิจัยระดับนานาชาติจำนวน 3 เรื่อง

1. (งานวิจัยหลัก) ในวารสาร Scientific Reports ซึ่งเป็นวารสารที่อยู่ใน Quartile in Category Q1 และมี Impact Factor 4.122

Thammatinna, K., Egan, M.K.E., Htoo, H.H., Khanna, K., Sugie, J., Nideffer, J.F., Villa, E., Tassanakajon, A., Pogliano, J., Nonejuie P., Chaikeeratisak, V. (2020) A novel vibriophage exhibits inhibitory activity against host protein synthesis machinery. Scientifi Reports 10 (1), 2347.

2. (งานวิจัยเสริม) ในวารสาร Cell ซึ่งเป็นวารสารที่อยู่ใน Quartile in Category Q1 และมี Impact Factor 36.216

Chaikeeratisak, V., Khanna, K., Nguyen, K.T., Sugie, J., Egan, M.E., Erb, M.L., Vavilina, A., Nonejuie, P., Nieweglowska, E Pogliano, K., et al. (2019). Viral Capsid Trafficking along Treadmilling Tubulin Filaments in Bacteria. Cell 177, 1771-1780.e12.

3. (งานวิจัยเสริม) ในวารสาร Antimicrobial Agents and Chemotherapy (AAC) ซึ่งเป็นวารสารที่อยู่ใน Quartile in Category Q1 และ Impact Factor 4.256

Htoo, H.H., Brumage, L., Chaikeeratisak, V., Tsunemoto, H., Sugie, J., Tribuddharat, C., Pogliano, J., and Nonejuie, P. (2019) Bacterial Cytological Profiling as a Tool To Study Mechanisms of Action of Antibiotics That Are Active against Acinetobacte baumannii. Antimicrobial agents and chemotherapy 63 (4), e02310-18

<u>คำอธิบายและตัวอย่างการนำไปใช้ประโยชน์ในแต่ละด้าน</u>

1. การใช้ประโยชน์ด้านนโยบาย

คำจำกัดความ : การนำความรู้จากงานวิจัยไปใช้ในกระบวนการกำหนดนโยบาย ซึ่งนโยบายหมายถึง หลักการ แนวทาง กลยุทธ์ ในการดำเนินงานเพื่อให้บรรลุวัตถุประสงค์ อาจเป็นนโยบายระดับประเทศ ระดับภูมิภาค ระดับจังหวัด ระดับท้องถิ่น หรือระดับหน่วยงาน นโยบายที่ดีจะต้องประกอบด้วยวัตถุประสงค์ แนวทาง และกลไกในการดำเนินงานที่ชัดเจน สอดคล้องกับปัญหาและความต้องการการใช้ประโยชน์ด้านนโยบายจะรวมทั้งการนำองค์ความรู้ไปสังเคราะห์เป็นนโยบายหรือทางเลือกเชิงนโยบาย (policy options) แล้วนำนโยบายนั้นไปสู่ผู้ใช้ประโยชน์

2. การใช้ประโยชน์ด้านสาธารณะ

คำจำกัดความ : การดำเนินงานเพื่อนำผลงานวิจัยและนวัตกรรม ไปใช้ในวงกว้างเพื่อประโยชน์ของสังคม และประชาชนทั่วไป ให้มีความรู้ความเข้าใจ เกิดความตระหนัก รู้เท่าทันการเปลี่ยนแปลง ซึ่งนำไปสู่การเปลี่ยนวิธีคิด พฤติกรรม เพื่อเพิ่มคุณภาพชีวิตของประชาชน สร้างสังคมคุณภาพ และส่งเสริมคุณภาพสิ่งแวดล้อม

3. การใช้ประโยชน์ด้านพาณิชย์

คำจำกัดความ : การนำนวัตกรรม เทคโนโลยี ผลิตภัณฑ์ใหม่ พันธุ์พืช พันธุ์สัตว์ ไปสู่การผลิตในเชิงพาณิชย์ การสร้างมูลค่าเพิ่มของผลิตภัณฑ์ การแปรรูป การสร้างตราสินค้า การเพิ่มประสิทธิภาพในกระบวนการผลิต และการลดต้นทุนการผลิต การสร้างอาชีพ และทางเลือกให้กับผู้ประกอบการ เกษตรกรหรือผู้ประกอบอาชีพอื่น ๆ

4. การใช้ประโยชน์ด้านชุมชนและพื้นที่

คำจำกัดความ : การนำกระบวนการ วิธีการ องค์ความรู้ การเปลี่ยนแปลง การเสริมพลัง อันเป็นผลกระทบที่เกิดจากการวิจัยและพัฒนาชุมชน ท้องถิ่น พื้นที่ ไปใช้ให้เกิดประโยชน์การขยายผลต่อชุมชน ท้องถิ่นและสังคมอื่น

5. การใช้ประโยชน์ด้านวิชาการ

คำจำกัดความ : การนำองค์ความรู้จากผลงานวิจัยที่ตีพิมพ์ในรูปแบบต่าง ๆ เช่น ผลงานตีพิมพ์ในวารสารระดับนานาชาติ ระดับชาติ หนังสือ ตำรา บทเรียน ไปเป็นประโยชน์ด้านวิชาการ การเรียนรู้ การเรียนการสอน ในวงนักวิชาการและผู้สนใจด้านวิชาการ รวมถึงการนำผลงานวิจัยไปวิจัยต่อยอด หรือการนำไปสู่ product และ process ไปใช้ในการเสริมสร้างนวัตกรรม และเทคโนโลยี